M.Sc. Víctor Hugo Mosquera Leyton

Universidad
del Cauca

Medical applications of low speed and resolution electrical impedance tomography

Director:

Ph.D. Carlos Felipe Rengifo Rodas

Co-Director:

Ph.D. Ramon Bragós Bardia

University of Cauca
Faculty of Engineering in Electronic and Telecomunications

PhD in Electronics sciences

February, 2021

II

Contents

List of Figures

List of Tables

Table of Abbreviations

- ADC: Analog-to-Digital Converter.
- AE: Absolute Error.
- BEM: Border Element Method.
- BMD: Bone Mineral Density.
- CC: Pearson's Correlation Coefficient.
- CEM: Complete Electrode Model.
- CG: Conjugate Gradient Algorithm.
- CN: Coronet arrangement.
- CWMF: Combined Wavelet Based Mesh Free.
- DAC: Digital-to-Analog Converter.
- DC: Direct Current.
- DDS: Direct Digital Synthesizer.
- DEM: Domain Embedding Method.
- DSP: Digital Signal Processor.
- EIDORS: Electrical Impedance Tomography and Diffuse Optical Tomography Reconstruction Software.
- EIT: Electrical Impedance Tomography.
- FEM: Finite Elements Method.

- FIM: Focused Impedance Method.
- FIM-4: Focused Impedance Measurement Tetra-polar.
- FIM-I: Focused Impedance Measurement Internal electrodes.
- FIM-IE: Focused Impedance Measurement Internal and External electrodes.
- FPGA: Field-Programmable Gate Array.
- fps: Frames per second.
- FWR: Full-Wave Rectifier mode.
- GFEM: Generalized FEM.
- GI: Global Impedance.
- GN−OS: Gauss−Newton One Step algorithm.
- GN: Gauss−Newton Algorithm.
- GUI: Graphical User Interface.
- H2L: Two Horizontal Lines arrangement.
- HNN: Hopfield Neural Networks.
- IRM: Impedance Ratio Method.
- MUX: Multiplexed.
- MVCR: Modified VCR.
- NCD: Non-communicable Diseases.
- NR: Newton−Raphson Algorithm.
- PDIPM: Primal and Dual Interior Point Method.
- PE: Percentage of Error.
- RBNN: Radial Basis Neural Networks.
- RE: Relative Error.
- RG: Ring arrangement.
- SC: semicircular arrangement.
- SNR: Signal to Noise Ratio.
- UI: Urinary incontinence.

- V2L: Two Vertical Lines arrangement.
- VCCS: Voltage Controlled Current Source.
- VCR: Voltage Change Ratios.
- WHO: World Health Organization.

Abstract

Urinary incontinence (UI), detrusor overactivity and prostatic hyperplasia are pathologies that cause urinary tract infections due to loss of sphincter control. UI is a common condition in elderly people, and between 15% to 35% of all adults suffer from severe UI. Additionally, people suffering from spinal cord injuries are highly prone to urinary tract infection due to the loss of micturition sensation. According to the World Health Organization, the prevalence of urinary tract diseases ranges from 40 to 80 people per million. Hence, UI is a public health problem. UI affects self-esteem and quality of life, and it is associated with higher rates of depression. UI also affects daily activities such as work, travel, social interaction, physical activity, sexual function, and sleep. Currently, catheterization is the most commonly used method for evacuating the bladder for people with UI, but the periodicity of the associated emptying procedures depends on an empirical estimate of the time it takes to fill the patient's bladder. Underestimating this period unnecessarily increases the number of catheterization procedures, thus increasing the risk of infections, cancers, and kidney stones. Conversely, overestimation of the catheterization period increases the risk of complications such as over-distension of the bladder wall, hydronephrosis, and autonomic dysreflexia. Ultrasound-based estimates are the gold standard to estimate bladder volume, with advantages of high portability and accuracy. However, ultrasound measurements must be performed by professionals, precluding continuous monitoring and limiting application to bladder volume monitoring.

Due to the electrical conductivity of the urine, several bioimpedance techniques have been considered for bladder volume monitoring. Among these, Global Impedance (GI), which presents a high accuracy in volume estimation for the following configurations: (1) simple ring electrode arrangement with adjacent patterns for injection and measurement, (2) two vertical lines V2L electrodes arrangement with opposite patterns for injection and measurement. Other proposed approaches for bladder monitoring are: Voltage Change Ratios (VCR), Impedance Ratio Method (IRM) and Focused Impedance Method (FIM). Which present high sensitive to changes in the conductivity, just like GI. Therefore, these approaches are not suitable for long-term monitoring of the bladder, because the conductivity of urine varies with health status and diet.

The robustness of a new proposal based on FIM was evaluated in a bladder phantom, presenting a low sensibility to the conductivity uncertainty of the phantom; being a promising technique for long-term monitoring of the bladder and would support the assisted bladder emptying process.

Acknowledgment

To my beloved wife and our children, who in the difficult moments of this process, their love was the incentive to continue. To my parents, from whom I have always received their support. To family and friends, whose encouraging messages always accompanied me.

To Carlos Felipe Rengifo and Ramon Bragós Bardía, who generously shared their knowledge and made it possible to finish this project. To the University of Cauca and DEIC, which supported each step in this process. To the Technical University of Catalonia and Carlos, Marta, Alfonso, Adrian, Nohemi, who made my internships in Barcelona a space of knowledge and personal growth. To Martha, Eliana, Karin, Pablo and Hermes, for their unparalleled companionship.

1 Introduction

Electrical impedance tomography (EIT) is a non-invasive technique to obtain images of the internal conductivity of an object. The EIT systems are based on the injection of current signals and the measurement of the generated potentials at the boundary of the object under study. In EIT applications on biological tissues, the currents are usually sinusoidal, with amplitudes below 1 mA and frequencies ranging from 1 kHz and 100 kHz. Once the potentials and currents are known, an image reconstruction method is used to estimate the spatial distribution of the internal electrical conductivity of the analyzed object [2].

The EIT has numerous applications in the medical field, successfully venturing into the monitoring of intracranial bruising [3], cancer detection [4], study of pelvic fluid accumulation [5], analysis of pulmonary ventilation [6], estimation of blood pressure [7], among others. The non-invasive and radiation-free nature of EIT make this technique a good alternative to support the diagnosis and follow-up of pathologies [2,8].

In recent decades, prototype systems for EIT have been proposed using Field Programmable Gate Arrays (FPGAs) and Digital Signal Processors (DSP). These devices generate up to 50 frames per second (fps), which has spread the application of EIT to problems with a high temporal variation in conductivity, such as blood pressure monitoring [6,7,9–11]. For EIT systems oriented to medical applications with a low temporal variability in their conductivity, the use of microcontrollers presents good results as evidenced in [12–14], with a lower cost than systems developed with FPGAs and DSPs. Process such as bladder emptying [5,15–17], stomach emptying [18,19], and studies of the cranial cavity [3,20–23] and the bone system [24–27] are fields in which EIT systems with a low number of images per second can be applied to pathology monitoring.

The current work proposes an EIT prototype for medical applications that require a low frames frequency, for which it is essential to analyze the effect of: i) the arrangement of surface electrodes, ii) the variation in the patterns of injection and measurement of signals and iii) the image reconstruction algorithms, in the performance of the EIT.

1.1 Problem

The World Health Organization (WHO) reveals that until 2018 mortality due to non-communicable diseases (NCDs) was approximately 85% in countries with medium and low income and worldwide 71% of deaths were due to the non-communicable diseases (NCD)[1]. On other hand, WHO, in its report entitled "Formulation of Policies on Medical Devices" [28] indicates that the population with the lowest resources, are 10 times more likely to die before of 14 years old. These mortality rates are due to the growing inequality gap related to technology access to support diagnostic processes. For this reason, an objective of WHO is to boost the development of biomedical technology to improve efficiency and quality in the provision of health services [29].

The techniques based on medical images are widely used in diagnostic processes, treatment evaluation and patient monitoring. Despite its limitations, technologies such as 2D ultrasound, computed tomography and magnetic resonance tomography have dabbled in medical environments, becoming an important tool in hospital care. For example, 2D ultrasound has a high interoperating variability, because it requires support methods for diagnostic [30]. On the other hand, computed tomography requires radiation and ionizing contrast, which leads to limited use on people [31]. Finally, the magnetic resonance tomography has the disadvantage of the time involved in obtaining the images, between 15 minutes and 1 hour, in addition to the high cost and low availability of this technology in developing countries [32].

EIT is a medical imaging alternative that is in increasing development in the field of biomedical applications [2, 33–36], as: evaluation of lung function [37–40], diagnosis of cystic fibrosis [41], monitoring of brain activity [42], detection of heart failure [43, 44], density analysis bone mineral [27], and detection of intracranial bruises [3], among others. Research in this topic focuses on the design of electronic systems, the development of image reconstruction algorithms, and the evaluation of their effectiveness in the diagnosis and monitoring of various pathologies. These points must be addressed to develop EIT applications in the medical field. This project seeks to contribute to the solution of the following question:

What is the effect of the number of electrodes, their geometrical disposition, the injection and measurement patterns and the images reconstruction algorithms in the behavior of the EIT when it is used in medical applications where the system to study presents a low temporal variability of its electrical conductivity?.

1.2 Hypothesis

Considering the problem of the low availability of technology for medical diagnostic processes, treatments evaluation, and patients monitoring, and the high mortality due to NCD, this project raises the following hypothesis:

[1] https://www.who.int/news-room/fact-sheets/detail/noncommunicable-diseases

- A low-cost electrical impedance tomography system can be devised to monitor human physiological processes with low temporal variability, such as bladder filling.
- The performance of EIT systems can be greatly improved by the proper selection of both the spatial distribution of the electrodes and the measurement and injection current patterns.

1.3 Objectives

1.3.1 General objective

To propose a low cost and low resolution EIT prototype for a medical application in which the object to be studied has a low temporal variability of electrical conductivity.

1.3.2 Specific objectives

- To define the requirements of an EIT system to study a biological process of low temporal variability of electrical conductivity.
- To develop a prototype of the EIT system according to the temporal variability requirements of the conductivity of the system to be studied.
- To study the effect of the number of electrodes, their geometrical disposition, the patterns of current injection and potentials measurement, and the image reconstruction algorithms in the behavior of the proposed EIT system.
- To perform an experimental evaluation of the EIT prototype developed on the system under study.

1.4 Contributions

The contributions of this work are listed below.

- *EIT system*: A minimal implementation of EIT system of 8 ports was develop as part of this project. It is based on the front-end for body composition measurement, AFE4300 from Texas Instruments. This EIT system injects the current signal, measures the voltages on the electrodes, and stores a frame every 16 seconds with a maximum SNR of 71.81 dB. The amplitude of the current generated by the AFE4300 is 294.5 μArms, which is below the maximum for a human [45], also it has an electrical safety stage for in-vivo test.

- *Effect of injection and measurement patterns*: During the last decades, numerous studies have reported the effect of the number of electrodes and their spatial arrangement on the quality of EIT images. However, studies in bladder monitoring applications are scarce, and the few existing present results only for ring arrangement, but not for other configurations. An exception to this trend is [46], that uses 16 electrodes to compare different arrangements. Although, this study considers only the adjacent pattern for injection and measurement. In this thesis, GI index was employed to volume estimation considering 5 different arrangements of 8 electrodes (simple ring, semicircular, coronet, horizontal lines and vertical lines) and combinations of adjacent and measurement patterns. Our simulation and experimental results indicate that the coronet and ring arrangements present the best performance, when the adjacent pattern is used for injection and measurement.

- *Volume estimation*: A new approach for volume estimation based on FIM was proposed. This approach was tested on a bladder phantom, which emulates the electrical properties of the lower human pelvis. The new approach identifies volume changes, in addition to be robust against the uncertainty of the internal conductivity of the bladder phantom.

1.5 Publications

The results of the project were presented in the following publications:

- **Implementation of a low cost prototype for electrical impedance tomography based on the integrated circuit for body composition measurement AFE4300**. Mosquera Víctor Hugo, Arregui Adrian Ramon Bragós Bardia, and Rengifo Carlos Felipe. Proceedings of the 11th International Joint Conference on Biomedical Engineering Systems and Technologies (BIOSTEC 2018): January 19-21, 2018: Funchal, Madeira, Portugal. Scitepress. DOI:10.5220/0006554901210127.

- **EIDORS-Matlab interface for forward problem solving of electrical impedance tomography**. Mosquera Víctor Hugo, Gonzalez Carlos Manuel and Ortega Edison. III Latin-American Conference on Bioimpedance (CLABIO 2018): October 3-5, 2018: Manizalez, Caldas, Colombia. https://www.researchgate.net/publication/336725029_EIDORS-Matlab_interface_for_forward_problem_solving_of_electrical_impedance_tomography.

- **GUI for performance analysis of EIT image reconstruction algorithms**. Mosquera Víctor Hugo, Rengifo Carlos Felipe, Melenge Alejandro and Fernandez Nelson Fernando. V International Congress on Engineering, Technology and Automation (CIITA2019): December 2-4, 2019: Medellín, Antioquia, Colombia. ISSN 2500-5987. http://memoriascimted.com/wp-content/uploads/2019/01/memorias-ciita-2018.pdf.

- **Robustness of Focused and Global Impedance Estimates of Bladder Volumes against Uncertainty of Urine Conductivity**. MOsquera Víctor Hugo, Bragos Ramon, Rengifo Carlos Felipe. Biomedical Physics & Engineering Express, vol 6. no. 5. 2020. https://doi.org/10.1088/2057-1976/ab8fc7

Other publications derived from the project in:

- **Tomography for electrical impedance an alternative method for monitoring joint injuries**. Muñoz Juan David and Mosquera Víctor Hugo. Ingeniería Solidaria (ISSN on line 2357-6014), vol. 16, no. 1, Jan. 2020. https://doi.org/10.16925/2357-6014.2020.01.05.
- **Electrical Impedance Tomography: Hardware Fundamentals and Medical Applications**. Escobar Fausto Andrés, Mosquera Vítor Hugo and Rengifo Carlos Felipe. Ingeniería Solidaria (ISSN on line 2357-6014), vol. 16, no. 3, Sep. 2020. https://doi.org/10.16925/2357-6014.2020.03.02.

Undergraduate and master's works directed by the author, during the development of the thesis:

- *Electrical impedance tomography for diagnosis of knee osteoarthritis*, master's work in development.
- *Electrical impedance tomography based on mixed signal device*, master's work in development.
- *GUI to support the diagnosis of COPD using electrical impedance tomography*, undergraduate's work finished.
- *Analysis of algorithms to solve the forward problem in the reconstruction of EIT images*, undergraduate's work finished.

2 Literature review

Our literature review followed the guidelines proposed in [47]. This defines a structured procedure for the classification of scientific publications in a given subject. Its application generates information such as: research topics, study populations, particular characteristics of the study, methodology and procedures. The steps defined in this technique are: i) inquiry questions, ii) search for related literature, iii) selection and evaluation, iv) classification scheme and v) data extraction.

The first stage of the methodology answers the following questions:

- What are the applications of EIT in medical environments?
- What are the most analyzed human organs using EIT?
- What are the basic characteristics of an EIT system for medical applications?

The previous questions generated the search strings that will be used for the search in databases. The questions and the search strings are shown in Table 2.1.

Table 2.1: Search results.

Search strings	**IEEE**	**ScienceDirec**	**Scopus**	**Pubmed**
Electrical Impedance Tomography AND Lung	22	21	256	157
Electrical Impedance Tomography AND Brain	16	5	59	69
Urinary Bladder AND Electrical Impedance Tomography	0	0	9	6
Urinary tract AND Electrical Impedance Tomography	0	0	2	11
Electrical Impedance Tomography AND Bladder	1	0	15	2
Electrical Impedance Tomography AND Bone	2	4	7	0
Electrical Impedance Tomography AND Breath	1	2	15	0
Electrical Impedance Tomography AND Blood pressure	0	1	54	5
Total	42	33	417	250

In the second stage of this methodology, a search is carried out in the IEEEXplore, ScienceDirect, Scopus and PubMed databases, and as a results 742 papers were found

(Table 2.1). The third stage consisted in the application of three exclusion criteria: i) works published before 2011, ii) technical reports nor thesis and iii) statistical data on medicals pathologies using standard systems. As a result of this process, a total of 219 relevant references were obtained, which were classified according to the taxonomy shown in Figure 2.1.

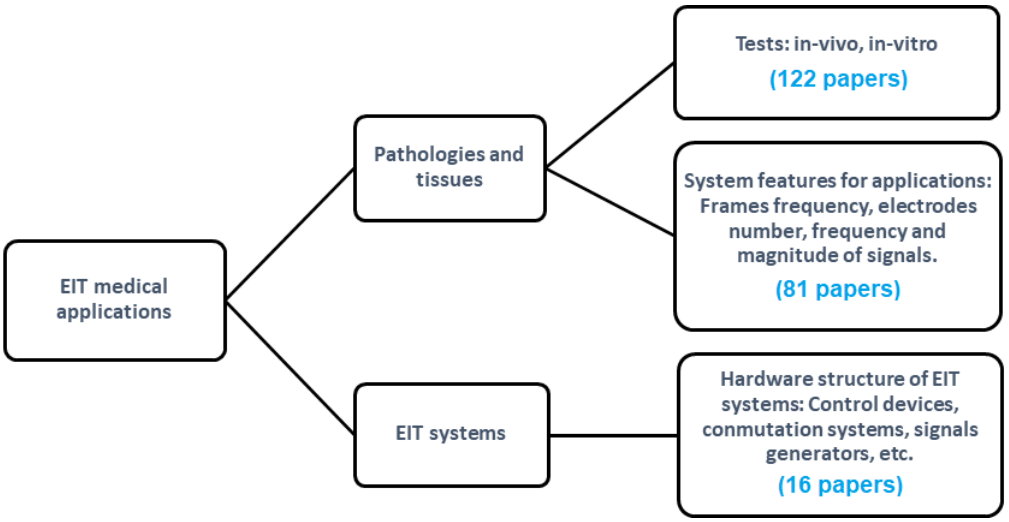

Figure 2.1: Taxonomy used to classify the publications resulting from the literature review process.

Finally, from the extraction and analysis of the data, the characteristics of the EIT systems for medical applications were obtained. These results are presented below:

2.1 EIT systems

The EIT systems Pulmo Vista® 500 of Dräger Global consists of 16 electrodes for injection and measurement of signals using the adjacent method and is able to generate up to 50 frames per second (fps). It is used to monitor the complete ventilation cycle in real time [48, 49]. The Maltron Sheffield Mark EIT system (Brown and Seagar) has been in development for 20 years and like Pulmo Vista® 500, uses 16 electrodes and adjacent pattern for injection and measurement [50]. Its later versions, the Mark I and Mark 2.5 system include a self-calibration system of the voltage injection source, and other modules that improve the performance but that make this a system complex [51, 52]. Other systems such as OXBACT-5 [53] and Darmouth [54] consist of 64 electrodes and use the adjacent method for injection and measurement. These systems, are restricted to a single method of current injection and measurement of potentials, limiting the image reconstruction process [27]. The mentioned EIT devices use a FPGA-based architecture, because FPGAs provide a high sampling rate and integration of several EIT modules, such as the direct digital synthesizer. This aspect reduces hardware and interfaces between the

modules, facilitating their implementation. On the other hand FPGAs require external A/D and D/A converters.

The systems discriminated in Table 2.2 have been evaluated considering the characteristics of the biological process to be monitored, although few of them present in-vivo tests. For example, the system proposed in [55] monitors heart rate at 131 fps and using 16 electrodes. In addition, it reconstructs the images of conductivity distribution of the thoracic cage, clearly differentiating the cross section of the lungs and heart. The injection and measurement method used in the tests is the adjacent. Shi and colleagues [56] who designed an EIT system with 16 electrodes that generates 1 fps and determines the alterations in the brain caused by temporary occlusion in the unilateral carotid artery.

Other prototypes based on FPGA are in the stage of development and are being tested on phantoms to characterize them and to evaluate their potential in medical applications. An example is presented in [57]. This system generates 100 fps with 32 electrodes and uses an adjacent method for injection and measurement. The main limitation of this system is the need of a National Instruments data acquisition board for its implementation, which impacts on costs. Another system tested on phantom is presented by Artem and colleagues [58] which does not depend on proprietary data acquisition system and consists of 16 electrodes for signal injection and measurement. Both works, [57] and [58], present results using only the adjacent injection and measurement method.

The DSPs (Digital Signal Processor) are another alternative for the development of EIT systems, such as in [59, 60]. The system presented in [59] manages 128 electrodes. The prototype described in [60] acquires 100 fps using 8 surface electrodes. Both systems were evaluated on phantoms and employ adjacent patterns for injection and measurement. A differentiating element in the system developed by Wi and his colleagues [60] is the ability to reconfigure the injection and measurement pattern, between the methods adjacent and polar, giving more versatility to the system. The implementation of EIT systems with DSP implies the use of a greater number of electronic components, compared to those implemented with FPGA's, which makes it difficult to implement.

Table 2.2: Hardware charateristics of EIT systems.

Reference	Main module	Signal generator method	Signal Reading card	Discrete components	Frequency range
Santos S [55].	Virtex-6 FPGA	Direct Digital Synthetizer (DDS), compiles v5,0	Virtex-6 FPGA DSP, Kit AD/DA	–	60-960 kHz
Shi X [56].	FPGA	–	ADC Module (NI 5751), (AD9252), signal conditioner(THS 7002TI)	VCCS(AD844)	1-190 kHz
Khan S [57].	FPGA NI Rio 7952R, Vitex 5LX50	(NI 5406), synchronizer NI 6674t	DAC DRIVER/ADC DRIVER	Relay Control NI XSeries 6341, ADC732 (multiplexer)	–
Artem [58].	FPGA Cyclone II Family	NCO (numerically controlled oscillator) M4K block SIN/COS	ADC modules (NI5751)	–	10 - 100kHz
Khan S [61].	FPGA (NI Flex Rio 7952R)	NI 5406 14 bits, synchronizer (NI6674t)	AMP(AD8250), ADC (AD7367)	(NI X-Series Card 6341)	–
Zhang Z [62].	FPGA Cyclone II Family	AD 9852	EP3C10F256C8N FPGA	PCI 9054, PCI9052	–
Zeng Y [63].	FPGA Cyclone II Family	DDS (TMS320F2812)	ADC(AD9235), ROM(EPCS4), DAC(AD9783)	ADC 12 bits, DAC 14 bits	10 Hz-250 kHz
Wi H [60].	DSP(TMS320F2812)	EP3C10F256C8N FPGA	AD624(Pre-amplifier) MAX 275 (Butterworth)	Port(DS1267E-010), switches(MAX4545CAP1009), source(ECM100US07ECM 100US09)	1 Hz - 50 kHz
Xu G [59].	DSP(TMS320F2812 TI)	AD852	AD624(Pre-amplifier) MAX 275 (Butterworth)	MAX306 CPLD(EPM1270)	0.1 Hz - 1MHz
Kukharenko [64].	PSoC (CY8C58LP)	Comparison and amplification modules integrated in PSoC.	ADC 12 bits PSoC	–	800 Hz - 32 MHz
Fouchard A [13].	Raspberry Pi	DDS(AD9837)	ADC(ADS7947), buffer(LMV651, to output DDS), Current sensor (OPA380), measure voltage (SR560)	Redd Relays	0.1 Hz - 1MHz
Chitturi V. [12].	Arduino Mega	Generator IC ICL8038	Amp(TL071 OPA)	Mux (CD4067B)	1 - 60 kHz
Huang J [14].	Microprocessor (MSP 430)	Microprocessor	–	Demodulator AD630	10 Hz - 200 kHz
Khalighi M [65].	Microprocessor Atmega 128	XR-2206 (EXAR Inc)	LF412 IC, AD844, LM393, AD844, ADC (AD1674), AD625.	LF412, 74HC4053, AD625JNZ, TC408tBP, ADG506AKN.	10 Hz - 1 MHz
Oh T [66].	FPGA EP1K50	FPGA EP1K50	NI USB 6259,National Instruments	–	125 Hz - 825 Hz
Dowrick T [67].	EEG amplifier	Arduino Nano	EEG amplifier	AD8039	2.4 kHz - 2.6 kHz

Most of the systems presented in Table 2.2 use adjacent patterns for injection and measurement, without the option to explore other configurations. This is the case of [14], which proposed a microprocessor-based EIT system composed of 16 electrodes that is applied to lung monitoring. Another example is [65], which describes an Arduino-based system of 16 electrodes intended for cancer detection. The experimental results presented in [65] were obtained using a phantom. An exception to the usage of adjacent patterns for injection and measurement is present by Fouchard and collaborators [13]. They designed a system of 8 electrodes with reconfigurable injection and measurement patterns through electronics relays controlled by a Raspberry PI board. This proposal has the disadvantage of being too slow (1 frame every 45 seconds) and working off-line.

The EIT systems based either on microcontrollers or microprocessors require external devices such as the sinusoidal signal generator, a voltage-controlled current source, a switching system to select the electrodes, and a demodulator to obtain the amplitude and phase of the voltage on the electrodes. The time delays introduced by the communication interfaces between these additional components limit the frame rate to a few frames per second.

The performance of EIT systems is verified in saline tanks with electrical conductivity similar to that of the tissue surrounding the organ to study. The latter is emulated by a small plastic cylinder of low conductivity (0.103 S/m for lungs, 0.072 S/m for liver, and 0.0834 S/m for Cortical bones). The number of electrodes used for injection and measurements influence the spatial and temporal resolution, as well as the number of frames and SNR of the reconstructed image [68, 69]. Generally, the EIT systems use 16 electrodes, with an injection current between 50 μA and 9 mA and frequencies ranging from 10 Hz to 1 MHz, depending on the region of the human body.

2.2 Medical applications of EIT

Currently, EIT images are used in medical application, such as the ventilation monitoring [70–72], monitoring blood pressure [7], detection of intracranial hemorrhages [23, 73], estimation of volume of bladder urine [16, 74], establish bone density [27], cardiac minimization after cardiac arrest [75]. The most relevant medical applications in which the EIT presents promising results are detailed below.

2.2.1 Respiratory system

One of the most studied organs using EIT are the lungs. The Table 2.3 presents works related to this organ and the characteristics used by the EIT system. It is evident that many of these works do not present precise information on the characteristics used for the study, especially those that perform tests on humans. The reason is due to the use of a commercial system called PulmoVista® 500, or its predecessors Sheffield Mark I or GOE MF II developed in 1980 and 1990 respectively and it is inferred that they used the

maximum benefits offered by this equipment. For example, the PulmoVista® system has the capacity to generate up to 50 frames per second, using a ring of 16 electrodes, with a current injection of 1 mA. The investigations of the EIT in the field of the respiratory system can be divided in pathology oriented and hardware oriented.

There are works that employ EIT systems previously developed by other researchers or commercial systems, and focus on in-vivo applications. In [76–85], for example, pulmonary ventilation under anesthesia, mechanical ventilation, embolism detection and pulmonary edema are analyzed and monitored in animals. The results obtained in these works presents a high accuracy in the reconstruction of the images that support the medical diagnosis, On the other hand, there are works such as [6, 11, 55, 86–106], in which this technology is applied to a population with the pathologies listed above, confirming the feasibility of using EIT in the detection and monitoring of pulmonary diseases. In [14,91,108–110] systems oriented to pulmonary applications are evaluated. These works detail the development and hardware characteristics; their results are based on test using phantoms, and sometimes on healthy volunteers. This strategy seeks to validate that the developed system complies with the requirements for the diagnosis and monitoring of pathologies, to project it as a future commercial alternative for medical applications.

Tumors and cancer lung have also been studied using EIT. Yang and colleagues [111], monitor tumors in lungs, and in [4], a study of healthy and cancer lung tissue is presented. It is concluded that it is possible to detect and differentiate the two types of tissues, using EIT. This results extends the field of EIT systems to the diagnosis of cancer.

According to the literature, the study of the pulmonary system requires a high performance EIT system, due to the high frequency of frames necessary to analyze lung pathologies, which leads to high hardware characteristics, necessary for the processing of the collected signals, increasing the cost of system.

2.2.2 Hemodynamic system monitoring

Hemodynamic system monitoring is required to follow the evolution of a patient. The EIT has ventured into this topic, allowing continuous measurement of hemodynamic parameters in a non-obstructive and non-invasive manner [112,113]. One of the first experiments in pigs shows that this technique is a good candidate for the development of a new family of continuous non-invasive blood pressure monitors [7]. A characteristic to highlight of the EIT system used in this work is the generation of 50 fps, which makes the system a high performance hardware, such as that required in the pulmonary system. The authors of [114] and [115] present test on humans. In [114] regarding the measurement of systolic volume and [115] the detection of atherosclerosis. Both works show satisfactory results, despite the poor resolution of the images, due to the use of 16 electrodes unlike the 32 used by Solá and his colleagues in [7]. To monitor the pulmonary artery pressure through the use of a ring of 16 electrodes, Proença and his colleagues [9, 10], with 25 fps, estimated the blood pressure by measuring the transit time of pulse. These works make visible the potential of the EIT in this field. The in-vivo advances shown in [10] generate

Table 2.3: Characteristics of EIT in lung applications

Pathology	Number of electrodes	Frequency (kHz)	SNR	Current (mA)	Frames (fps)
Analysis of intrapulmonary gas distribution [76]	16	—	—	—	—
Evaluation of the effects of non-invasive ventilation during spontaneous breathing [6]	16	—	—	—	—
Lung impedance distribution measurement [14]	16	10-200	—	—	—
Measurement of pulmonary impedance distribution [55]	16	60-960	106.9		<131
Inhomogeneity detection of ventilation [76]	16	—	—	—	—
Mechanical ventilation distribution monitoring [77]	16	50	—	5	13
Pulmonary recruitment and endotracheal suction in ventilated premature infants [90]	16	—	—	—	44
Evaluation of pulmonary ventilation in neonates [91]	8	4-812.75	—	—	25
Air distribution evaluation in preterm infants [92]	16	50	—	—	—
Lung ventilation monitoring [107]	32	—	—	—	20
Tidal Volume Monitoring [88]	16	48	—	1	17
Evaluation of the level of instability of bronchopulmonary dysplasia [93]	16	2-1600	—	1.5	25
Real-time lung ventilation monitoring [108]	32	10-200	—	0.1 a 1	20
Lung impedance distribution monitoring [94]	32	10-200	56.3	0.1 a 1	20
Lung function monitoring [109]	32	10-200	—	0.1-8	30
Pulmonary embolism detection [78]	32	100	—	5	10
Pulmonary congestion classification [95]	5	—	—	—	—
Baseline selection for pulmonary impedance distribution [79]	16	110	—	9	50
Evaluation of pulmonary ventilation in patients with COPD [86]	16	50	—	5	33
Pulmonary ventilation study in different patient positions [80]	32	144	—	3	30
Pulmonary Function Evaluation [87]	16	—	—	—	—
3D lung function monitoring [88]	16	90	—	5	40
Quantification of pulmonary edema [81]	32	—	—	—	50
Assessing regional lung mechanic [96]	16	0.08-130	—	5	50
Monitoring of regional lung ventilation [97]	16	100	—	5	13
Regional lung perfusion estimation [83]	32	125	—	5-12	44
Monitoring of regional lung function [98]	16	50	80	5	33
Regional lung function determined [99]	16	—	—	—	33
Variation of poorly ventilated lung units [100]	32	—	—	—	48
Regional lung ventilation [101]	16	50	—	5	44
Changes in lung volume and ventilation [102]	16	100	75	5	44
Clinical diagnosis of lung abnormalities [103]	—	2-768	—	—	—
Measurement of regional pulmonary oxygen uptake [104]	16	50	75	5	25
Real-Time Detection of Hemothorax [84]	16	100	—	1	12
Hyperoxia affects the regional pulmonary ventilation/perfusion ratio [105]	32	125	—	5	50
Identification of regional overdistension [85]	16	—	—	—	40
Monitoring of volume lung [106]	16	100	—	5	44

Table 2.4: Characteristics of EIT in brain applications.

Phatology	Electrodes number	Frequency (kHz)	SNR (dB)	Current (mA)	Frames (fps)
Location of intracraneal hematoma [3]	8	50	–	1	–
Cerebral edema monitoring [20, 116]	16	50	80	1	1
Determination of the impedance of intracraneal tissues [117]	6	25	–	0.14	–
Focal monitoring of cerebral infarction [124]	16	50	–	1	1
Brian activity monitoring [42]	30	1.7	–	1	–
Brian activity monitoring [56]	16	50	83	1	1
Intracraneal hemorrhage detection [21]	32	10	–	–	20
Treatment of cerebral edema [73]	16	50	75	1	1
Imaging of cerbral perfusion [125]	57	2	–	0.05	5
Intracranial injury [126]	16	50	80	1	–
Monitoring brain injury [127]	16	50	–	1.25	–
Detection of brain tissue [128]	16	50	75	0.750	1
Intracranial hemorrhage [129]	16	50	75	0.5	3
Cerebral monitoring during total aortic arch replacement [130]	16	50	80	1	1
Activity brain monitoring [123]	114	1.475	–	0.05	–
Monitor regional cerebral edema [122]	16	50	80	1	–
Bioimpedance measurement of healthy and ischemic rat brain [121]	30	0.01 - 3	–	0.05	–
Long-term monitoring of dynamic brain electrical impedance tomography [119]	16	50	80	1	1
Quantification of intraventricular hemorrhage [120]	16	50	80	1	1
Monitoring of epileptic seizures [118]	8	50	–	0.05	1

an opportunity to develop EIT systems, with less demanding characteristics and good results; however, the methods based on the observation of the time series of certain pixels or regions, derived from the behavior of the impedance with the movement of the fluids (perfusion, breathing), intrinsically require high speed and high resolution simultaneously.

2.2.3 Cerebral monitoring

Miscellaneous investigations have been conducted to determine the impedance of head tissues with the aim to diagnose and monitor brain edemas, intracranial hemorrhage in both animal and human models, as well as in-vitro models. The Table 2.4 shows the different works that have been carried out in this field using EIT. The Table shows that for the same pathology there is no consensus in the number electrodes. However, studies agree in using one frame per second. Considering the frequency of the current signal most works used 50 kHz and 1mA. The in-vivo advances presented in [20, 21, 42, 56, 116–123] show the feasibility of using EIT in monitoring brain activity, detecting and monitoring cranial hemorrhages. Even if EIT systems presented in these references detect changes of impedance in cerebral fluids, there are aspects that require further exploration, such as selection of the optimal arrangement of electrodes and the best reconstruction algorithms.

2.2.4 Bladder monitoring

The so-called vesicoureteral reflux is a pathology that is presented by the leakage of urine from the bladder to the kidneys. This pathology can generate chronic renal failure, urinary tract infections, kidney infection, nephrotic syndrome, scarring of the kidneys, among other. For this reason, the EIT seeks to monitor the bladder volume and support the diagnosis of this pathology [131]. It is case of Li and colleagues [5], who designed an EIT system based on 16 electrodes, with the frequency range from 0 to 12.5 MHz. This system monitors the distribution of impedance in the bladder, and so establishes a close relationship between bladder volume and estimated conductivity in healthy patients. On the other hand, Schlebusch and collaborators [15, 73, 132, 133], with the aim of assist to paraplegic patients, which present decreased of bladder volume sensation due to damage to their neuronal structures, used the EIT to monitoring the bladder volume. The in-vitro experiments carried out in this work used a planar arrangement of 64 (8 x 8) electrodes, and not the classic ring arrangements. A feature to highlight in this application is the need of 1 frame per second to determine the bladder emptying.

GI index is based in the reconstruction matrix, which indicates the change in intensity of the pixels of the reconstructed image. This method shows good performance in bladder volume estimation when urine conductivity does not change from day to day; otherwise, volume can be over or underestimated [134,135] when considering constant urine conductivity, since the conductivity change generate error in estimation. Casterlar proposed to use an electrode into bladder to make volume estimation less sensitive to conductivity changes in urine [136]. This approach, although invasive, is robust against urine conductivity uncertainty.

2.2.5 Osseous system

Osteoporosis is another disease in which EIT has dabbled by determining bone mineral density (BMD). In [25], EIT is used for to estimate of the degree of osteopenia. This study focused on in-vitro tests, obtaining very good results, though due to the physiological characteristics of patients would present inaccuracies in the estimation. On [27], it was possible to identify the change in pelvic density, by applying a current with a frequency of 100 kHz to the patient. The experiments developed in this work demonstrated that is feasible to assess the severity of osteopenia through the estimation of BMD by EIT. The results presented in [27] were obtained on male patients, leaving a field of exploration in women.

Bone impedance can also become a support for forensic science, as it can help to determine the death time of an individual, as concluded in [24]; which, by measuring the electrical bioimpedance of the femur or tibia and the height of the subject established the time of death more accurately.

It is important to note that the number of electrodes used in the case studies in this subsection is small, 5 electrodes in [27] and 2 in [24].

2.3 Reconstruction image algorithms to EIT

EIT is a non-invasive image reconstruction technique, which offers a large field of action due to its low cost, portability and safety in handling [137]. In the medical field, this technique is applied to multiple medical conditions in organs located in the rib cage. One of the most studied organs is the lung, where the results of EIT are promising in the diagnosis of various pathologies [39].

The EIT image reconstruction search to solve two problems: i) the forward problem, that estimates the potential on the boundary electrodes, from the current injected to the object under study and supposing known the spatial distribution of the electrical conductivity. ii) the inverse problem, which estimates the conductivity distribution knowing the current and the potential on the electrodes. EIT images reconstruction requires the solution of both problems [138, 139].

Considering that image quality of the conductivity distribution depend on the performance of forward problem algorithm [140], several researches propose different alternatives to solve it. On the other hand, due to the nonlinear and ill-posed nature of the inverse problem, it is necessary a regularized solver to obtain a unique and stable solution [139]. In the following, the various alternatives for the solution of forward and inverse problem are presented.

2.3.1 Forward problem

The main problem in the EIT images reconstruction is the mathematical representation of the distribution of the electric potential, which is a system of equations poorly conditioned [137], and whose solution process is called a forward problem.

The forward problem solution requires a reference potential determined by the Dirichlet or boundary conditions. These conditions do not present problems in its implementation, but they can generate difficulties in the forward problem solution when analyzing heterogeneous regions [141]. These difficulties have been addressed through various solution methods, as mentioned below.

One of the most used methods for solving of forward problem, for its simplicity and its results, is the finite elements method (FEM) [138], although it has some disadvantages, such as the low signal to noise ratio (SNR) and the requirement of a large capacity for both processing and storage in memory [142]. In order to improve these aspects, research has been carried out to optimize this method, creating the generalized FEM method (GFEM), which shows better performance in terms of computational cost and SNR. This is why GFEM is a promising method for future studies in EIT. Other methods such as the border element method (BEM) [143] with promising results and the method called domain embedding method (DEM) [144], which combines the characteristics of the FEM and BEM methods, improves the solution of the direct problem in 3D. For this method only simulation results have been reported [144].

For a most accurate model for the EIT, the effects of the electrodes and the contact impedance between the electrolyte and the electrodes must be considered. The Complete Electrode Model (CEM) is the technique that consider these aspects, which is solved through FEM [145, 146]. This method has very good results in terms of computational cost; however, no comparisons have been made with other methods, thus leaving a gap for future research. On the other hand, the combined wavelet based mesh free (CWMF) method is suitable for representing domains with variable object geometries or mechanical movements; however, the CPU time is higher than for the FEM [147]. The results presented in [147] are based on simulation test on a 2D model.

Most of the above mentioned algorithms are analyzed in simulation. However, Zhang and collaborators [148] used the FEM method to analyze images of lungs obtained from a healthy volunteer of 33 years. In the references found in the systematic search performed, the method (FEM) is the only validated in humans.

Considering that most research on EIT image reconstruction employ the FEM for the forward problem, it is important to evaluate its performance versus others alternatives, with the aim to define the best approach for EIT image reconstruction.

2.3.2 Inverse problem

EIT image reconstruction or inverse problem is a nonlinear ill-posed problem and as a consequence it is difficult to obtain stable and reliable results especially in-vivo experiments [149]. Hence, researchers propose different alternatives to face the reconstruction of EIT images, as the mentioned below.

EIT image reconstruction is a nonlinear problem; however, linearized approximations have proved to be very useful. Backprojection is a linear reconstruction algorithm proposed by Barber and Brown [150, 151] and it is the simplest to implement and one of the most common image reconstruction techniques used in EIT [152]. It has also been widely used in clinical experimental [150]. Other linear approach is the one-step linearized Gauss–Newton (GN) solver, which calculates a linear reconstruction matrix that is used to obtain rapid, real-time EIT imaging [153, 154]. Conjugate Gradient iteration is a technique for solving linear systems, which projects the space dimension of a problem in a Krylov subspace with lower dimension [155].

Others alternatives to solve the inverse problem are iterative algorithms; such as GN, which is the most popular to solve nonlinear minimization. This approach is based on least squares minimization [156,157]. The non-linear Newton–Raphson (NR) iteration approach involves the construction and repeatedly Cholesky decomposition of the sensitivity matrix, showing fast convergence for 2D EIT, but unsuitable for 3D EIT [158, 159]. For complex ill-conditioned large scale applications, the non-linear conjugate gradient (CG) algorithm is recognized as one of the most suitable numerical algorithms [159,160]. Other alternative is the Primal and Dual Interior Point Method (PDIPM), which is based on the conversion of non-differentiable problems into equivalent differentiable problems by introducing dual

variables using the Cauchy-Schwartz inequality [161, 162]. On other hand, formulating the inverse problem as a state-estimation problem gave rise to the approach of EIT image reconstruction based on Kalman filter, which allow tracking fast of impedance changes [163, 164].

The neural networks are an other option for EIT image reconstruction. In [165] shows that the Radial Basis Neural Networks (RBNN) and Hopfield Neural Networks (HNN) have the better accuracy than GN algorithm, becoming a good alternative for medical applications. The D-Bar method employs convolutional neural networks trained with simulated data. The results presented in [166] indicates that this method requires a minimal reconstruction time when compared with other approaches.

The different alternatives for inverse problem solver, leave a field of exploration to determine the best approach based in the accuracy of image reconstruction. The EIDORS (Electrical Impedance Tomography and Diffuse Optical Tomography Reconstruction Software) is an widely-used open-source platform that contains several algorithms to solve the forward and inverse problems for EIT; whereby, we will use it in performance analysis of the EIT image reconstruction.

2.4 Conclusions

The state of the art presented in the current chapter defined the following aspects of this thesis work:

- Bladder volume monitoring does not require a high temporal resolution, being 1 fps enough for most applications. Despite this, the main barrier for its massive adoption is that uncertainty in urine conductivity leads to over or under estimation of bladder volume. This problem has motivated one of the contributions of this work, which is the development of a FIM Approach, that according to our experimental results is robust against conductivity uncertainty.
- The EIT system to be designed must generate a current signal not exceeding 1 mA at a frequency of 50 kHz, which are the predominant characteristics in medical applications of the EIT.
- The existence of several alternatives for EIT image reconstruction prompted us to conduct a quantitative study oriented to find the best method for bladder monitoring applications.
- EIT systems for bladder monitoring use 16 electrodes in different configurations with promising results. The reduction of spatial resolution is an aspect that will be analyzed in this project; looking for an efficient bladder monitoring with 8 electrodes, which reduces the complexity of the hardware to be designed.

3 Theoretical background

3.1 Introduction

The EIT is a technique to study the conductivity distribution of an object or a biological tissue [167]. The electrical properties of the tissues or regions of the body are used to determine diseases and to monitor a biological process. In addition to be free of ionizing radiation and low cost, EIT has demonstrated promising results in medical applications [168].

The EIT images reconstruction implies the solution of a nonlinear and ill-posed mathematical problem [169], so many researchers have proposed optimization methods to find numerically stable solutions. The accuracy of EIT images reconstruction depends on the method used; for this reason a quantitative analysis to establish the best method is necessary. In this chapter, we describe four performance indexes: correlation coefficient, percentage of error, absolute error, and relative error, to define the best option of EIT image reconstruction.

Not only the electrical properties of tissues can be analyzed by EIT, size is another property that can be estimated with this technique. The GI index, that has shown promising results in volume estimation, requires the reconstruction matrix (R^f), which relates the pixels of an EIT image with the estimated conductivity [135], and that is calculated using EIT image reconstruction algorithms. GI is obtained by summing all pixel values of the image vector (I^f). Another alternative for volume estimation is the FIM, a method created at Dhaka University [170], which consists of the sum of orthonormal tetrapolar potential measurements obtained from electrodes located around a target area [171]. Approaches such as the Impedance Ratio Method (IRM) [133] and Voltage Change Ratio (VCR) [74] establish a close relationship between volume and the tetrapolar measurements of impedance and voltage, respectively.

In this chapter is show the mathematical concepts about EIT, performance indexes to EIT image reconstruction and the volume estimation.

3.2 Electrical Impedance Tomography (EIT)

The Figure 3.1 presents the concept of the EIT, which consists of applying currents (I) on a set of electrodes connected on the boundary ($\partial\Omega$) of a body (Ω); subsequently, the resulting voltages (V) are measured on the remaining electrodes. The mathematical background of the EIT is explained in [172]; where Maxwell equations and the Faraday and Ampere laws are formulated in differential form to define the relationship between the admitivity (γ) and the potential on the electrodes (ϕ) (Equation 3.1).

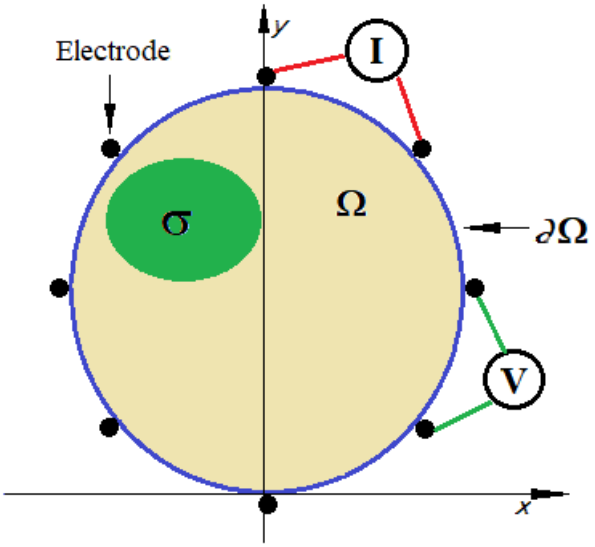

Figure 3.1: Conductivity changes detection with EIT.

$$\nabla \cdot (\gamma \nabla \phi) = 0 \tag{3.1}$$

γ is a complex value $\gamma = \sigma + j\omega\varepsilon$ where σ represent the conductivity, $i \triangleq \sqrt{-1}$ is the imaginary unit, ω denotes the angular frequency and ε is the permitivity. This equation describes the electrical potential inside Ω. Whenever Ω is stimulated with low frequency currents ($\omega \approx 0$), the following EIT equation is obtained

$$\nabla \cdot (\sigma \nabla \phi) = 0 \tag{3.2}$$

The non-linear partial differential equation 3.2 has infinite solutions. Particular solutions are obtained applying either the Dirichlet or Neumann conditions. The former are used when voltages are applied to the boundary electrodes:

$$\phi(x_i) = v_i, \qquad i = 1, 2, \ldots, m \tag{3.3}$$

Where x_i is a point on $\partial\Omega$ that indicates the position of the electrode i, v_i is the voltage applied to such electrode, and m is the total number of electrodes. Neumann conditions are used when currents are injected and drained through the surface electrodes. In such a case:

$$\sigma\nabla\phi(x_i)\cdot\overrightarrow{n} = I_i, \qquad i = 1, 2, \ldots, m \tag{3.4}$$

Where $\overrightarrow{n}$ is a unitary vector perpendicular to $\partial\Omega$ in x_i. I_i is the current density through the electrode i and it is positive for the injecting electrode and negative for draining electrode. Additionally, Kirchoff's current law must be satisfied:

$$\sum_{i=1}^{m} I_i = 0 \tag{3.5}$$

The solution of the EIT problem is divided into two parts: i) estimate the potentials on boundary knowing the injected current and assuming a conductivity distribution, this part is called forward problem and ii) assess the conductivity distribution knowing the injected currents and the measured potentials or inverse problem (Figure 3.2). The forward and inverse problems are detailed below.

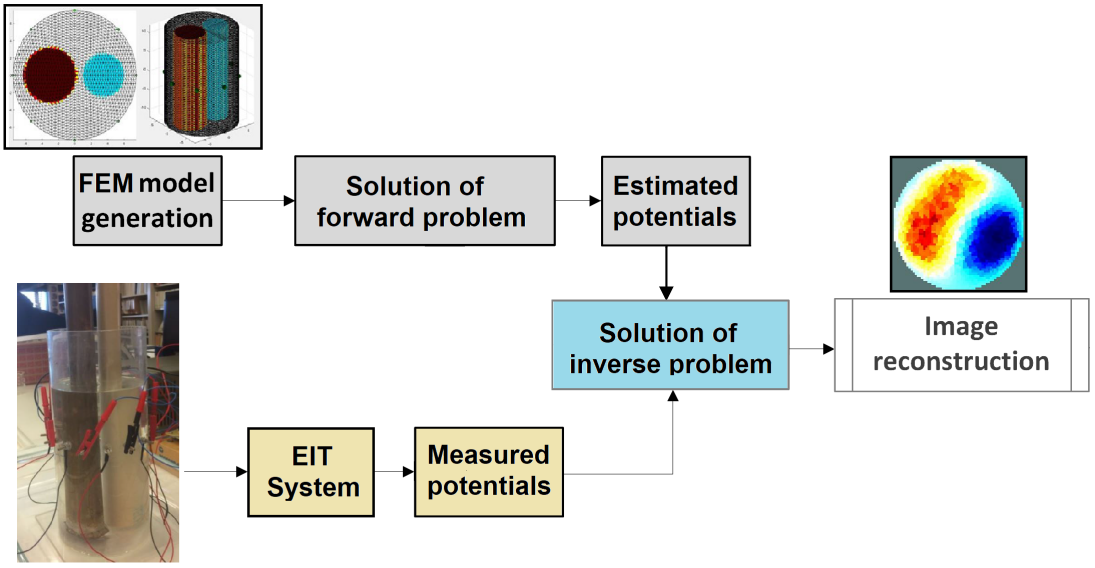

Figure 3.2: EIT image reconstruction.

3.2.1 Illustrative example of the analytical solution of the Laplace's equation

In the system presented in Figure 3.3, the internal disk has conductivity σ_i and radius R_i; for the external disk these values are σ_e and R_e, respectively. Normalized polar

coordinates will be used to calculate the electric potential in both disks. We mean by normalized that the radius r will be the quotient between the physical radius r' and R_e. In this manner, the first polar coordinate will a be a real number in the interval $[0, 1]$. This choice is made to simplify calculations of the potential at $\partial\Omega$, which is defined as $\partial\Omega = \{(1, \theta) \mid \theta \in [0, 2\pi)\}$. In the following, θ will denote an angle in the interval $[0, 2\pi)$.

The potential in the inner and outer disks will be defined as $\phi_i(r\prime, \theta)$ and $\phi_e(r\prime, \theta)$,

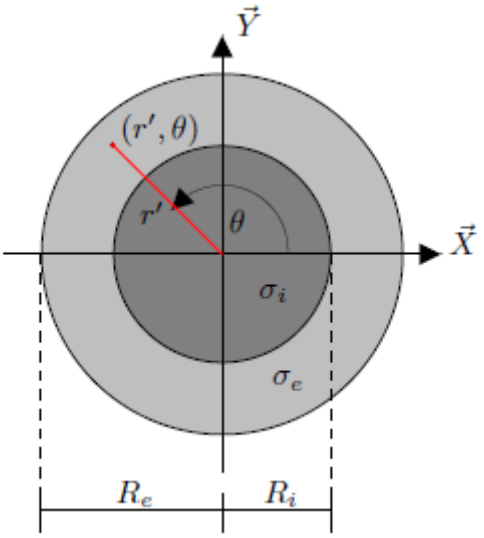

Figure 3.3: Concentric disks of different conductivity.

respectively. Both of them must satisfy the Laplace equation (3.6)

$$\begin{aligned} \nabla \cdot \nabla \phi_i &= 0 \\ \nabla \cdot \nabla \phi_e &= 0 \end{aligned} \tag{3.6}$$

In polar coordinates, these equation can be rewritten as:

$$\begin{aligned} \frac{\partial^2 \phi_i}{\partial r^2} + \frac{1}{r}\frac{\partial \phi_i}{\partial r} + \frac{1}{r^2}\frac{\partial^2 \phi_i}{\partial \theta^2} &= 0 \\ \frac{\partial^2 \phi_e}{\partial r^2} + \frac{1}{r}\frac{\partial \phi_e}{\partial r} + \frac{1}{r^2}\frac{\partial^2 \phi_e}{\partial \theta^2} &= 0 \end{aligned} \tag{3.7}$$

Since the potential must be continuous at $r = \alpha$, with α defined as the normalized radius of the internal disk $\alpha \triangleq R_i/R_e$, the following constraint is added:

$$\phi_i(\alpha, \theta) = \phi_e(\alpha, \theta), \qquad \forall\theta \tag{3.8}$$

Another requirement for potentials is the continuity at $r = \alpha$ of the current density normal component. Since polar coordinates are used, the normal component of $\nabla\phi$ is given by:

$$\begin{aligned} \nabla\phi \cdot \vec{n} &= \begin{bmatrix} \dfrac{\partial\phi}{\partial r}, & \dfrac{1}{r}\dfrac{\partial\phi}{\partial\theta} \end{bmatrix} \begin{bmatrix} 1 \\ 0 \end{bmatrix} \\ &= \frac{\partial\phi}{\partial r} \end{aligned} \tag{3.9}$$

Using the property (3.9), the current density conditions can be written as follows:

$$\sigma_i \frac{\partial\phi_i(\alpha,\theta)}{\partial r} = \sigma_e \frac{\partial\phi_e(\alpha,\theta)}{\partial r}, \qquad \forall\theta \tag{3.10}$$

Using again the property (3.9), the boundary condition is:

$$-\sigma_e \frac{\partial\phi_e(1,\theta)}{\partial r} = j(\theta), \qquad \forall\theta \tag{3.11}$$

Where $j(\theta)$ is a known function that indicates the current density at each point of $\partial\Omega$. In summary, the potentials ϕ_i and ϕ_e are two functions satisfying the equations (3.6), (3.8), (3.10), and (3.11). These functions are written as linear combinations of harmonically related solutions of (3.6)

$$\begin{aligned} \phi_i(r,\theta) &= \sum_{k=0}^{\infty} a_k\, r^k\, e^{i\,k\,\theta} \\ \phi_e(r,\theta) &= \sum_{k=0}^{\infty} \left[b_k\, r^k + c_k\, r^{-k}\right]\, e^{i\,k\,\theta} \end{aligned} \tag{3.12}$$

The coefficients a_k, b_k and c_k, which are the unknowns of the problem, are calculated from the equations (3.8), (3.10), and (3.11). Taking the derivatives of the potential with respect to r we obtain:

$$\begin{aligned} \frac{\partial\phi_i(r,\theta)}{\partial r} &= \sum_{k=1}^{\infty} a_k\, k\, r^{k-1}\, e^{i\,k\,\theta} \\ \frac{\partial\phi_e(r,\theta)}{\partial r} &= \sum_{k=1}^{\infty} \left[b_k\, k\, r^{k-1} - c_k\, k\, r^{-k-1}\right]\, e^{i\,k\,\theta} \end{aligned} \tag{3.13}$$

The above equations begin with $k = 1$ given that these functions become zero at $k = 0$. The current density at the boundary of the external disk ($r = 1$) is described using the same base of orthogonal functions used for ϕ_i and ϕ_e

$$j(\theta) = \sum_{k=1}^{\infty} w_k\, e^{i\,k\,\theta} \tag{3.14}$$

Replacing (3.13) and (3.14) in to (3.8), (3.10), and (3.11), the follow system of equations is obtained:

$$\begin{bmatrix} \alpha^k & -\alpha^k & -\alpha^{-k} \\ \sigma\, k\, \alpha^{k-1} & -k\, \alpha^{k-1} & k\, \alpha^{-k-1} \\ 0 & -k & k \end{bmatrix} \begin{bmatrix} a_k \\ b_k \\ c_k \end{bmatrix} = \begin{bmatrix} 0 \\ 0 \\ w_k \end{bmatrix}, \qquad k = 1, 2, \ldots \tag{3.15}$$

The solution of (3.15) leads to the following potential for the internal disk:

$$a_k = \frac{-2\, w_k}{k\,(\sigma + 1 + \alpha^{2k}\,(\sigma - 1))}$$

$$b_k = \frac{-w_k\,(\sigma + 1)}{k\,(\sigma + 1 + \alpha^{2k}\,(\sigma - 1))} \tag{3.16}$$

$$c_k = \frac{w_k\, \alpha^{2k}\ (\sigma - 1)}{k\,(\sigma + 1 + \alpha^{2k}\,(\sigma - 1))}$$

When a_k is replaced in the equation that describes ϕ_i, the following potential is obtained:

$$\phi_i(r, \theta) = -\sum_{k=1}^{\infty} \frac{2\, w_k}{k\,(\sigma + 1 + \alpha^{2k}\,(\sigma - 1))}\, r^k\, e^{i\, k\, \theta} \tag{3.17}$$

From b_k and c_k, it can be shown that the potential for the external disk is as follows:

$$\phi_e(r, \theta) = -\sum_{k=1}^{\infty} \frac{w_k}{k} \left[\frac{1 - \mu\, \alpha^{2k}\ r^{-2k}}{1 + \mu\, \alpha^{2k}} \right] r^k\, e^{i\, k\, \theta} \tag{3.18}$$

with:

$$\mu = \frac{\sigma - 1}{\sigma + 1} \tag{3.19}$$

This theoretical result will be used in the Results chapter to compare the methods FIM of 4 electrodes (FIM-4), IRM, and VCR, with respect to their capacity to estimate the radius of the internal disk, when its conductivity is unknown. These methods will be explained in the Section 3.5 of this chapter.

3.2.2 Forward problem

The forward problem can be solved analytically or numerically. The analytical methods are preferable as computation time is reduced, however their usage is limited to a few idealized geometries [173, 174]. For numerical solutions, the governing equation are discretized using the finite elements method (FEM) or the generalized FEM (GFEM) [175]. For general geometries and inhomogeneous materials, FEM is well suited to solve the forward problem and is the most used in EIT [138, 142, 145, 147, 176–178]. In EIT, the

approach based on FEM, consists in dividing Ω into a finite number of regions of constant conductivity. A relation can be obtained between the voltage measurements on the boundary and the conductivity of such regions (Eq 3.20) [176, 179, 180].

$$\Phi = \boldsymbol{J}\sigma \tag{3.20}$$

Where $\boldsymbol{J}$ is known as the sensitivity matrix or Jacobian matrix, which relates vector of voltage measurements (Φ) with vector of conductivities (σ). If σ and $\boldsymbol{J}$ are known. Then the estimation of Φ is simple. Considering the variety of methods available in EIDORS, this project will analyze the best alternative for solving the forward problem in this section.

3.2.3 Inverse problem

The inverse problem seeks to obtain the conductivity distribution using the potential on the electrodes and the injected currents. To solve the inverse problem is necessary to use a forward model to minimize the difference between the potentials estimated and measured on the boundary (Figure 3.2). There are several approaches to solve the inverse problem, which is ill-posed and is based on linearization and regularization [174]. The conductivity estimation obtained from 3.2 is:

$$\boldsymbol{J}^T\Phi = \boldsymbol{J}^T\boldsymbol{J}\sigma \tag{3.21}$$

$$\sigma = (\boldsymbol{J}\boldsymbol{J}^T)^{-1}\boldsymbol{J}^T\Phi \tag{3.22}$$

The matrix $(\boldsymbol{J}\boldsymbol{J}^T)$ is ill-conditioned. The best way to solve this problem is to use regularization techniques [160]; which are necessary to obtain a unique solution from a ill-posed EIT problem [181]. Additionally, a regularized solution of the inverse problem improves the reconstructed image quality [182, 183]. For the these reasons, many regularization methods, such as Tikhonov [184–186], Laplace [187–189], Total Variation [162, 190, 191], Noser [187, 192, 193], Helmholtz- Type [188], projection error propagation-based [182, 183, 194], have been proposed.

In [195] is presents the different electrical proprieties of human tissues, so is possible to determine the conductivity of internal tissues of a section of body through EIT. The conductivity distribution estimation of different tissues within a cross section of a body is called absolute EIT image. Absolute EIT images generally requires iterative reconstruction methods whose convergence depends on a priori information such as the shape and the size of the tissue, and also the position of the electrodes. Nevertheless, in in-vivo test these details are not always available. An alternative to the absolute approach is the differential EIT, in which the images are obtained by comparing measures with respect to reference values previously obtained. This last approach will be used in the present work.

3.3 Sensitivity maps of impedance measurement

The sensitivity distribution of an impedance measurement determines impedance change caused by a given change in conductivity distribution. The sensitivity distribution also establishes the impedance contribution of each region within the area under study. The sensitivity map is the superposition of all the sensitivity distributions corresponding to each measurement [196].

Based on Geselowitz's theorem [197], a study of sensitivity maps for the FIM, GI, VCR and IRM approaches will be performed, based on the calculation of sensitivity distribution given by:

$$J_{dmk} = \frac{\partial V_{dm}}{\partial \sigma_k} = -\int \bigtriangledown u(I^d) \cdot \nabla u(I^m) dV \tag{3.23}$$

where $u(I^d)$ is the potential for the dth driving pattern and $u(I^m)$ is the potential for the mth driving pattern [198]. The sensitivity maps for the electrode arrangement of each approach will be carried out using simulated FEM models in EIDORS, which will indicate the regions of the greatest contribution in the impedance measurement.

3.4 EIT images analysis

In the last decades EIT research community has focused their attention in metrics such as spatial and temporal resolution, accuracy and signal-to-noise ratio; which are used to assess the quality of EIT images.

3.4.1 Spatial and temporal resolution for EIT image

Spatial resolution of EIT depends on the accuracy and noise level of the measurements, the number of electrodes, and the reconstruction algorithm used. For this reason, spatial resolution is an important parameter for the analysis of EIT image reconstruction [199]. The spatial resolution was addressed in this project as follows.

3.4.1.1 Accuracy indexes

Usually, the accuracy indexes most frequently used to test reconstruction algorithms are the Pearson's correlation coefficient (CC) and percentage of error (PE); which perform comparative process between a FEM model and a reconstructed EIT image. These indexes will be used in this work to identify the best alternative for EIT image reconstruction

employing the algorithms available in EIDORS. CC and PE are described by the equations 3.24 and 3.25 respectively.

$$CC = \frac{\sum_{i=1}^{N}\sum_{j=1}^{M}\left(\left(R_{ij}-\bar{R}\right)\left(A_{ij}-\bar{A}\right)\right)}{\left(\sum_{i=1}^{N}\sum_{j=1}^{M}\left(\left(R_{ij}-\bar{R}\right)^{2}\left(A_{ij}-\bar{A}\right)^{2}\right)\right)^{1/2}} \tag{3.24}$$

$$PE = \frac{\sum_{i=1}^{N}\sum_{j=1}^{M}\left(\left(R_{ij}-A_{ij}\right)\right)}{\sum_{i=1}^{N}\sum_{j=1}^{M}\left(R_{ij}\right)} * 100 \tag{3.25}$$

Being R the pixels intensity matrix of the reconstructed reference image, A the pixels intensity matrix of the reconstructed image under analysis, $\bar{R}$ and $\bar{A}$ the mean of the values of each matrix (Eq. 3.26).

$$\bar{X} = \frac{1}{N * M}\sum_{i=1}^{N}\sum_{j=1}^{M} X_{ij} \tag{3.26}$$

The indexes mentioned above are used to compare inverse problem solution algorithms. The performance of the forward problem solvers is evaluated by the difference between the potentials estimated on a FEM model and the potentials measured on a phantom. The absolute error (E_{Abs}) and relative error (E_{relat}) are calculated according to the equations 3.27 and 3.28, respectively.

$$E_{Abs} = \frac{|V_{meas} - V_{estim}|}{N_{meas}} * 100 \tag{3.27}$$

$$E_{relat} = \frac{\left|\frac{V_{meas}}{V_{estim}} - 1\right|}{N_{meas}} * 100 \tag{3.28}$$

V_{meas} are the measured potentials, V_{estim} the estimated potentials and N_{meas} the number of measurements. A graphical user interface (GUI) EIDORS-Matlab was implemented to study the performance of algorithms that solve the forward and inverse problems. The GUI allows to compare the performance indexes of two algorithms simultaneously.

3.4.2 Signal-to-noise ratio (SNR) and frames frequency

The SNR is to calculate through the mean and standard deviation of the potential measurements (equation 3.29) [200] and the frames frequency is to obtain varying the time to perform a measurement on each electrode; the measure time with best SNR define the frames frequency.

$$SNR = 20log\left(\frac{Mean\left(m_i\right)}{std\left(m_i\right)}\right) \tag{3.29}$$

being m_i the potential measured on the electrode i.

3.5 Volume estimation with bioimpedance

This chapter presents the GI, FIM, IRM, and VCR techniques, which have been recently proposed for volume estimation in medical applications.

GI is defined as the sum of the pixels of an image and as a consequence it requires to solve the EIT inverse problem. On other hand, FIM approach does not need the reconstruction matrix; the potential variation is enough to estimate volume. FIM estimates the impedance of the region of interest by means of two potential measurements mutually perpendicular giving a higher sensitivity in the central region compared to its surroundings [201]. Similar as FIM method, IRM and VCR do not require of an image reconstruction algorithm. IRM, proposed in [133], estimates the volume estimation of an object employing three impedance measurements. On the other hand, VCR requires two voltages measures to estimate the volume [74], although the robustness against uncertainty of conductivity has not been analyzed. The GI, FIM, IRM, and VCR are explained below.

3.5.1 Global impedance index

The GI approach is based on reconstructed images of differential EIT (dEIT), in which homogeneous (v_h) and non-homogeneous (v_{nh}^f) vector measurements are taken. The superscript f, which ranges from 1 to N_f, indicates the frame. N is the number of voltage measures per frame and is hence the number of elements of vectors v_h and v_{nh}^f. Differences between v_h and v_{nh}^f are used in an EIT reconstruction algorithm to calculate changes of conductivity inside the object under study [17, 132, 134]. Hence, variations in potential for any frame f are calculated using the following operation:

$$\Delta v^f\,(k) = \frac{v_{nh}^f\,(k) - v_h(k)}{v_h(k)}, k{=}1,...\mathrm{N} \tag{3.30}$$

where $\Delta v^f(k)$, $v_{nh}^f(k)$ and $v_h(k)$ are the k-th elements of the vectors Δv^f, v_{nh}^f, and v_h, respectively. To solve the pixel conductivity vector I^f, the matrix R^f must be calculated using a differential EIT reconstruction algorithm. R^f has M rows and N columns (M, number of pixels of the conductivity image). Hence, the vectors I^f and Δv^f are related by equation 3.31 as follows:

$$I^f = R^f \Delta v^f \tag{3.31}$$

GI of dimensionless units is calculated by adding the values of all pixels of I^f for each frame as follows (equation 3.32):

$$GI = \sum_{f=1}^{N_f} \sum_{k=1}^{N} I^f(k) \tag{3.32}$$

Because the EIT system has 8 electrodes and because voltages at the injection electrode and at its two nearest neighbors are not measured, $N = 40$, corresponding with 8 current injections and 5 voltage measurements for each frame. The reconstruction matrix is calculated from a 2D EIT image of 32 by 32 pixels. Therefore, R^f has 1024 (32^2) rows and 40 columns and was solved using a cubic finite element model of 37412 elements implemented in EIDORS.

3.5.2 Focused impedance measurement (FIM)

FIM Method is a technique of impedance measurement that can localize a zone of interest in a volume, eliminating effects of neighboring regions and using 8, 6 or 4 electrodes [171, 202–205]. FIM shows promising results in gastric monitoring [170], breast tumors [206] and lung ventilation [207]. We propose a modification of the FIM approach using 8 electrodes; the classical FIM and modified FIM are explained then.

3.5.2.1 Classic FIM method

Tetrapolar FIMs are based on the sum of independent measurements of mutually perpendicular and concentric potentials. This is done to detect changes that are generated by the injected current on the equipotential lines inside the object under study. Saha and collaborators [208] show that changes in conductivity/impedance of the object under study lead to proportional differences in electrical potential between equipotential lines. This assumption remains valid for a constant injected current.

The arrangement of electrodes for FIM is shown in Figure 3.4. When the current is injected through the E_0 and E_2 electrodes, equipotential lines are represented as $a - a'$ and $b - b'$. Similarly, when current is injected through the E_1 and E_3 electrodes, then the equipotential lines are represented as $c - c'$ and $d - d'$. These potentials are measured on electrodes E_4, E_5, E_6 and E_7, and the focused area **O** is defined for equipotential lines [209].

Changes in potential are estimated relative to the reference measure P_{ref}, which is the potential when there is no object in the region **O** of Figure 3.4. In this case, the conductivity is homogeneous throughout the cross section under study. P_{ref} is calculated using equation 3.33 as follows:

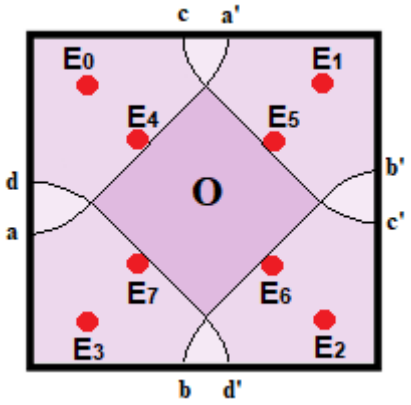

Figure 3.4: Focused area in an 8-Electrodes FIM arrangement.

$$P_{ref} = P^{o}_{4,6} + P^{o}_{5,7} \tag{3.33}$$

$P^{o}_{4,6}$ is the difference in potential between the electrodes E_4 and E_5 for the homogeneous configuration (indicated with the superscript ^{o}). Similarly, $P^{o}_{5,7}$ is the difference in potential between the electrodes E_5 and E_7. Hence, given a conductivity change in region **O** (Figure 3.4), the potential is defined in equation 3.34 as follows:

$$P = P_{4,6} + P_{5,7} \tag{3.34}$$

The variability of potential is then defined as:

$$\Delta P = \frac{P - P_{ref}}{P_{ref}} \tag{3.35}$$

The opposite pattern for injection and measurement using the classic FIM approach has been applied in previous studies [210, 211], but in bladder volume estimation shows poor robustness due urine conductivity uncertainty, as will be demonstrate in results chapter.

3.5.2.2 Modified FIM method

We propose a modified FIM approach which employs adjacent patterns for injection and measurement, using the same electrode arrangement of FIM classic. For this purpose, the electrodes were divided into externals (E_0, E_1, E_2, and E_3) and internals (E_4, E_5, E_6, and E_7) according to the configuration presented in Figure 3.4. The Table 3.1, shows the injection and measurement electrodes used for the two proposed FIM approaches.

In the first proposed FIM approach, FIM-I (I, internal), the variable P of equation 3.35 was equal to P_{int}, which is calculated as P_{int}=$P_{4,5}$+$P_{5,6}$+$P'_{5,6}$+$P_{6,7}$. In the second proposed

Table 3.1: Injection and measurement patterns for the proposed FIM approaches

	Injection	Measurement	
Potentials on internal electrodes	E_0 - E_1	$P_{4,5}$	$P_{5,6}$
	E_1 - E_2	$P'_{5,6}$	$P_{6,7}$
	E_4 - E_5	$P_{6,7}$	
	E_5 - E_6	$P_{4,7}$	
Potentials on external electrodes	E_4 - E_5	$P_{0,1}$	$P_{1,2}$
	E_5 - E_6	$P'_{1,2}$	$P_{2,3}$

approach, FIM-IE (IE, Internal-External), $P = P_{int} + P_{ext}$ with P_{ext}=$P_{0,1}$+$P_{1,2}$+$P'_{1,2}$+$P_{2,3}$ and P_{int} as for FIM-I. In the previously described FIM-4 approach [167], variable $P = P_{4,7} + P_{6,7}$. As indicated in Table 3.1, FIM-I requires two injections of current and four measures of voltage, whereas FIM-IE requires four injections of current and eight measures of voltage. In contrast, classic FIM-4 requires two injections of current and two measures of voltage. P_{ref} for each approach is defined as P.

3.5.3 Impedance Ratio Method (IRM)

IRM relates volume with impedance change. This technique search the volume estimation robustness against the conductivity variability of the object under study. The three tetrapolar measurements required to calculate the impedance ratio are presented in Figure 3.5 [133]. The frontal measurement is used to calculate $Z_f = V_f/I_f$, backward measurement defines $Z_b = V_b/I_b$, and the side measurement determines $Z_s = V_s/I_s$. The potentials and the currents are measured and injected on boundary electrodes, which are placed in a ring arrangement. The measurements proposed in [133] present higher sensibility of impedance variations; assuming that the object under study must be close of the electrodes, being that, the current densities are biggest in the vicinity of these. Therefore, the increasing of volume object implies higher change in sensitivity of impedance measurements. The equation 3.36 defines the IRM.

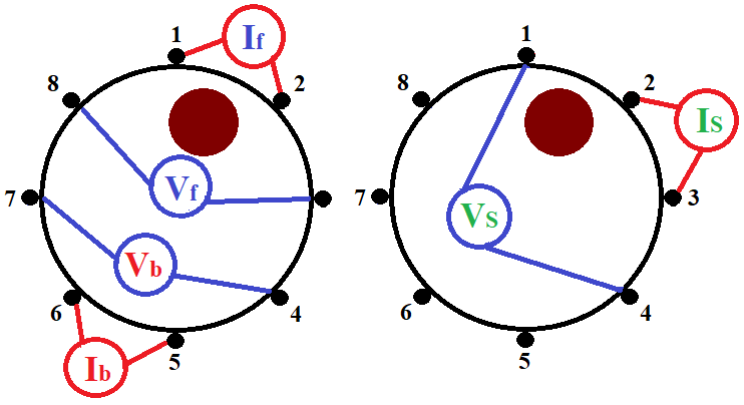

Figure 3.5: Injection and measurement of signals for IRM

$$IR = \frac{Z_s - Z_f}{Z_b - Z_f} \tag{3.36}$$

3.5.4 Voltage Change Ratio (VCR)

VCR [74] associates the voltage change with the volume of the object under study. This is calculated considering a reference measurement (V_0), which is obtained when the object studied has the lowest volume. Others potentials measurements (V) are taken during the volume increasing to determine the VCR (Eq. 3.37).

$$VCR = \frac{|V - V_0|}{V_0} \tag{3.37}$$

The electric potentials are measured considering the electrode configuration shown in Figure 3.6.

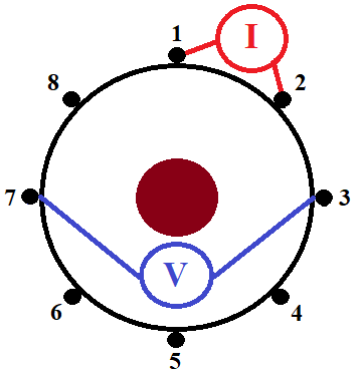

Figure 3.6: Injection and measurement of signals for VCR.

VCR index uses two voltage measurements only, one reference and the other to determine the change in volume; in order to have redundant voltage measurements, the modified VCR (MVCR) is proposed. The MVCR requires 8 voltage measurements, as indicated in Figure 3.7. The MVCR is calculated using the equation 3.38.

$$MVCR = \frac{\sum_{i=1}^{8} \frac{|V_i - V_0|}{V_0}}{n} \tag{3.38}$$

Where n is the number of voltage measurements and V_0 is the reference voltage obtained when the current is injected by electrodes 1 and 2 and the studied object has the lowest volume.

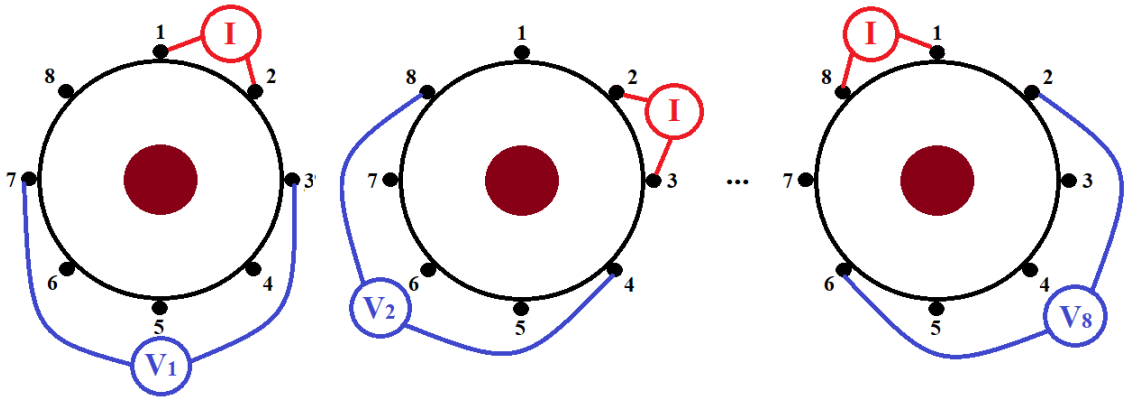

Figure 3.7: Injection and measurement of signals for MVCR.

3.6 Summary

This chapter presented the GI, FIM, IRM, and VCR methods for volume estimation. The first approach requires to apply EIT image reconstruction algorithms, which are selected using the performance indexes correlation coefficient and percentage of error describes in the equations 3.24 and 3.25, respectively. In contrast, FIM, IRM, and VCR necessitate only the potential on the electrodes and very simple mathematical expressions, such as 3.35, 3.36, and 3.37.

One of the contributions of this work is the FIM approach described in Section 3.5.2.2, and the other one the low cost EIT system presented in Section 4.3.

4 Materials and Methods

4.1 Introduction

This chapter describes the proposed low-cost EIT system. This prototype has 8 channels for injection and measurement of signals. In addition, the injection and measurement patterns are easily reconfigurable by updating the internal registers of the AFE4300 device, which is the main component of our EIT system. Others AFE4300 functions are the generation of a 294.5 μA_{rms} current signal and an internal full-wave rectifier responsible for delivering the estimated conductivity, which is sent via Bluetooth to a PIC16F886 microcontroller. The PIC16F886 manages the registers of the AFE4300 and communicates the EIT system with the computer where the measurements are stored. Also, the AFE4300 has the functionality to measure impedance directly between the surface electrodes [212]. Not only the electrical properties of tissues can be analyzed by EIT, size is another property that can be estimated with this technique.

The four mentioned approaches in the previous chapter for volume estimation (GI, FIM, IRM, and VCR) were evaluated using three bladder phantoms that emulate the conductivity of the internal tissues of the lower pelvis. Each phantom has a cylindrical cavity filled up with a saline solution that emulates urine. The conductivity of this solution was changed across different trials to study its effect on volume estimation.

This chapter describes the design of the low cost EIT system, and the phantoms used for the volume estimation tests.

4.2 Electrode arrays and injection and measurement patterns

The number and geometric arrangement of the electrodes is an important parameter to consider for the implementation of EIT systems. There are works that show a promise

performance of EIT in the bladder monitoring using different electrode arrangements. In this field, the simple ring is the most frequently employed [5,46,135]; nonetheless, double ring [46,135], semicircular [46,74,213], matricial [46,135,192,214], and linear [46,135,215] are also used. The above mentioned works are based on EIT systems of 16 electrodes; on other hand, [133] shows a study with 8 electrodes in simple ring configuration, being a good alternative to estimate bladder volume.

Injection and measurement patterns are other aspects to consider in EIT image reconstruction; although the adjacent pattern for injection and measurement is the predominant method in medical applications of EIT [68], patterns such as opposite, cross and trigonometric have also been used to study the performance of EIT. In [216] it is asserted that the opposite pattern presents better SNR than the adjacent, in tests on chicken meat tissue. Adler and his colleagues [68] do not recommend the adjacent method for injection and measurement due to its poor performance. Silva and his collaborators [51], using a 3D simulation, conclude that the opposite method is the worst option due to the effects of noise in the measurement of potentials. These results are obtained considering more than 16 electrodes.

Other injection and measurement techniques have shown promising results, such as [217], where methods called parallel and bypass are presented. They determine abdominal fat employing 32 electrodes.

Considering the above mentioned studies regarding the arrangement of electrodes and injection and measurement patterns, it is important to analyze the effects of these on the reconstruction of EIT images with 8 electrodes in bladder monitoring. In this work, we study five configurations: (i) ring (RG), (ii) semicircular (SC), (iii) coronet (CN), (iv) 2 vertical lines (V2L) and (v) 2 horizontal lines (H2L), which were evaluated on a finite element model (FEM) of the lower pelvis (Figure 4.1). In the first part of the present study, which was carried out through simulation, the bladder was represented by spheres of different radius. This radius was varied from 0.05 to 0.19 m with steps of 0.05 m, to determine the performance of these electrode configurations and the injection and measurement patterns adjacent and opposite on the accuracy of the estimation of the bladder volume. After using the EIDORS software to establish the best electrode arrangement and the best injection and measurement patterns for spheres volume estimation, we conducted experiments with the designed EIT measurement system, a saline tank (4g/L), and three steel spheres with a radius of 27.5, 35.0 and 37.5 mm. The experiment sought to estimate the volume of the spheres using GI index, which will be explained later.

With respect to the number of electrodes, it is clear that the greater the number of electrodes the better the reconstructed EIT image accuracy, as is ratified in [199,218,219], so our study focuses on low spatial resolution EIT.

The temporal resolution is related to the number of frames that the EIT system has the ability to capture, which is closely linked to the hardware design and its processing capacity [199]. The temporal resolution of the designed EIT system obtains a frame every 16 sec.

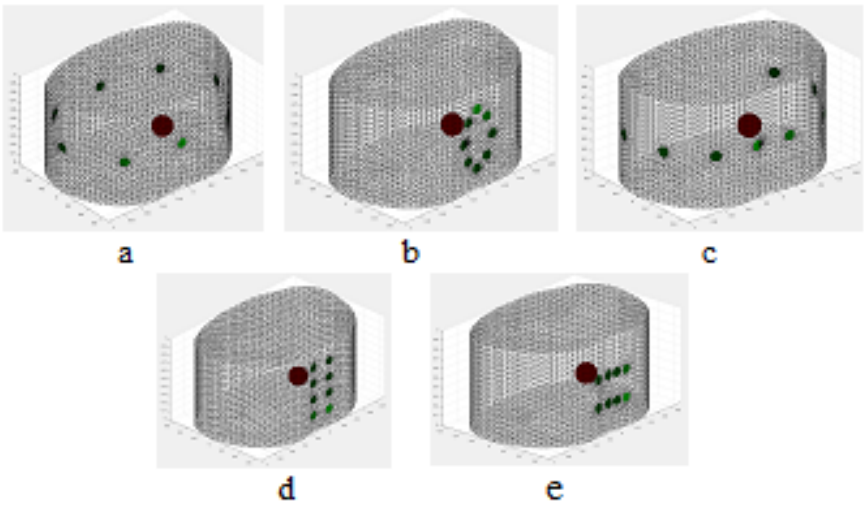

Figure 4.1: Electrode arrays. a) Ring, b) Coronet, c) Semicircular, d) 2 vertical lines and e) 2 horizontal lines.

4.3 Low-Cost EIT system design

The EIT system is based on the AFE4300 analog front-end of Texas Instruments, which was designed for body composition measurement. This integrated circuit has 8 ports for current injection and potential measurement. Although some of the ports are intended for calibration purposes, they can be configured as current-injection, voltage-detection system ports. The AFE4300 generates a 294.5 μA_{rms} alternating current through a voltage controlled current source (VCCS), which is powered by an internal direct digital synthesizer (DDS), which together a 6-bit DAC and 1-MSPS generates a sinusoidal signal. The potentials measured on the electrodes are obtained by a demodulator, which can be configured to obtain either the amplitude of the sinusoidal signal (FWR full-wave rectifier mode), or the I/Q components. In our experiments, we used the FWR mode which is faster than the other one. The obtained amplitude is quantized using a 16 bits delta-sigma ADC with a clock frequency of 1 MHz. A PIC16F886 microcontroller is the interface to configure the frequency of the injection signal, the configuration of the ports for injection and measurement and the transmission on the data to the computer are done through a HC06 Bluetooth module. An application in Labview is used to select the desired characteristics for the EIT system and to store the measured frames. In order to have a EIT system for in-vivo testing, it must have a current protection network for both, measurement and injection. This network is composed by resistors and capacitors that connect each port with the ground to eliminate the DC offset present in the current signals. The power is supplied by a 3.7V LiPO battery. The protection network, the current protection device of the AFE4300 and the battery power supply ensure compliance with the safety standard IEC60601 for medical equipment [45]. The Figure 4.2 shows the block diagram of the proposed EIT system and the Figure 4.3 shows the scheme of body composition meter module of the AFE4300.

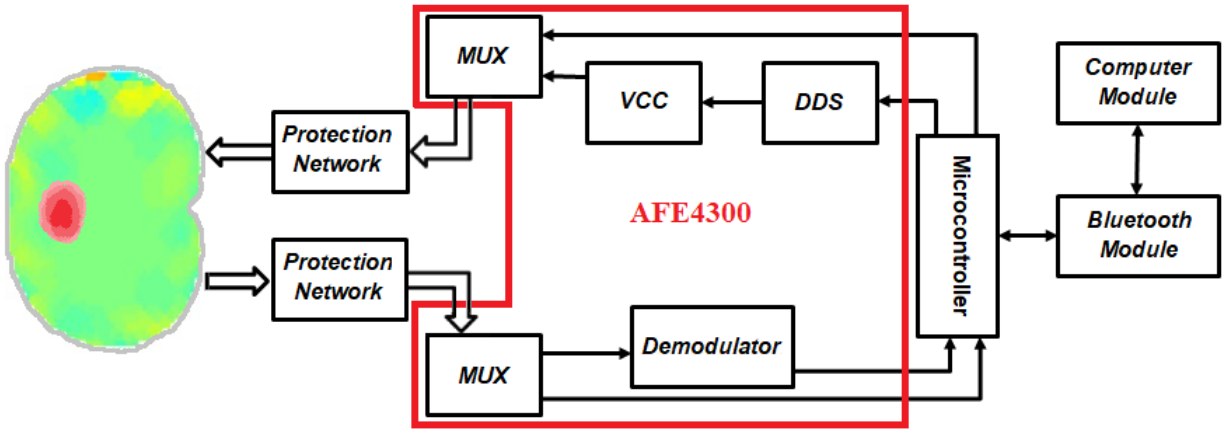

Figure 4.2: EIT system diagram.

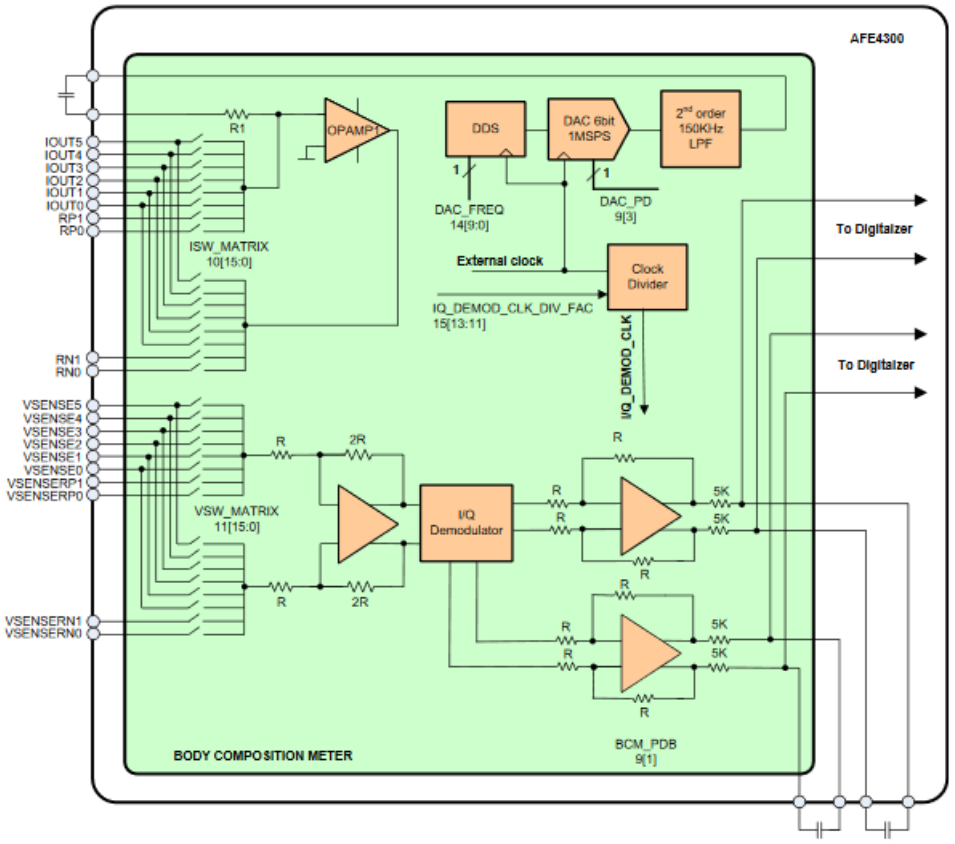

Figure 4.3: Module of body composition measurement of the AFE4300 [1].

4.3.1 AFE4300 configuration

The AFE4300 device can be configured through internal registers, which define the signal frequency, injection and measurement patterns, demodulation mode, and synchronization

of internal modules. Detailed information on the AFE4300 configuration is found in [1]. The Table 4.1 shows the configuration of the AFE4300 used for the operation of the tomograph designed.

Table 4.1: Registers configuration AFE4300.

Register	Address	Value	Description
ADC_CONTROL_REGISTER1	0X01	0X4140	Continuous-conversion or single-shot mode. Single-ended or differential mode. ADC power down. ADC dat-rate control bits.
MISC_REG1	0X02	0X0000	Write 0x0000 after power up and/or reset.
MISC_REG2	0X03	0XFFFF	Write 0XFFFF after power up and/or reset.
DEVICE_CONTROL	0X09	0X6006	Enable DAC for weight scale, body Composition measurements. Chip power down. Body composition measurement front-end power down. Weight scale front-end power down.
ISW_MUX	0X0A	Veering	Control for switches IOUTP, IOUTN,RP and RN
VSENSE_MUX	0X0B	Veering	Control for switches VSEBSEP, VSENSEN, VSENSEP_R and VSENSEN_R
IQ_MODE_ENABLE	0X0C	0X0000	Enable IQ demodulator.
WEIGTH_SCALE_CONTROL	0X0D	0X0000	Offset DAC setting for weight-scale front-end.
ADC_CONTROL_REGISTER2	0X10	0X0063	Reference and peripheral selection bits.
MISC_REG3	0X1A	0X0030	Write 0x0C00 after power up and/or reset.
BCM_DAC_FREQ	0X0E	0X0052	Set the frequency of BCM. excitation current source.
DEVICE_CONTROL2	0X0F	0X0800	IQ demodulator clock frequency.

The registers ISW_MUX and VSENSE_MUX are configured through the PIC 16F886 to select the electrodes for injection and measurement, respectively. The register BCM_DAC_FREQ defines the frequency of the current signal.

4.4 Injection and measurement patterns

4.4.1 Injection pattern for current signals

programmed from a 10-bit registerThe DDS output signal feeds a 6-bit DAC whose refresh rate is 1 msps. The high-frequency components of the DAC output signal are eliminated by means of a low pass band second-order filter with a cut-off frequency of 150 kHz. The DC component of the signal delivered by the filter is removed by means of a in-series external capacitor. One of the capacitor terminals is the input signal to a voltage-current converter that is connected to a multiplexer and then to the current injection ports IOUTX (Figure 4.3). The voltage to current conversion is made through the following equation:

$$i\left(t\right) = \left(\frac{V_{AC}}{R_1}\right) \tag{4.1}$$

Being $R_1 = 1.5\ \text{k}\Omega \pm 20\%$ an internal element of the AFE4300. Considering the minimal value of R_1, the maximal current generated is equal to the RMS value of the voltage $(1V_{pp}/(2\sqrt{2})$ divided by 1.2 kΩ, equivalent to 294.5 μA.

The injection patterns for the current signals are configured taking into account the ISW_MUX register (Figure 4.4), where each bit enables (1) or disables (0) the required

port. The bits corresponding to RN0, RN1, RP0 and RP1 are defined for the calibration of the device, for the design of EIT prototype these ports were enabled for current injection and to have an 8-port prototype. The ISW_MUX register frame manages the ports for the positive (bits 15 to 8) and negative (bits 7 to 0) outputs of VCCS.

15	14	13	12	11	10	9	8	7	6	5	4	3	2	1	0
IOUTP5	IOUTP4	IOUTP3	IOUTP2	IOUTP1	IOUTP0	RP1	RP0	IOUTN5	IOUTN4	IOUTN3	IOUTN2	IOUTN1	IOUTN0	RN1	RN0

Figure 4.4: Multiplexor control for current injection.

4.4.2 Measurement patterns for potentials

The measurements patterns for the potentials are configured taking into account the VSENSE_MUX register (Figure 4.5), where each bit enables (1) or disables (0) the required port. The calibration ports for measurement patterns are VESENSP_R0, VSENSEP_R1, VSENSEN_R0 and VSENSEN_R1. These ports are employed for measurement in the designed prototype to have 8 ports for measurement. The VSENSE_MUX register manages the ports for the positive (bits 15 to 8) and negative (bits 7 to 0) inputs of differential amplifier of the AFE4300.

15	14	13	12	11	10	9	8	7	6	5	4	3	2	1	0
VSENSEP5	VSENSEP4	VSENSEP3	VSENSEP2	VSENSEP1	VSENSEP0	VSENSEP_R1	VSENSEP_R0	VSENSEN5	VSENSEN4	VSENSEN3	VSENSEN2	VSENSEN1	VSENSEN0	VSENSEM_R1	VSENSEM_R0

Figure 4.5: Multiplexor control for potential measurement.

4.4.2.1 Current signal frequency definition

The signal frequency is defined for DAC output frequency (BCM_DAC_FREQ register), which is given by $DACxfCLK/1024$, where fCLK is the frequency of the device input clock. For medical applications the current signal frequency most used is 50 kHz, then DAC register was set to 0x0052; although the designed prototype allows the variation of this frequency.

4.4.3 Implementation EIT system

The EIT system has a microcontroller PIC 16F886, which configure the AFE4300 registers considering the values shown in Table 4.1, Both devices used 3.3 V for functioning. The

pins of PIC16F886 used for the communications with AFE4300 are the following:

- **Pins SDI and SDO**: Used to implement the transmission of data between the PIC and the AFE4300 using SPI.
- **Pin SCL**: Clock generated by the microcontroller in order to use SPI.
- **CLKOUT PIN**: Clock signal of 1 MHz generated by the PIC, for define the clock signal of AFE4300.
- **Pins RX and TX**: Used to transmit the data of the microcontroller to the Bluetooth module (HC-06) using the USART protocol.

4.4.3.1 Protection network

The safety stage consists of two capacitor-resistor networks. One of them in series with the current outputs and the other one with the voltage inputs to the AFE4300 (Figure 4.6). This in done to filter the DC components of the signals and to make EIT system compliant with the safety standard IEC60601 for medical equipment type III. On the other hand, a capacitor-resistor network in series with the electrode and ground port is employed to get better the measure accuracy, which is affected due the electrodes capacitance and human body [1].

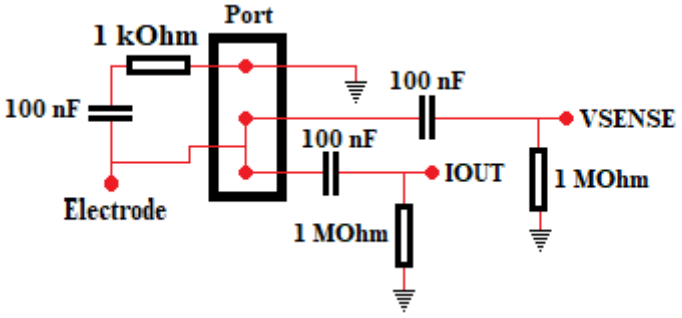

Figure 4.6: Protection network.

The designed system costs 65.60€. The prices of the devices AFE4300, PIC16F886 and HC06 respectively are 4.58€, 2.09€ and 11.61€; passive elements such as resistors and capacitors, in addition to electrode connectors, 2000 mA LiPo 3.7 V battery and Power Cell LiPo Charger, have a price of 47.32€.

4.4.3.2 Characterization of EIT system

The schematic diagram of EIT system is shown in Figure 4.7. The AFE4300, PIC16F866 and HC06 are contained in this circuit; also the PCB has ports to program the microcontroller and to connect a power supply.

The SNR and the number of frames per second that the device acquires were obtained using a 2D resistive network (Cardiff EIT phantom). A Labview application was implemented for data acquisition, which stored the potential measurements per frame.

The Table 4.2 shows the SNR for different measurement time delays. As it can be seen, for a time delay of 50 ms, the system exhibits the highest SNR, therefore the EIT system was configured to take measurements for 50 ms.

Table 4.2: SNR of EIT system for different measurement time delays.

Time delay	**SNR (dB)**		
(ms)	**Max**	**Mean**	**Min**
10	40.7	17.82	4.55
25	74.73	29.57	9.74
50	71.81	47.77	24.04
100	56.04	33.95	45.70

The time required to read a frame is calculated as the number of voltage measurements (64) multiplied by the total delay to measurement and transmission (250 ms), which equals to $64x250 = 16000$ ms, doing the proposed system suitable for application with low temporal variability. The frequency of the current signal was set up to 50 kHz, which is the most used in EIT for medical application.

4.5 Environments for experimentation

4.5.1 Saline phantom

A cylindrical vessel of 15 cm radius and 30 cm high was implemented for volume estimation tests. The saline phantom has a single ring arrangement of 8 electrodes and uses a saline solution with a concentration of 4 g/L. Steel spheres with volumes 0.028 m^3, 0.030 m^3 and 0.0314 m^3 were placed one by one into the phantom, and their volumes were estimated by GI. The best results for numerical simulation were obtained using the adjacent pattern for injection and measurement. The Figure 4.8 shows the experiment assembly.

4.5.2 Bladder phantom

A phantom that emulates the electrical properties of the lower pelvis was designed to estimate bladder volume through bioimpedance measurements. The conductivity of this part of the human body was estimated in 0.217 S/m, using the database of Hasgall and collaborators [195]. The conductivity of the urine takes values between 0.59 and 3.22 S/m [220, 221].

The first option we considered to emulate the electrical properties of the low pelvis was a mixture of graphite and silicone, based on the phantom proposed in [220, 221]. The Table 4.3 shows the conductivity of the mixture, measured with a Hewlett Packard 4192A Impedance Analyzer, when it contains 12 g of silicone and an amount of graphite ranging from 0.5 g to 12 g. The Table 4.3 shows the electrical behavior for a current signal of 20 to 100 kHz. The last row of Table 4.3 shows a strong positive correlation between conductivity and frequency, suggesting a capacitive behavior, which also exists in the bladder wall [195]. On the other hand, the conductivity values are very small compared to those of the lower pelvic tissue, and as a consequence, this mixture was discarded. The problem with this option is that for higher concentrations of graphite the mixture is not compact.

Table 4.3: Conductivity (S/m) of graphite and silicone samples.

Frequency	**Concentration of graphite (g)**				
(kHz)	**0.5**	**2**	**4**	**8**	**12**
20	4.2×10^{-6}	1.7×10^{-5}	1.4×10^{-5}	1.7×10^{-4}	1.5×10^{-3}
30	6.3×10^{-6}	1.8×10^{-5}	2.7×10^{-5}	2.4×10^{-4}	1.7×10^{-3}
40	8.3×10^{-6}	1.8×10^{-5}	4.0×10^{-5}	3.1×10^{-4}	1.9×10^{-3}
50	1.0×10^{-5}	1.9×10^{-5}	5.2×10^{-5}	3.7×10^{-4}	2.2×10^{-3}
60	1.2×10^{-5}	1.9×10^{-5}	7.0×10^{-5}	4.3×10^{-4}	2.4×10^{-3}
70	1.4×10^{-5}	2.0×10^{-5}	8.5×10^{-5}	4.9×10^{-4}	2.8×10^{-3}
80	1.6×10^{-5}	2.1×10^{-5}	9.8×10^{-5}	5.5×10^{-4}	2.9×10^{-3}
90	1.8×10^{-5}	2.3×10^{-5}	11.0×10^{-5}	6.1×10^{-4}	3.1×10^{-3}
100	2.1×10^{-5}	2.5×10^{-5}	12.3×10^{-5}	6.7×10^{-4}	3.3×10^{-3}
Pearson's correlation	0.9984	0.9487	0.9991	0.9996	0.9959

The second option was to use agar and saline solution. The mixture contained 1 liter of saline solution with a conductivity of 0.193 S/m, and 20 g of biological agar No, 1 of Oxoid. The overall conductivity of the phantom was set to 0.217 S/m, emulating the electrical characteristics of the lower human pelvis.

The bladder phantom was implemented in a 30 cm long, 30 cm wide and 30 cm high methacrylate cubic container. For this work three phantoms were implemented, each one with cylindrical cavity of radius 5.2 cm, 4.15 cm and 2.5 cm. All of the cavities were 1.9 cm deep. These cavities were used to emulate bladders of different sizes (Figure 4.9). Every bladder phantom has a layer of a mixture of agar and saline solution of 2 cm of high, to emulate the lower pelvis tissue. The 8 electrodes of the EIT system were located on the underside of the container according to the pattern shown in Figure 4.10. The assembly of bladder phantom is shown in Figure 4.11.

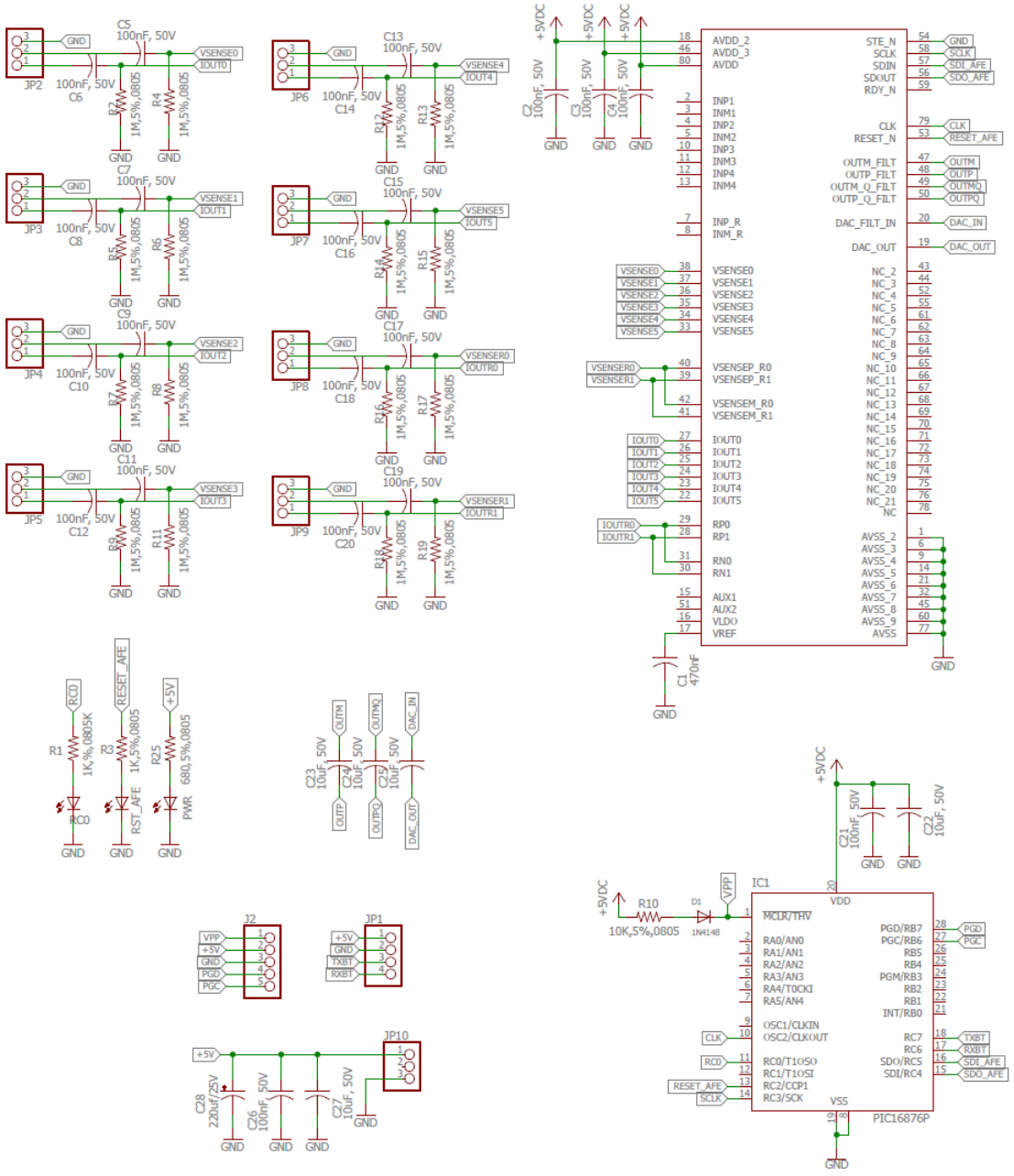

Figure 4.7: Schematic diagram of EIT system.

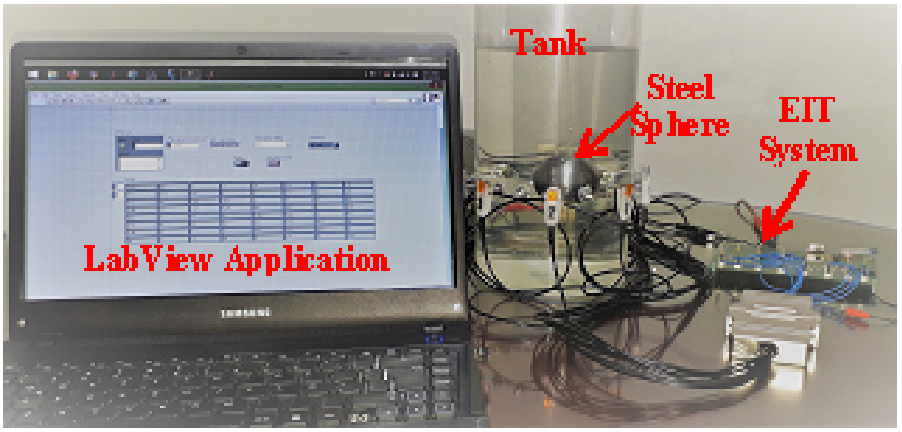

Figure 4.8: Assembly of saline phantom.

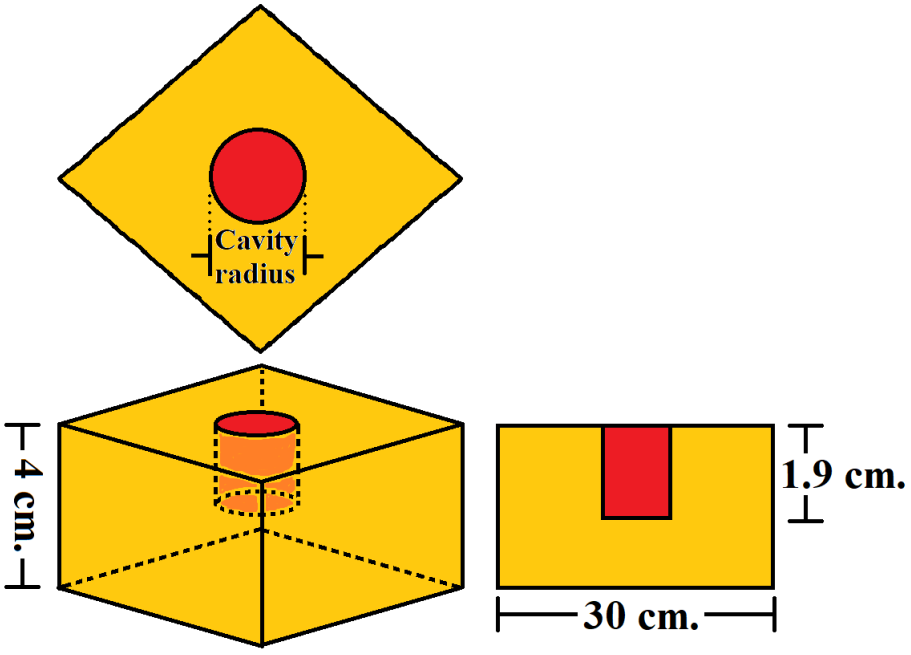

Figure 4.9: Bladder phantom implemented with an agar and saline solution.

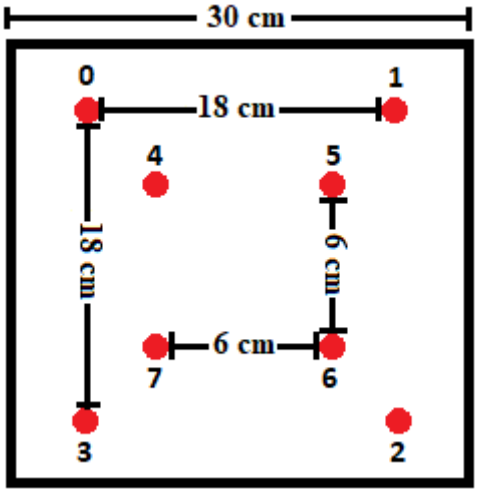

Figure 4.10: Electrodes configuration of the bladder phantom.

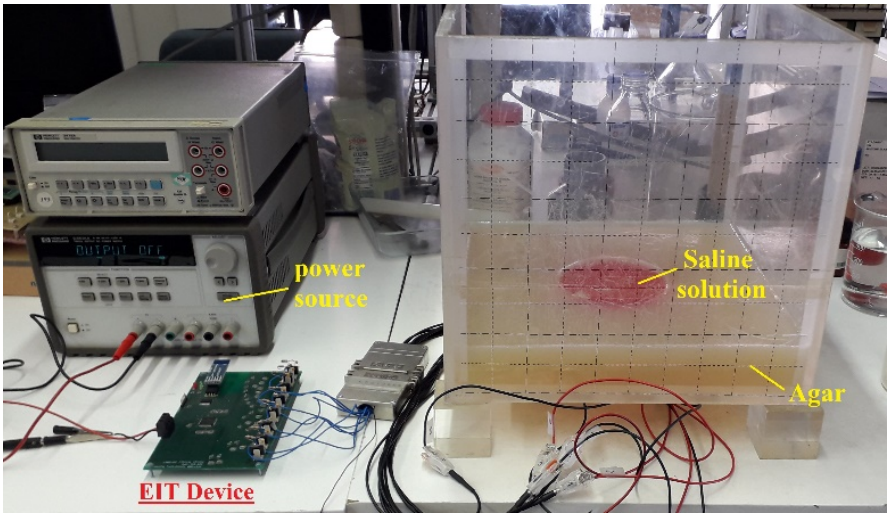

Figure 4.11: Assembly of the bladder phantom.

5 Results

5.1 Introduction

This chapter presents numerical and experimental results regarding: (i) the performance of different previously proposed algorithms for solving the forward and inverse EIT problems, (ii) the effect of the electrode arrangement and injection and measurement patterns on EIT volume estimation, iii) the in-vitro experiments to compare GI with the bioimpedance approaches IRM, VCR and MVCR, with respect to their capacity to differentiate between three steel spheres of different size, and (iv) the in-vitro experiments to compare GI with FIM approaches, regarding their robustness against conductivity uncertainty.

The absolute and relative errors of the potentials estimated on the electrodes were the criteria to select the best algorithm for solving the forward problem. For the inverse problem, these criteria were the Pearson's correlation coefficient and percentage of error. The comparison between algorithms was performed using two Matlab-EIDORS interfaces developed as part of this thesis.

The effect of the electrode spatial distribution on EIT volume estimation was assessed using the arrangements: RN, SC, CN, V2L, and H2L; and for the effect of the injection and measurement patterns, the adjacent and opposite configurations were studied. Once the best combination of arrangement and patterns was obtained through numerical simulation, it was employed in the later experiments with a physical phantom.

To compare GI, IRM, VCR, and MVCR, we conceived an experiment involving a small, medium and large steel spheres that were placed, one at a time, in a tank with a saline solution. For each sphere we took 30 voltage measurements, with a sampling time of 16 seconds. The three data sets, one for each sphere, were used as the inputs for the bioimpedance methods (FIM or IRM or VCR or MVCR). The medians of the three resulting output datasets were compared using the Kruskal-Wallis test to assess the significance of their differences.

To compare GI with FIM approaches, we used three objects of different volume as in the

experiments of the previous paragraph; but this time, the internal conductivity of each object was changed to assess robustness against conductivity uncertainty.

5.2 Performance of EIT image reconstruction algorithms

This phase of the study included the forward and inverse problem solvers available in EIDORS. Once the best solver for the forward problem was selected, it was used in all subsequent comparisons between inverse problem solvers.

5.2.1 Selection of the solver for the forward problem

The graphical user interface for the forward problem (GUI-Forward), presented in Figure 5.1, has the following functionalities: i) generation of 2D and 3D models, ii) selection of first or higher order solvers, iii) graphical display of currents and potentials within a FEM model, and iv) calculation of the absolute and relative errors between the potentials estimated by EIDORS and those measured on a real EIT system.

The algorithms to solve the forward problem were evaluated by comparing the potentials measured on a physical cylindrical phantom of 15 cm in diameter and 40 cm height, with the potentials predicted using a FEM model consisting of 2304 elements and 80 planes. For both, the real and simulated cylinder, we used 8 electrodes distributed in ring arrangement. The reference potentials were obtained when the tank was filled with a saline solution whose conductivity was 0.12 S/m. Subsequently, copper and a plastic bars, with 3.5 and 2.5 cm of diameter, respectively, were placed in the saline tank. The Figure 5.2 shows the real and virtual tanks with the two bars inside. The conductivity distribution estimation of the tank with the bars is presented in [222].

The Table 5.1 shows that there is no difference between the errors given by the first and higher orders solvers. However, the higher order algorithm requires less computing time than the first order. For this reason, the higher order algorithm will be used to solve forward problems, considering FEM and CEM approaches available in EIDORS.

5.2.2 Selection of the solver for the inverse problem

The Figure 5.3 presents the graphical user interface for the inverse problem (GUI-Inverse). It has the following functionalities: i) selection of 2D and 3D models generated with GUI-Forward, ii) offline operation using real or simulated data, iii) graphical display of the mesh with the reconstructed image, and iv) calculation of CC and PE.

The first step in EIT image reconstruction is to use either FEM or CEM models to estimate the potential on the electrodes. FEM is the most widely used method in EIT [138], whereas CEM has a low computational cost [145]. The estimated and the measured

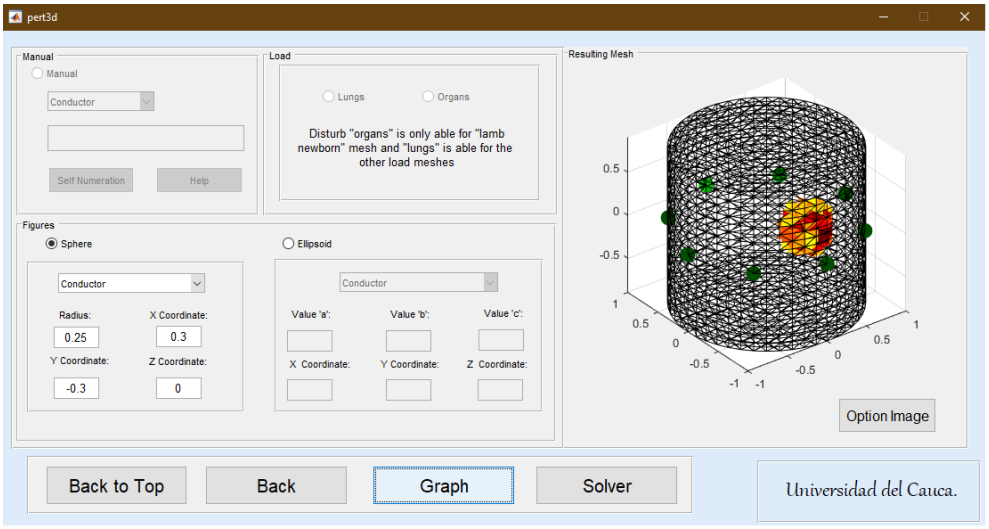

(a)

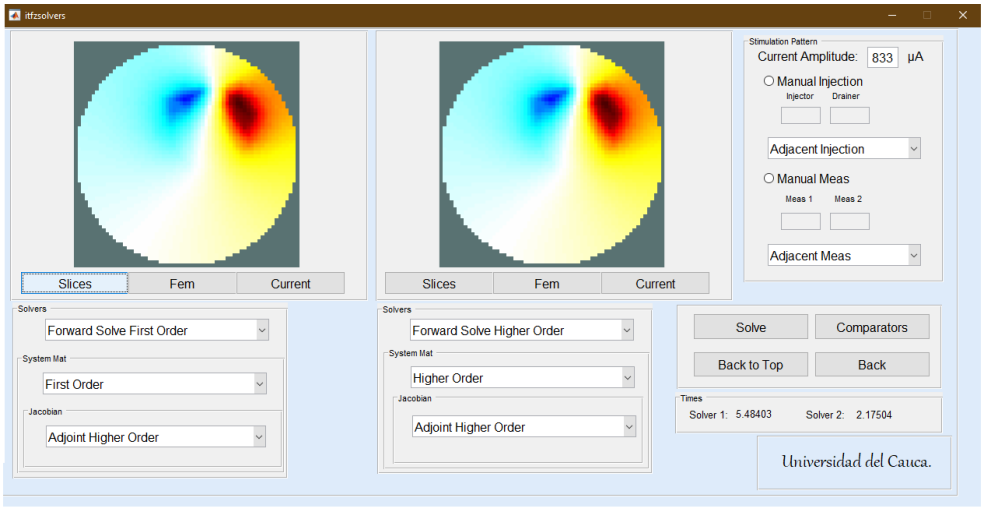

(b)

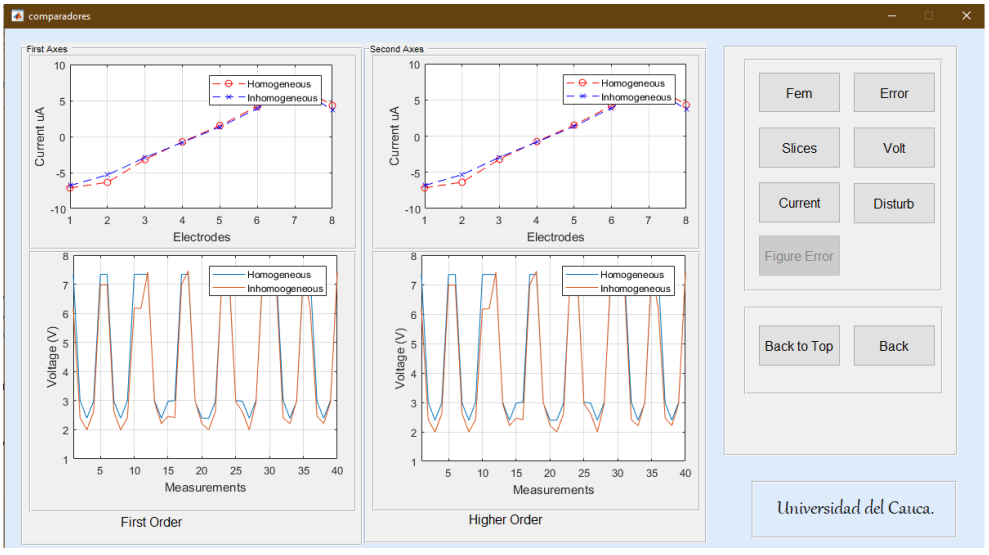

(c)

Figure 5.1: Developed GUI for forward problem: a) Forward model construction, b) Selection of forward problem solvers, c) Results of solving forward problem.

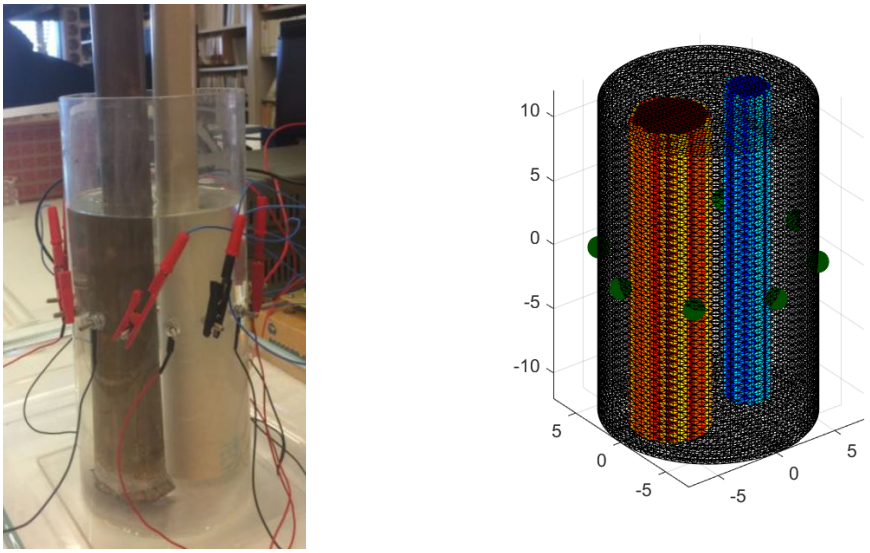

(a) Phantom (b) FEM model

Figure 5.2: Phantom tank and FEM model of phantom for potential estimation.

Table 5.1: Comparison between potentials measured and estimated, and estimation time of potentials on forward model.

SOLVER	RE (%)	AE (%)	Time (s)
Tank without bars			
First Order	1.44	3.95	5.26
Higher Order	1.44	3.95	5.11
Tank with conductive bar			
First Order	1.86	6.93	1.85
Higher Order	1.86	6.93	1.76
Tank with non-conductive bar			
First Order	1.90	11.56	1.36
Higher Order	1.90	11.56	1.27
Tank with conductive and non-conductive bars			
First Order	1.20	2.47	2.54
Higher Order	1.20	2.47	2.47

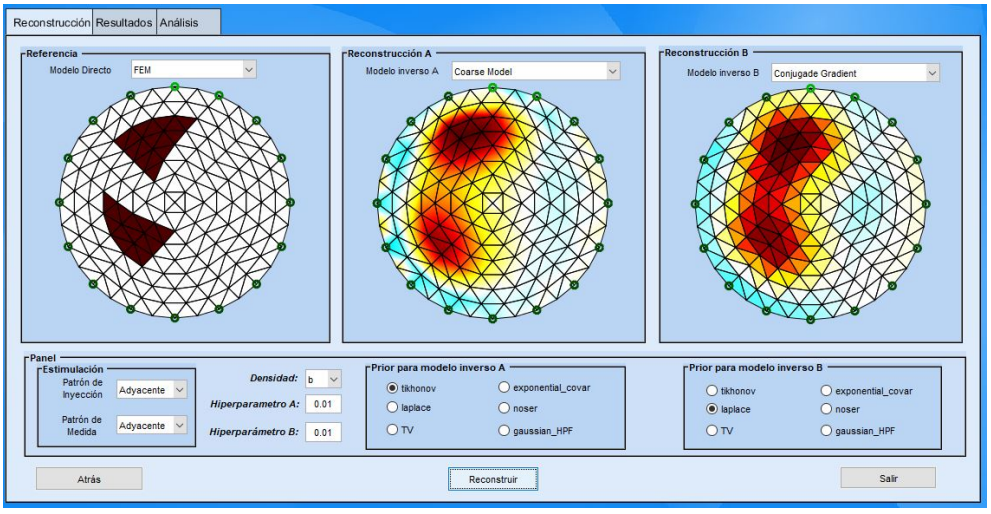

(a)

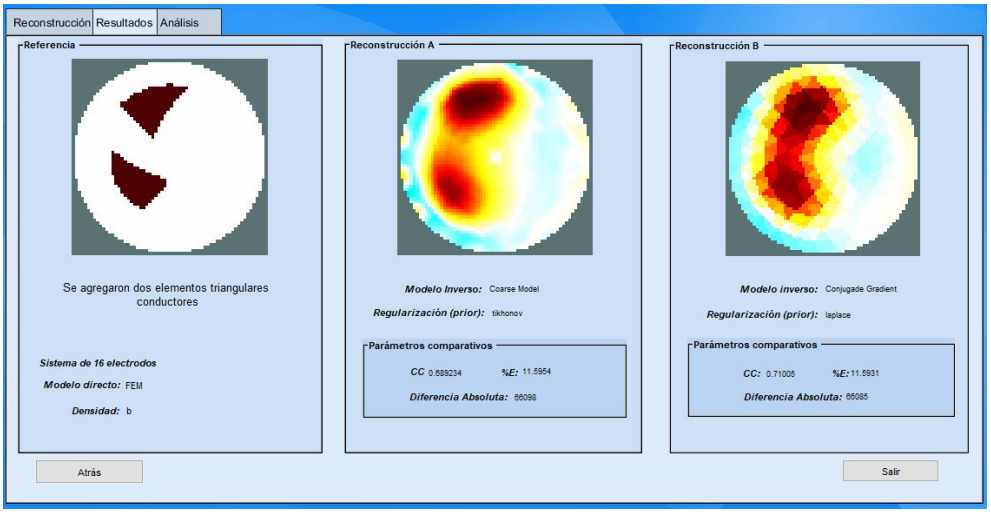

(b)

Figure 5.3: Developed GUI for inverse problem: a) Selection of algorithms and parameters for image reconstruction, b) Reconstructed image and comparative results.

potentials are the inputs to the reconstruction algorithms, which require regularization processes to find unique and stable solutions. EIDORS has the following reconstruction algorithms: Gauss-Newton One Step (GN-OS), Gauss-Newton (GN), Primal-Dual Interior Point Method-Difference (PDIMP-D), and Kalman; and the following options for regularization: Tikhonov, Laplace, Total Variation, Exponential Covar, Noser, and Gaussian High Pass Filter. The accuracy of the different combinations between reconstruction and regularization algorithms was determined using the CC and PE, which are described by the Equations (3.24) and (3.25), respectively.

A circular 2D model with 8 electrodes and a mesh density of 256 elements was used to compare inverse problem solvers. The adjacent injection and measurement patterns were employed for this test, although the opposite and trigonometric patterns are also available. In addition, only differential reconstruction algorithms were considered. The Table 5.2 shows the results obtained with the configurations that presented a CC greater than 0.5. The triplets ⟨FEM, Noser, GN-OS⟩, ⟨FEM, Noser, GN⟩ and ⟨FEM, Noser, PDIMP-D⟩ have the best CC and PE; being, all of them being good alternatives for image reconstruction. For the subsequent in-vitro experiments, we selected ⟨FEM, Noser, GN-OS⟩ which had a slightly better performance that ⟨FEM, Noser, GN⟩ and ⟨FEM, Noser, PDIMP-D⟩.

Table 5.2: Quantitative results of reconstruction of EIT images.

Regularization	Solver forward problem	CG		GN-OS		GN		PDIMP-D		Kalman	
		CC	PE (%)	CC	PE (%)	CC	PE (%)	CC	PE (%)	CC	PE(%)
Tikhonov	**FEM**	0.70	11.08	0.70	11.08	0.70	11.97	0.70	11.97	0.73	10.89
Laplace	**FEM**	0.71	11.59	0.70	11.84	0.70	13.14	0.68	12.49	0.55	11.67
Total Variation	**FEM**	0.86	7.07	0.85	7.03	0.86	7.15	0.86	7.15	0.70	11.92
Exponential Covar	**FEM**	0.80	8.57	0.77	9.73	0.77	10.39	0.75	10.47	0.66	11.48
Noser	**FEM**	0.85	7.35	0.86	6.58	0.85	6.63	0.86	6.63	0.70	11.97
Gaussian High Pass Filter	**FEM**	0.83	7.55	0.78	9.19	0.78	9.68	0.78	9.69	0.69	11.68
Tikhonov	**CEM**	0.65	13.17	0.65	13.17	0.64	14.75	0.65	14.75	0.68	13.53
Laplace	**CEM**	0.68	12.5	0.66	13.43	0.67	15.23	0.64	14.45	0.49	13.78
Total Variation	**CEM**	0.84	7.78	0.84	8.01	0.83	8.36	0.83	8.36	0.65	14.72
Exponential Covar	**CEM**	0.77	9.62	0.72	11.31	0.73	12.44	0.71	12.50	0.60	14.16
Noser	**CEM**	0.83	7.94	0.86	6.74	0.86	6.82	0.86	6.82	0.65	14.78
Gaussian High Pass Filter	**CEM**	0.80	8.59	0.73	10.85	0.74	11.79	0.74	11.58	0.64	14.61

5.3 Effect of electrode arrangements and patterns of injection and measurement of signals of EIT in the volume's estimation

The effect of the electrode arrangements and patterns of injection and measurement focused on volume estimation. The simulation experiments for this analysis used a FEM model of the bladder and lower pelvis. The electrode arrangement is detailed in Section 4.2. To estimate the volume of the bladder using GI, we applied the GN-OS reconstruction algorithm with Noser regularization, because, according to the Table 5.2, they presented the best performance. The Figures 5.4 to 5.8 present the volume estimation of the simulated bladder, using the GI method with different electrode arrays and injection and measurement patterns. The dotted red line represents the theoretical volume of the simulated bladder as a function of its radius. According to these Figures, the ring configuration with adjacent patterns for injection and measurement (RN ad-ad) presents the best approximation to the theoretical volume (Figure 5.7), followed by the semicircular arrangement with injection and measurement in opposition (SC op-op) (Figure 5.8). The disposition consisting of 2 vertical lines with adjacent injection and measurement patterns (V2L ad-ad) presents an acceptable volume estimation (Figure 5.6). It is also evident that the incremental behavior of $|GI^{-1}|$ is directly related with the volume of the simulated bladder. The AE was calculated by normalizing both, the estimated and the theoretical volume, to avoid the calculation of a scaling factor relating $|GI^{-1}|$ and m^3.

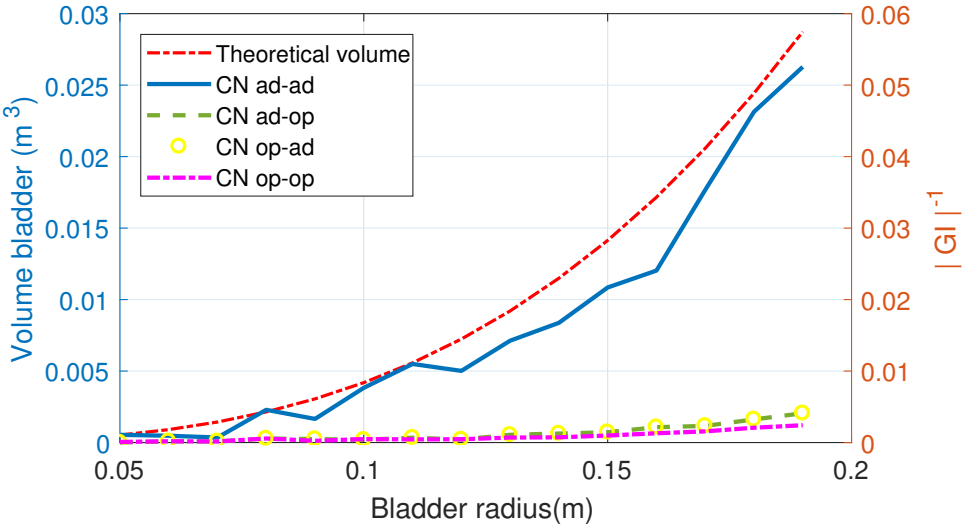

Figure 5.4: Estimated bladder volume with the coronet array (CN) and combinations of adjacent (ad) and opposite (op) patterns.

The Table 5.3 shows the medians and interquartile ranges of AE considering simulated signals free of noise. The RN ad-ad and SC op-op configurations have the lowest medians (1.66×10^{-2} and 7.23×10^{-2}, respectively). The interquartile ranges of these configura-

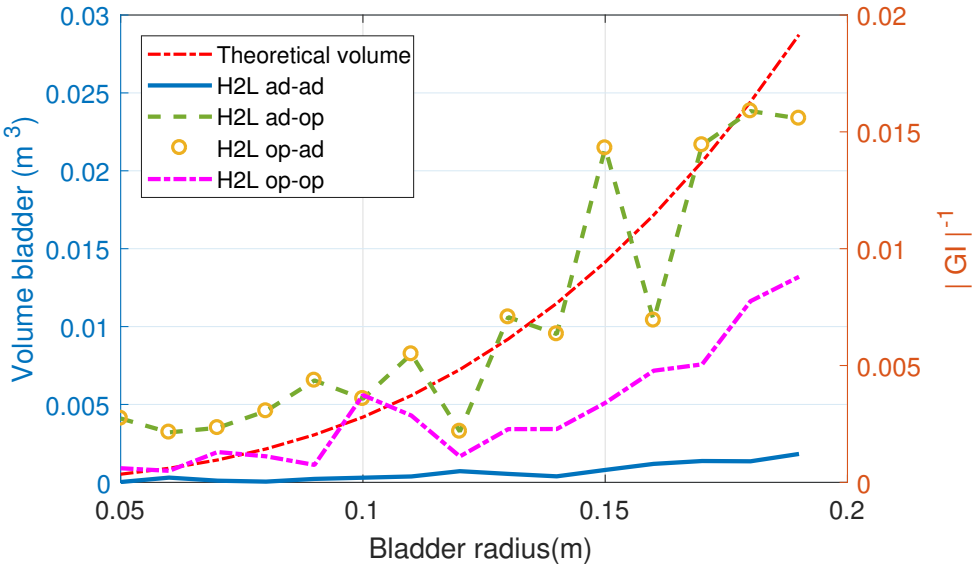

Figure 5.5: Estimated bladder volume with 2 horizontal lines of electrodes (H2L) and combinations of adjacent (ad) and opposite (op) patterns.

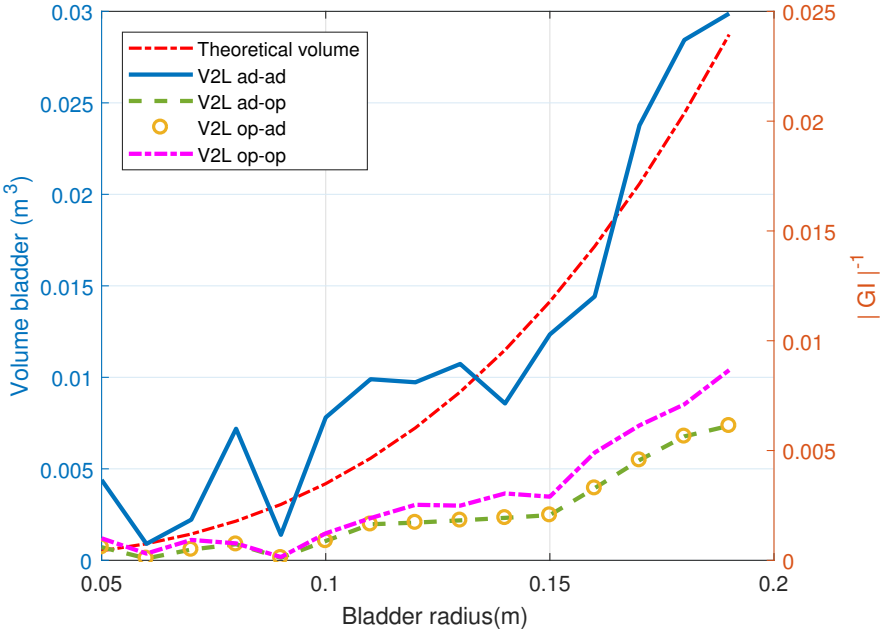

Figure 5.6: Estimated bladder volume with 2 vertical lines of electrodes (V2L) and combinations of adjacent (ad) and opposite (op) patterns.

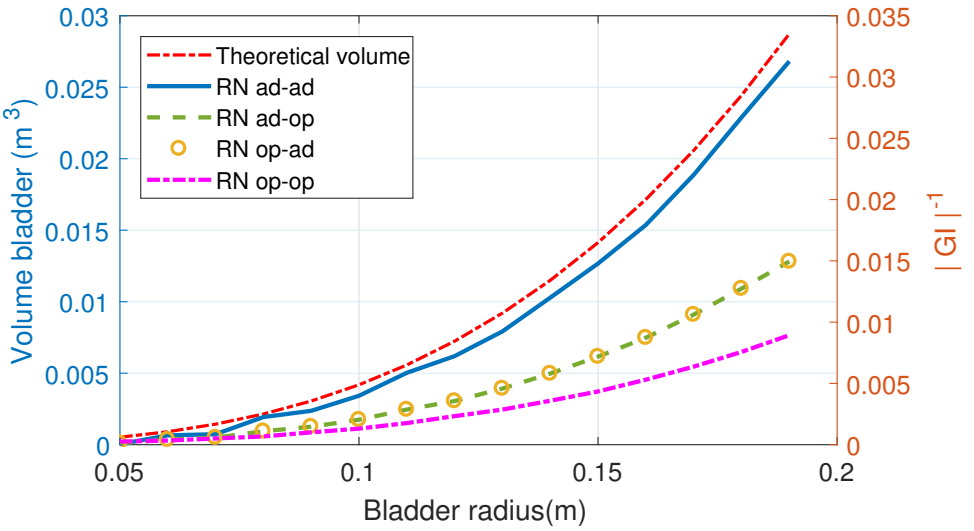

Figure 5.7: Estimated bladder volume with the ring array (RN) and combinations of adjacent (ad) and opposite (op) patterns.

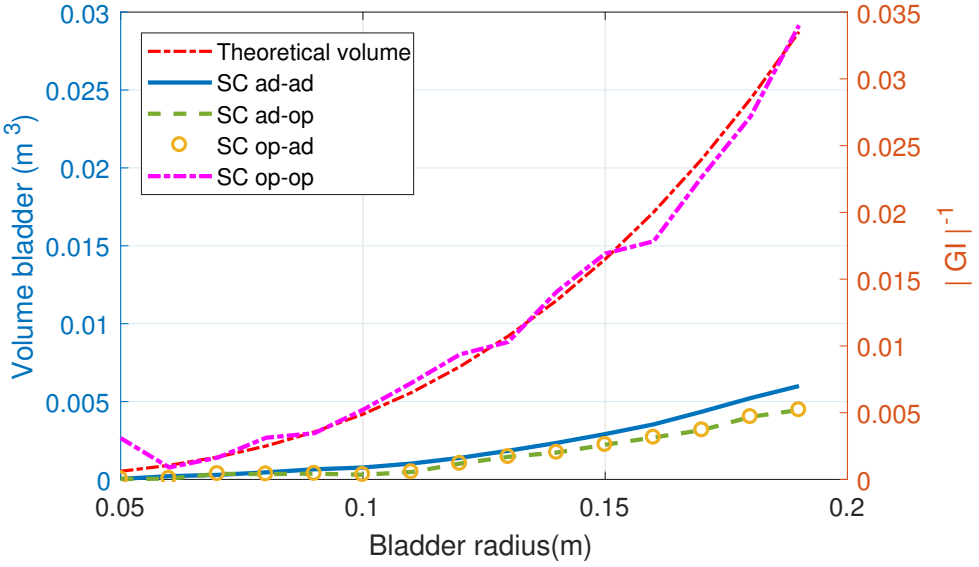

Figure 5.8: Estimated bladder volume with the semicircular array (SC) and combinations of adjacent (ad) and opposite (op) patterns.

Table 5.3: Median and intercuartile range of the absolute error for noise free measurements.

	Injection-Measurement							
	ad-ad		ad-op		op-ad		op-op	
	Median	Interquatile range	Median	Interquatile range	Median	Interquatile range	Median	Interquatile range
CN	22.51×10^{-2}	32.20×10^{-2}	23.68×10^{-2}	46.69×10^{-2}	23.68×10^{-2}	46.69×10^{-2}	23.48×10^{-2}	49.94×10^{-2}
H2L	23.49×10^{-2}	49.58×10^{-2}	17.33×10^{-2}	27.65×10^{-2}	17.33×10^{-2}	27.65×10^{-2}	22.70×10^{-2}	51.67×10^{-2}
RN	1.66×10^{-2}	2.75×10^{-2}	12.53×10^{-2}	25.39×10^{-2}	12.53×10^{-2}	25.39×10^{-2}	16.99×10^{-2}	35.96×10^{-2}
SC	19.31×10^{-2}	39.47×10^{-2}	21.03×10^{-2}	42.62×10^{-2}	21.30×10^{-2}	42.62×10^{-2}	7.23×10^{-2}	7.02×10^{-2}
V2L	10.72×10^{-2}	12.01×10^{-2}	19.00×10^{-2}	42.86×10^{-2}	19.00×10^{-2}	42.86×10^{-2}	16.17×10^{-2}	37.57×10^{-2}

Table 5.4: Median and intercuartile range of the absolute error for measurement with Gaussian white noise.

	Injection-Measurement							
	ad-ad		ad-op		op-ad		op-op	
	Median	Interquatile range	Median	Interquatile range	Median	Interquatile range	Median	Interquatile range
CN	17.73×10^{-2}	22.16×10^{-2}	22.66×10^{-2}	44.15×10^{-2}	23.78×10^{-2}	44.92×10^{-2}	24.13×10^{-2}	49.88×10^{-2}
H2L	23.72×10^{-2}	48.15×10^{-2}	11.03×10^{-2}	29.84×10^{-2}	13.02×10^{-2}	22.17×10^{-2}	23.09×10^{-2}	51.00×10^{-2}
RN	5.90×10^{-2}	2.89×10^{-2}	12.44×10^{-2}	23.20×10^{-2}	12.69×10^{-2}	23.23×10^{-2}	18.32×10^{-2}	34.57×10^{-2}
SC	18.45×10^{-2}	39.73×10^{-2}	22.32×10^{-2}	45.74×10^{-2}	19.91×10^{-2}	43.38×10^{-2}	6.46×10^{-2}	6.85×10^{-2}
V2L	11.95×10^{-2}	14.57×10^{-2}	16.41×10^{-2}	44.05×10^{-2}	18.92×10^{-2}	42.68×10^{-2}	15.86×10^{-2}	37.07×10^{-2}

tions are also the smallest, being both the best alternatives for volume estimation.

EIT systems are affected by two main sources of noise. One coming from the contact impedance between the electrodes and skin, and the other generated by electrical noise. The effects of noise on volume estimation accuracy are presented in the Table 5.4. For this test, the SNR was set to 47.7 dB, which is the value measured for the system presented in [222]. The RN ad-ad and SC op-op configurations presented the lowest median AE values (5.90×10^{-2} and 6.46×10^{-2} respectively). The interquartile ranges of these alternatives are also the smallest.

The root-mean-square-error (RMSE) was calculated for each configuration. The Table 5.5 indicates that the configurations with the lowest RMSE are RN ad-ad and SN op-op.

Table 5.5: Root-mean-square of the volume estimation error, considering free-noise measurements and with Gaussian white noise (SNR 47.7 dB).

	Free noise measures				measures with Gaussian noise			
	Injection-measurements pattern				Injection-measurement pattern			
	ad-ad	ad-op	op-ad	op-op	ad-ad	ad-op	op-ad	op-op
CN	37.8%	40.5%	40.5%	42.6%	51.5%	40.4%	40.9%	42.4%
H2L	44.5%	26.1%	26.1%	34.6%	44.6%	27.1%	28.9%	35.1%
RN	3.7%	22.3%	22.3%	31.9%	6.9%	23.5%	23.8%	32.2%
SC	35%	38%	38%	8.8%	35.1%	36.6%	38.3%	8.9%
V2L	9.7%	36.6%	36.6%	32.9%	13.3%	36.3%	36.8%	32.9%

5.4 In-vitro experiments for volume estimation

The performance of GI, IRM, and VCR was evaluated using a cylindrical phantom filled with a saline solution (4 g/L) and three steel spheres of radius of 27.5, 35.0 and 37.5 mm. For each trial, only one sphere was placed in the tank. The Kruskal-Wallis test was employed to determine whether the differences between measurements were significant. For the in-vitro experiments, we selected the ring arrangement and the adjacent patterns for both, injection and measurement. This was because they presented the best performance during the numerical simulation tests.

The Figures 5.9 to 5.12 show the box plot considering 30 measurements for each sphere. The dispersion of the data was caused by the measurement noise. [46] shows that GI is inversely proportional to the volume of the object. Hence, the Figure 5.9 presents the results for $|GI|^{-1}$ instead of GI. This index allows a good differentiation of the size of each sphere.

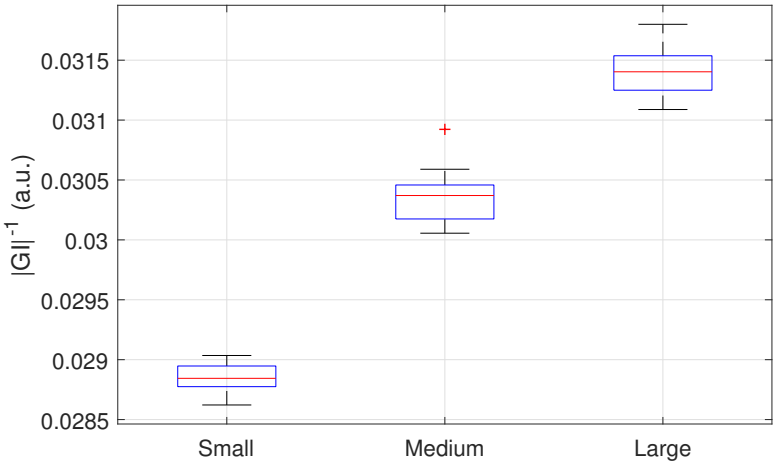

Figure 5.9: GI results for volume variation.

The Figure 5.10 shows that IRM [133] medians do not increase as the volume of the spheres increases. Furthermore, the Table 5.6 suggests that these variables are nonlinearly related. The results for VCR and MVCR are presented in Figures 5.11 and 5.12 respectively. Interquartile ranges indicate that MVCR is much less sensitive to noise than VCR. On the other hand, the medians of Figure 5.12 only differ by the second decimal digit, indicating that MVCR is also less sensitive to changes in volume.

For each of the four indices compared in this study, medians and interquartile ranges are presented in Tables 5.6 and 5.7. The values were obtained by taking 30 measurements for each sphere.

The GI, VCR and MVCR increase as the volume of the spheres increases (Table. 5.6). The interquartile ranges of these indices (Table 5.7) show that it is feasible to discriminate

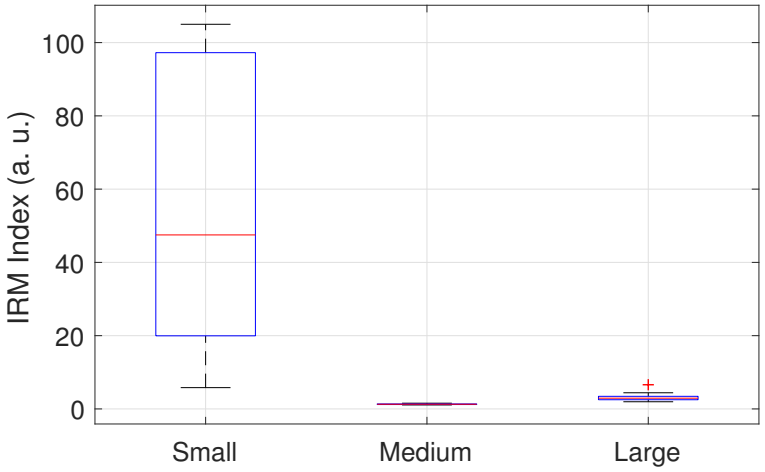

Figure 5.10: IRM results for volume variation.

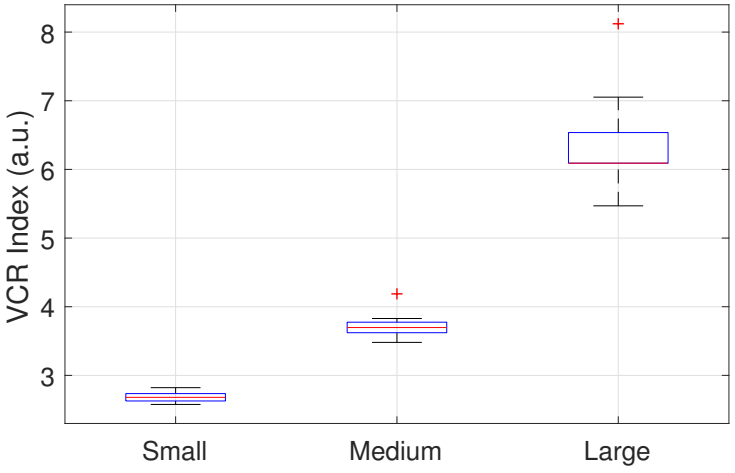

Figure 5.11: VCR results for volume variation.

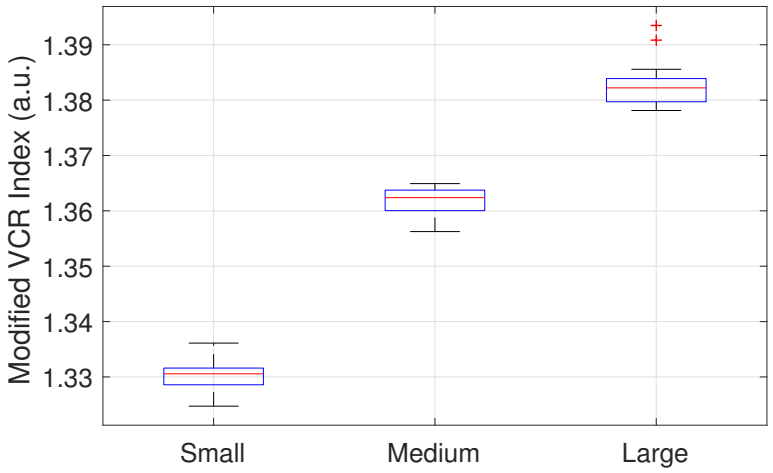

Figure 5.12: MVCR results for volume variation.

Table 5.6: Medians of measurements for each volume estimation method and sphere size.

	GI	IRM	VCR	MVCR
Small	2.88×10^{-2}	47	2.68	1.33
Medium	3.03×10^{-2}	1.12	3.69	1.36
Large	3.14×10^{-2}	2.91	6.09	1.38

Table 5.7: Interquartile ranges of measurements for each volume estimation method and sphere size.

	GI	IRM	VCR	MVCR
Small	1.7×10^{-4}	76	0.09	3×10^{-3}
Medium	3.04×10^{-4}	0.17	0.18	3.5×10^{-3}
Large	3.5×10^{-4}	0.95	0.21	4.2×10^{-3}

between the volumes of the spheres, since there is no overlap between the data sets.

The Figure 5.13 show that the region center of GI approach has a very low sensitive, near to zero (represented by white color); on the other hand, the IRM, VCR and MVCR approaches show a negative sensitive (blue hue). Considering the sensitivity maps, these indices could have a best performance if the object under study is placed near of the electrodes; where the sensitive is high (dark red color).

The p-values from Kruskal-Wallis test for differences between the medians of the output variables for each index are shown in Table 5.8. Differences between output variables were considered insignificant when $p > 0.05$, which indicates the impossibility of distinguishing between volumes. If p-values from Kruskal-Wallis test are $p \leq 0.05$, then volumes are distinguishable.

For the four methods, the Kruskal-Wallis test indicates that the differences between the measurements obtained with each sphere are significant. However, as presented in Ta-

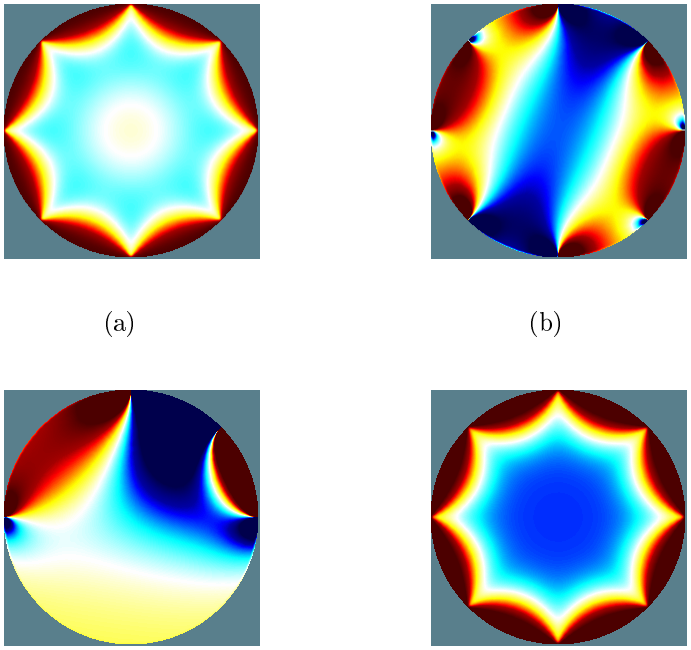

(a) (b)

(c) (d)

Figure 5.13: Sensitivity maps for ring electrodes arrangement: a) GI, b) IRM, c) VCR, d) MVCR.

Table 5.8: p-values from Kruskal-Wallis test between for each index and sphere size.

	GI	**IRM**	**VCR**	**MVCR**
Small-Medium	1.34×10^{-8}	2.26×10^{-7}	1.24×10^{-8}	1.32×10^{-8}
Medium-Large	1.34×10^{-8}	2.26×10^{-7}	1.11×10^{-8}	1.32×10^{-8}
Small-Large	1.34×10^{-8}	1.04×10^{-7}	1.10×10^{-8}	1.33×10^{-8}

ble 5.6 there is no direct or inverse relationship between IRM medians and the volume of the spheres.

5.5 In-vitro experiments to assess robustness against urine conductivity uncertainty.

The estimation of bladder volume should consider that the conductivity of urine varies with diet and pathogens of the urinary system. This implies that the estimation indices must be robust against urine conductivity uncertainty. In this section, we study the effect of the conductivity on the volume estimation.

The GI has been used in bladder monitoring experiments [5, 132, 133], in which the participants begin with empty bladder and then drink a liquid of known conductivity. However,

in practice, urine conductivity is known and greatly affect GI values.

The IRM index is defined by [133] as:

$$IRM = \frac{Z_s - Z_f}{Z_b - Z_f} \tag{5.1}$$

Where the impedance Z_f, Z_b and Z_s are defined as $Z_f \triangleq U_f/I_f$, $Z_b \triangleq U_b/I_b$ and $Z_s \triangleq U_s/I_s$, and will be represented as the sum of a constant value more the measurement noise:

$$\begin{aligned} Z_f &= \bar{Z}_f + \epsilon_f \\ Z_b &= \bar{Z}_b + \epsilon_b \\ Z_s &= \bar{Z}_s + \epsilon_s \end{aligned} \tag{5.2}$$

Then it's get:

$$IRM = \frac{(\bar{Z}_s - \bar{Z}_f) + (\epsilon_s - \epsilon_f)}{(\bar{Z}_b - \bar{Z}_f) + (\epsilon_b - \epsilon_f)} \tag{5.3}$$

When the object under study is at the center of the electrode arrangement of Figure 3.5, then $U_f = U_b = U_s$, and as consequence, $\bar{Z}_f = \bar{Z}_b = \bar{Z}_s$. The Figure 5.14 shows Uf, U_b and U_s for system of two concentric disks presented in Section 3.2.1. When the three impedances are equal, the resulting IRM will depend on the measurement noises but not on the conductivity or the size of the object analyzed (Equation 5.4):

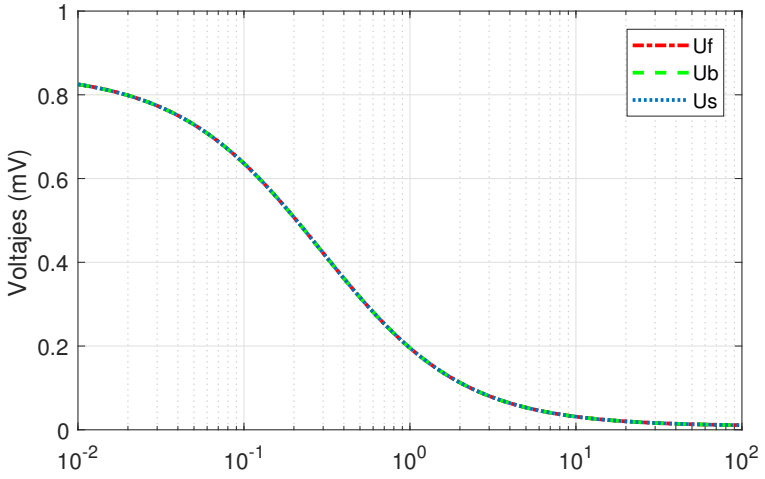

Figure 5.14: Potential on electrodes calculated using the example of Section 3.2.1.

$$IRM = \frac{\epsilon_s - \epsilon_f}{\epsilon_b - \epsilon_f} \tag{5.4}$$

The analytical solution of the Laplace's equation for two concentric disks of different conductivity (Section 3.2.1) was used to assess the robustness of VCR and MVCR against conductivity uncertainty. The Figures 5.15 and 5.16 show that VCR and MVCR depend on the conductivity of the inner circle.

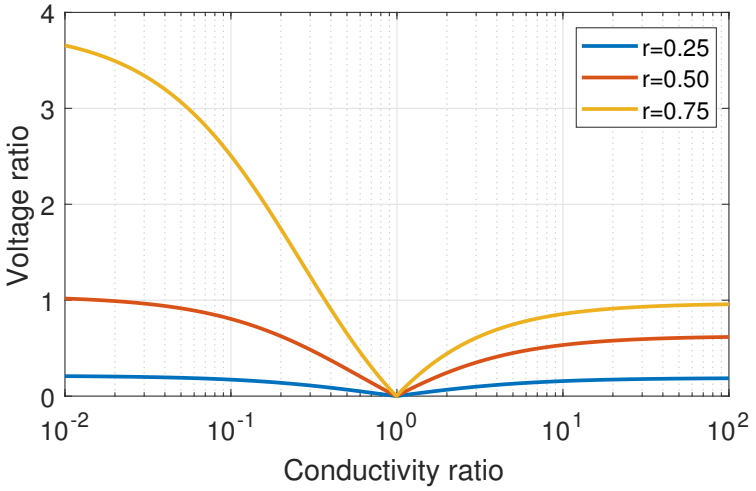

Figure 5.15: Voltage ratio vs conductivity ratio.

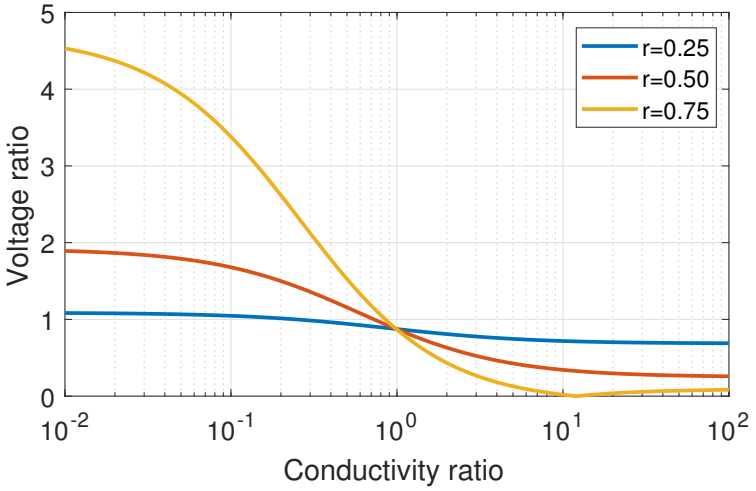

Figure 5.16: Modified voltage ratio vs conductivity ratio.

As GI, IRM, VCR and MVCR are not robust against conductivity uncertainty, they were not considered for the bladder phantom tests.

The FIM is another alternative for volume estimation through bioimpedance measures, which places the electrodes on a plane frontal to the object under study. The Figures 5.17

and 5.18 show the effect of the conductivity change on the impedance measurements of the classic approach FIM4 (Section 3.5.2.1) on two concentric disk. The Figures 5.17 and 5.18 show that the smaller the radius of the inner disk, the lower is the sensitivity of FIM4 with respect to changes in conductivity. These simulation results suggest that the FIM approach could be a promising alternative for volume estimation because its moderate sensitivity to conductivity changes.

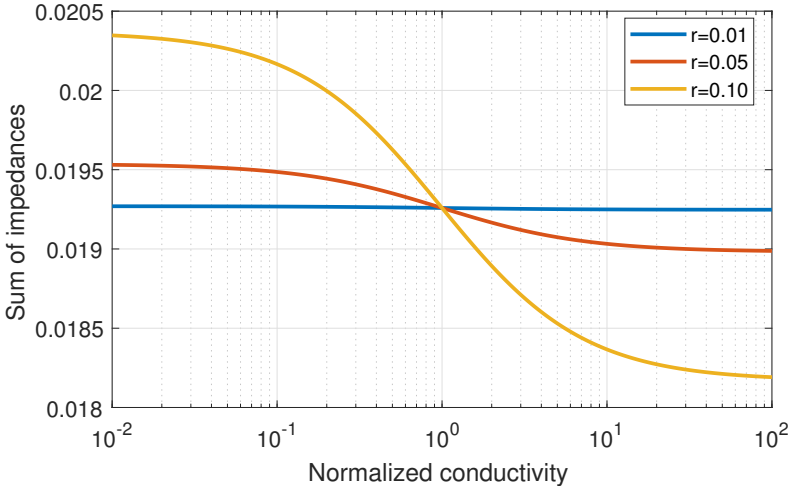

Figure 5.17: Focused impedance vs conductivity ratio for small radius of inner circle.

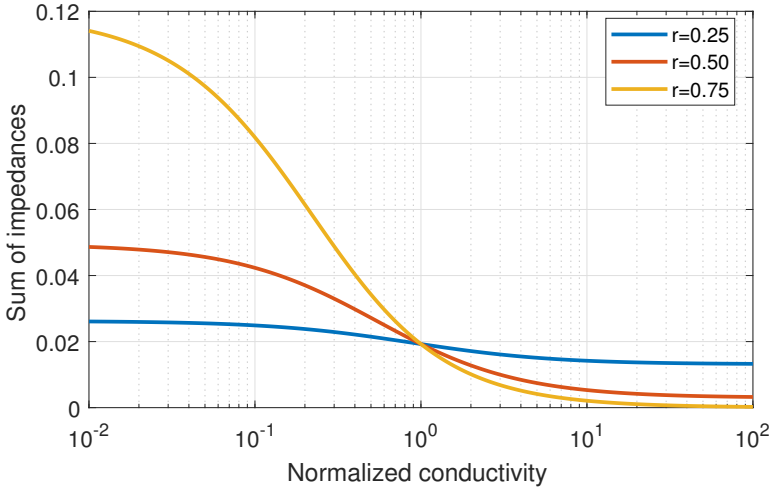

Figure 5.18: Focused impedance vs conductivity ratio for medium and big radius of the inner circle.

The sensitivity maps for the approaches based in FIM are generated through the FEM model of the bladder phantom of the Figure 4.9; the green circles represent the location of the electrodes on the phantom, according to Figure 3.4. The Figure 5.19 shows the behavior of the sensitivity when the phantom's empty cavity has a radius 5.2 cm; the results in this experiment show that the FIM4 and FIM-IE approaches have greater sensitivity in

the central zone of the phantom than FIM-I. On the other hand, in Figure 5.20 shows the difference of the sensitivity maps when the conductivity into the phantom cavity changes from 1.027 to 1.877 S/m and 1.866 and 2.61 S/m. This experiment shows that the FIM-IE index has lower sensibility to conductivity changes that FIM4 and FIM-I. Finally, from sensitivity maps results 5.19 and 5.20 can be concluded that FIM approaches are good alternative for volume estimation. Furthermore, the FIM-IE approach proposed is very promising for long-term bladder monitoring because of its lower sensitivity to conductivity changes.

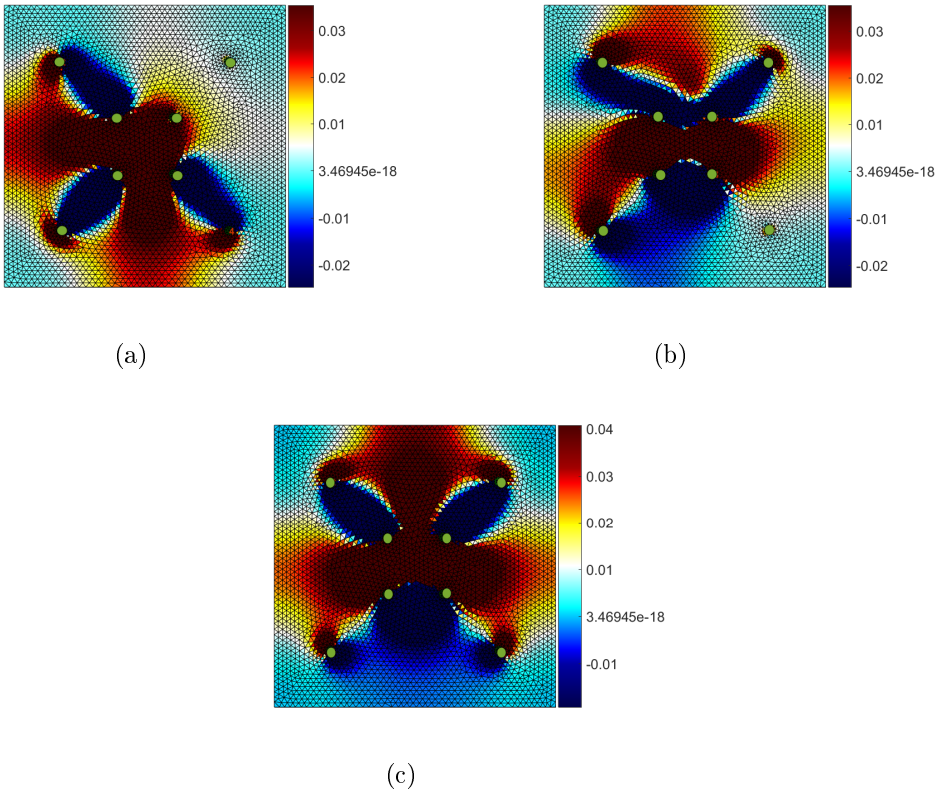

Figure 5.19: Sensitivity maps of bladder phantom with cavity of 5.2 cm of radius: a)FIM4, b) FIM-I and c) FIM-IE

We used three phantoms with cavity radii of 2.50, 4.15 and 5.20 cm, and saline solution conductivity levels of 1.207, 1.877 and 2.610 S/m considering the characteristics presented in Section 4.5.2. Hence, the total number of experimental configurations for each method (FIM-I, FIM-IE, FIM-4 and GI) is nine. Output variables for each method (electrical potential for FIM-I, FIM-IE and FIM-4, and GI) were calculated by averaging the measurements of 10 frames. For homogeneous measures, we used a reference conductivity of 0.217 S/m, which corresponds with the conductivity of the bladder wall.

For each of the four methods compared in this study, medians and interquartile ranges of all combinations of cavities and conductivities are presented in Tables 5.9, 5.10, 5.11 and 5.12. The right-most column of these tables contain p-values from Kruskal-Wallis tests for differences between median output variables for each method with varied radii of the

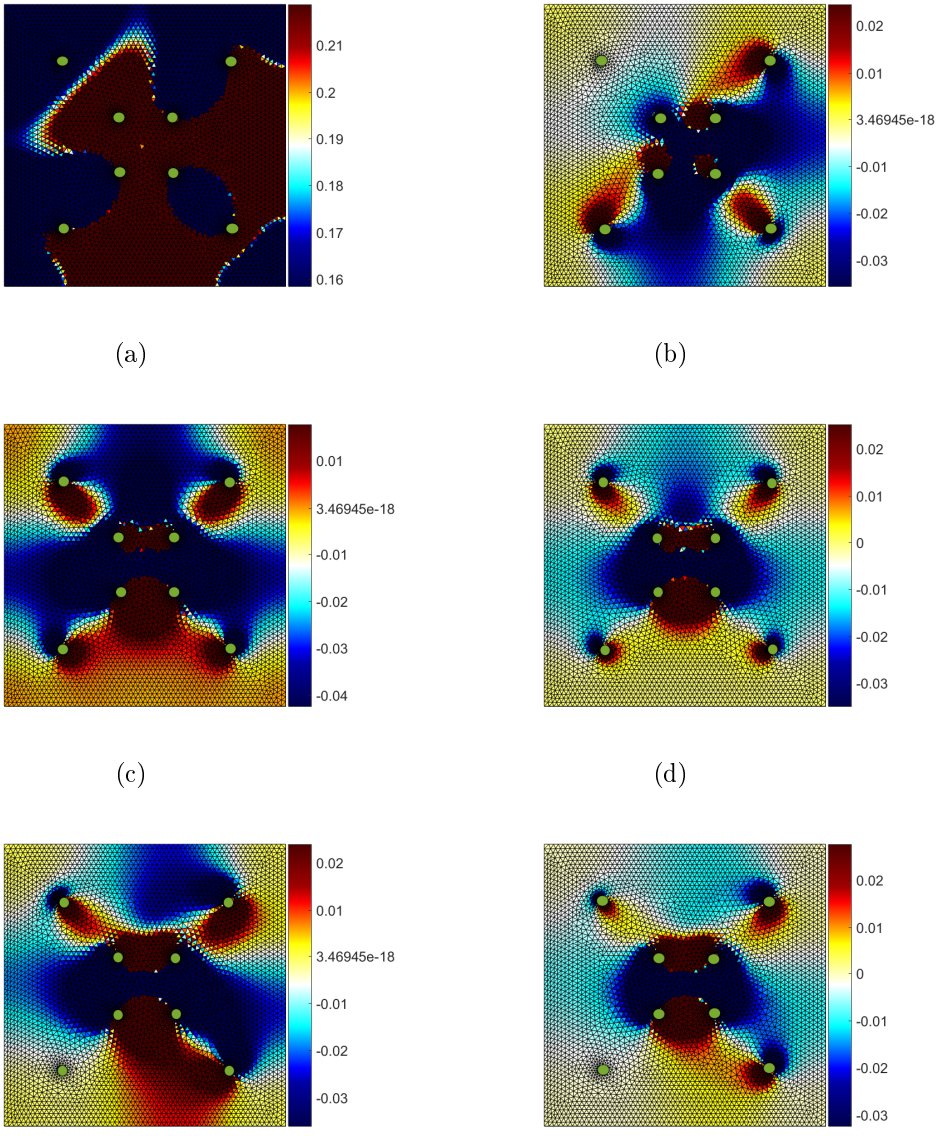

Figure 5.20: Difference between the sensitivity maps due to conductivity change from: a) 1.27 to 1.877 S/m and FIM4, b) 1.877 to 2.61 S/m and FIM4, c) 1.27 to 1.877 S/m and FIM-I, d) 1.877 to 2.61 S/m and FIM-I, e) 1.27 to 1.877 S/m and FIM-IE and f) 1.877 to 2.61 S/m and FIM-IE.

cavity and constant conductivity. Differences between output variables were considered insignificant when $p > 0.05$, which indicated failure to distinguish between volumes at the given conductivity level. Under these conditions p-values are listed in the fourth column. When p-values from Kruskal-Wallis tests are ≤ 0.05, then at least one of the cavities is giving measurements that differ from the other two. Under these conditions, all three possible comparisons of cavities must be made, and the number in the fourth column represents the comparison with the highest p-value.

In the Tables 5.9, 5.10, 5.11 and 5.12 we present p-values from Kruskal-Wallis tests for differences between measurements made at constant volumes, for which insignificant differences in conductivity ($p \leq 0.05$) were associated, indicating robustness of the method against uncertainties of conductivity. In these experiments, we used Kruskal-Wallis tests instead of a one-way ANOVA because not all data sets were normally distributed. The present bioimpedance methods were considered suitable for bladder volume estimations if they indicate significant differences between test cavities but no differences relating to conductivity, as follows:

- Table column condition: All values in the last column must be ≤ 0.05, indicating significant differences between the three test cavities.
- Table row condition: All the values in the last row must be > 0.05 indicating insignificant differences between measurements of volume despite differing conductivities.

In evaluations using the FIM-I method, electrical potential varies with increasing conductivity and constant volume (Figure 5.21). Additionally, at a conductivity value of 1.877 S/m, ΔP returned similar values for middle-sized and large cavities ($p = 0.3245$). In addition, FIM-I was sensitive to conductivity.

Table 5.9: Median $\pm$ interquartile range for the volume estimated by the FIM-I approach; p-values were calculated using Kruskal-Wallis tests for differences between median values.

		Radius of the cavity			
		Small	**Medium**	**Large**	**p-value**
S/m	**1.027**	1.31 ± 1.0	25.34 ± 2.5	32.09 ± 3.7	0.0291
	1.877	0.24 ± 0.1	28.40 ± 5.5	29.53 ± 4.8	0.3245
	2.610	0.48 ± 0.5	21.14 ± 0.8	24.17 ± 3.0	0.0294
	p-value	0.0085	≤ 0.001	≤ 0.001	

As shown in Figure 5.22, ΔP values were approximately constant for each cavity when determined using the FIM-IE method, despite the differing conductivity levels of the saline solution. The values in the last row of Table 5.10 indicate no significant differences ($p > 0.05$), whereas those in the last column of Table 5.10 show that FIM-IE measurements differ significantly for the three cavities.

As shown in Figure 5.23, electrical potential from the FIM-4 method varies with increasing conductivity and when cavity volumes are constant. Additionally, at a conductivity of 2.610 S/m, ΔP was similar for middle and large cavities. In all cases FIM-4 failed to

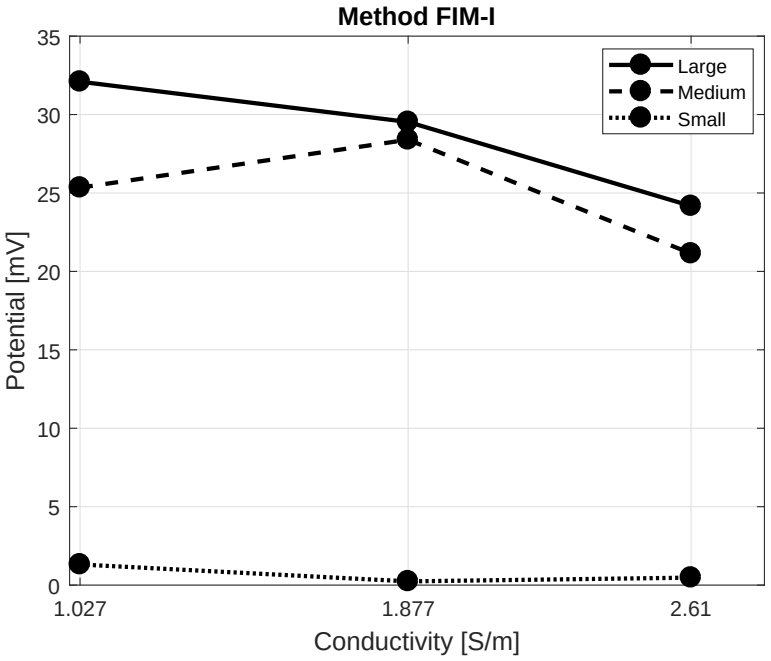

Figure 5.21: Electrical potential estimated using the FIM-I approach; solid, dashed and dotted lines represent cavities with large, medium and small radii, respectively.

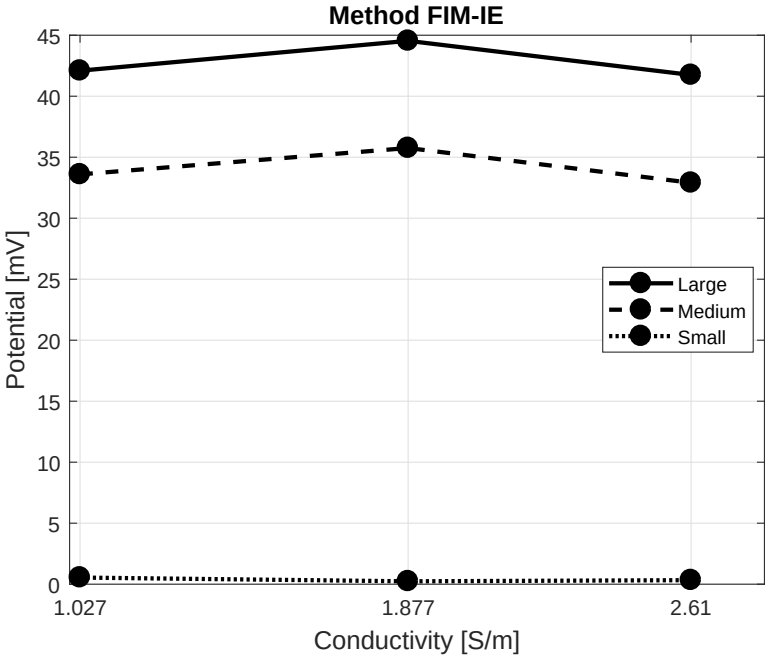

Figure 5.22: Electrical potential estimated by the FIM-IE approach; solid, dashed and dotted lines represent cavities with large, medium, and small radii, respectively.

differentiate between volumes of at least two cavities (Table 5.11, last column). Like FIM-I, measurements of electric potential from the FIM-4 approach were largely dependent on conductivity (Table 5.11).

Table 5.10: Median ± interquartile range for volume estimates from the FIM-IE approach; differences between median values were identified using Kruskal-Wallis tests.

		Radius of the cavity			
		Small	**Medium**	**Large**	**p-value**
S/m	**1.027**	0.54 ± 0.7	33.59 ± 2.9	42.09 ± 2.6	0.0298
	1.877	0.24 ± 0.1	35.75 ± 4.6	44.54 ± 5.8	0.0298
	2.610	0.33 ± 0.1	32.91 ± 1.8	41.74 ± 3.4	0.0298
	p-value	0.3320	0.1409	0.1959	

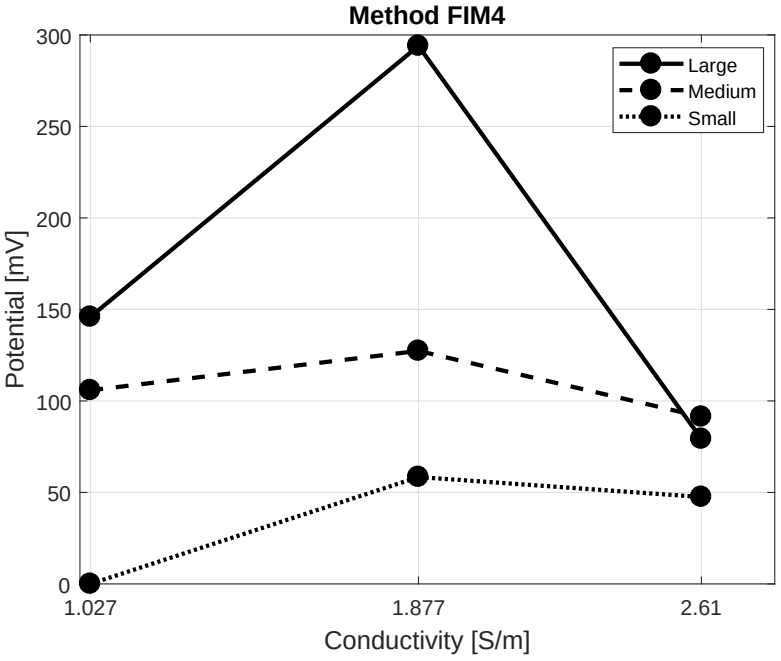

Figure 5.23: Electrical potential estimated by the FIM-4 approach; solid, dashed and dotted lines represent cavities with large, medium, and small radii, respectively.

In assessments using GI, median values varied with increasing conductivity of saline solutions (Figure 5.24) when cavity volumes were kept constant. In addition, at a conductivity of 1.027 S/m, GI values for the large cavity were less than those for the middle cavity. Yet for a conductivity of 1.877 S/m, the GI values for the large cavity were greater than for the middle-sized cavity. As listed in Table 5.12, GI fails in the row condition for all three cavity sizes, and fails the column condition for the lowest cavity size.

In summary, FIM-I, FIM4, and GI approaches do not satisfy the row condition of similar values over a range of conductivities. Specifically, all three methods are subject to electrical conductivity of saline solutions. These three methods also fail the column condition of differing measurements between different sized cavities for at least one of the cavities. In contrast, the FIM-IE approach satisfies both conditions and returns electrical potential values that vary with cavity sizes, with low sensitivity to the urine conductivity.

Table 5.11: Median ± interquartile ranges for volumes estimated by the FIM4 approach; differences between median values were identified using Kruskal-Wallis tests.

		Radius of the cavity			
		Small	**Medium**	**Large**	**p-value**
S/m	**1.027**	0.00 ± 6.2	105.82 ± 6.2	145.94 ± 24.7	0.2751
	1.877	58.39 ± 19.1	127.33 ± 154.9	294.00 ± 55.6	0.1825
	2.610	47.51 ± 16.1	91.34 ± 40.3	79.24 ± 59.6	0.4254
	p-value	≤ 0.001	0.0012	≤ 0.001	

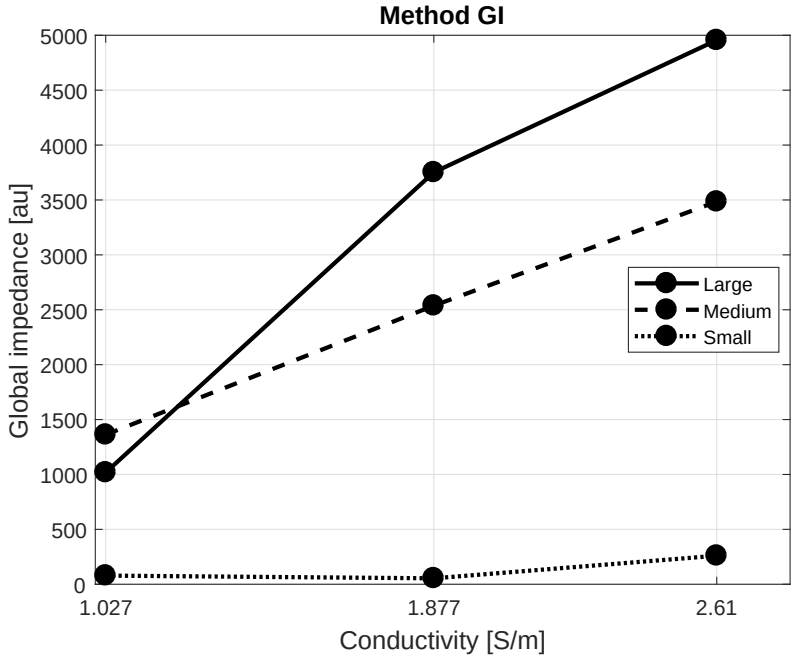

Figure 5.24: GI estimated by the GI approach; solid, dashed and dotted lines represent cavities with large, medium, and small radii, respectively.

5.6 Summary

The performance of EIT image reconstruction algorithms is discussed in Section 5.2. The high-order algorithm was used to calculate the potentials in FEM and CEM model, since it has a higher calculation speed (Table 5.1). On the other hand, the best accuracy for the reconstruction of EIT images was obtained using the combination ⟨FEM, Noser, GN-OS⟩ (Table 5.2).

With respect to electrode arrays and their effect on volume estimation; it was determined, by simulation, that the classic ring arrangement with adjacent injection and measurement patterns are the best configuration when the GI index is used (Tables 5.3 and 5.4). Although the GI index estimates the volume of an object with constant conductivity, this is not a suitable alternative for bladder monitoring, since urine presents high uncertainty in its conductivity. This is why the IRM, VCR, MVCR and FIM (FIM4, FIM-I, FIM-IE) approaches were studied; determining that the FIM-IE approach is the best alternative for long-term monitoring of the bladder due to the results on bladder phantom presented

Table 5.12: Median ± interquartile ranges for volumes estimated using the GI approach; differences between median values were identified using Kruskal-Wallis tests.

		Radius of the cavity			
		Small	**Medium**	**Large**	**p-value**
S/m	**1.027**	78.69 ± 93.2	1362.22 ± 112.5	1018.22 ± 725.5	0.6300
	1.877	54.04 ± 82.1	2537.48 ± 103.4	3751.78 ± 462.0	0.0292
	2.610	259.72 ± 32.8	3484.70 ± 26.3	4955.52 ± 128.9	0.0296
	p-value	0.0012	≤ 0.001	≤ 0.001	

in Section 5.5.

6 Discussion and Conclusions

6.1 Introduction

In this chapter, we discuss: i) the biological process selected to design the EIT system, ii) the performance of the EIT system to monitoring the biological process under study iii) the algorithms to solve forward and inverse EIT problems and the spatial arrangement of electrodes and the patterns for current injection and voltage measurement, iv) the in-vitro performance of GI, VCR, MRI and MVCR for constant and non-constant conductivity.

6.2 Biological process to study with EIT system of low temporal and spatial resolution

The bibliographic review presented in Section 2.2 shows that current signals of 1 mA at 50 kHz are the commonly used in EIT image reconstruction. Additionally, [91] and [3] point out that a system with low spatial resolution (8 electrodes) presents good performance in biomedical applications. With regard to the temporal variability of the conductivity of biological processes, the urinary and cerebral systems require low frame rates.

In this thesis the bladder volume was selected as case study because it presents a low temporal variability of its conductivity. However, the results presented in [15, 73, 132, 133] show that the uncertainty of the urine generates erroneous estimates of the bladder volume, which is a limitation for long-term monitoring. In this work, an algorithm based on FIM was proposed, which presents low sensitivity to the uncertainty of conductivity, being a promising alternative for long-term monitoring of bladder size as evidenced in Figure 5.22.

According to Figures 5.9, 5.11 and 5.12, when using a simple ring configuration, GI, VCR and MVCR differentiate objects with different volume but with the same conductivity. These methods have relative and absolute errors lower than 1.90% and 11.56%, respectively. Furthermore, the interquartile ranges (Tables 5.7, 5.9, 5.10 and 5.11) indicate that

GI, VCR, and MVCR have low sensitivity to noise. On the other hand, in the case of the IRM method, it does not detect small objects, which is in agreement with [133].

6.3 Performance of EIT image reconstruction

The EIT forward problem is solved using the finite element method that consists of discretizing the object under study and its environment to produce a geometric structure called mesh. The mesh density in the vicinity of the electrodes is used to estimate voltage gradients through the Newman conditions (Eq. 3.4). These estimates were obtained using higher order and first order algorithms, which presented the same errors for the four experiments considered in Table 5.1. These results are in agreement with [178], which through simulation analyzed the converge of a 2D forward problem. This thesis extended the results of [178] to a 3D forward problem, in addition to using real data. The Table 5.1 also showed that in all experiments, the higher order algorithm has a shorter calculation time than the first-order algorithm. These same observations were also reported in [177] and [178].

Regarding reconstruction algorithms, we found that the combination ⟨FEM, Noser, GN-OS⟩ gave the lowest error, while ⟨FEM, Laplace, GN⟩ had the worst performance (Table 5.2). On the contrary, [8] reports that this last triplet had the best performance. This discrepancy originates from the number of electrodes; 8 in our case and 16 in the other. In [223], ⟨Total Variation, GN⟩ and ⟨Noser, GN⟩ had better performance that ⟨Laplace, GN⟩. Our results suggest that 8 electrodes for EIT image reconstruction are enough to estimate the size and conductivity of an object when the combination ⟨FEM, Noser, GN-OS⟩ is employed.

6.4 Analysis of electrodes arrangement and injection and measurement patterns in volume estimation

With respect to electrode configuration, RN ad-ad led to the smallest absolute errors for noise and noise-free measurements (Table 5.5). This last result is in disagreement with [46], which found that double ring, quadruple ring, double ventral semicircular, and 4x4 matrix performed better than RN. Considering that the forward models used here and in [46] were similar, the difference in the results can be explained by the number of electrodes employed in each study; while we used 8 electrodes, [46] used 16. This indicates that the accuracy in the estimation of the volume is highly affected by the number of the electrodes when the RN configuration is used.

As presented in Figures 5.4 to 5.8, the injection and measurement patterns influence volume estimation. The electrode arrangements CN, H2L, RN, SC, and V2L presented a RMS volume estimation error between 22.3% and 40.9%, when the opposite pattern was used either for injection or measurement (Table 5.5). The effects of injection and

measurement patterns on volume estimation using GI is a topic that, to the best of our knowledge, has not been analyzed, so our work provides an important contribution in this regard.

The obtained results suggest that for 8 electrodes the RN ad-ad configuration is the best alternative for volume estimation when the electrodes are located in a transverse plane. On the other hand, if several transverse planes are considered to locate the electrodes, the V2L ad-ad configuration is the best alternative.

The Figures 5.13 and 5.19 show that the FIM-I and FIM IE electrode arrangements proposed in this thesis, and FIM4 proposed in [211] present a higher sensitivity in the central region than those based on the single ring configuration. This suggests that the former are more appropriate for detecting conductivity changes of small volume objects. However, this claim is challenged by the experimental results presented in the first column of Tables 5.9 to 5.12, where only FIM-IE cannot distinguish changes in conductivity. Here it is important to clarify that this feature of FIM-IE is not a disadvantage but an advantage, considering that for bladder volume monitoring, the approach is to obtain volume estimates robust to the uncertainty of conductivity.

6.5 Performance of volume estimation through bioimpedance measurements

The linear relationship between $|GI|^{-1}$ and volume was confirmed in our in-vitro experiments (Section 5.4), as in [132–135]. The Figure 5.9 indicates that the volume of the steel spheres is linearly correlated with $|GI|^{-1}$. The interquartile ranges, lower than $3.5E-4$, reveal the low sensitivity of $|GI|^{-1}$ to measurement noise (Table 5.7). In addition, the Kruskal Wallis test (Table 5.8) confirmed that the difference between the $|GI|^{-1}$ values for each sphere were significant ($p \leq 0.001$). These results suggest that GI is viable for volume monitoring when 8 electrodes, in single ring configuration, are used.

In this thesis, the volume of the steel spheres was also estimated using bioimpedance approaches, which do not require of image reconstruction algorithms:

- The median values of the IRM measurements significantly differ for the three spheres (Table 5.8); however, they do not correlate positively or negatively with the volume of the sphere. The Table 5.6 shows that the medium sphere has the lowest median, while the small sphere has the largest median. This is because when the object under study is symmetrically located with respect to the electrodes, the front, rear and side voltages are the same, and as a consequence the IRM becomes a quotient of noises (Equation 5.4). This fact makes IRM unsuitable for bladder volume estimation.
- The Figure 5.11 shows that the VCR measurements for each sphere do not overlap. The Table 5.8 evidences that the median values of the VCR measurements significantly differ for the three spheres and positively correlate with their volume

(Table 5.6). This positive correlation was also observed in [74] for human bladder monitoring. Furthermore, [74] found a linear correlation between bladder volume and VCR measurements.

- MVCR, proposed as part of this thesis, is an extension of VCR that uses eight voltage measurements to improve robustness against noise. As seen in Table 5.6, the interquartile ranges for MCVR are lower than those for VCR. Like VCR, MVCR leads to significant differences in the measurements for each sphere (Table 5.8).

The results obtained with the metallic spheres and the saline solution show that GI, VCR and MVCR are suitable approaches for volume monitoring when the conductivity of the object under study is unknown but constant. VCR had the highest sensitivity to volume variation, while MVCR had the highest noise robustness. Both VCR and MVCR are easier to implement than GI because they do not require an image reconstruction algorithm.

The Figures 5.15 and 5.16 show that when the volume remains constant but the conductivity varies, the VCR and MVCR estimates also vary, making it impossible to distinguish between changes in volume and changes in conductivity. GI suffers from the same problem as VCR and MVCR because it is calculated as the sum of the conductivity pixels of an image; and as a consequence, a large moderate-conductivity object can have the similar GI as a medium, high-conductivity object (Figure 5.24).

The bioimpedance approaches used in this thesis detect changes in volume when the conductivity of the object under study remains constant. Furthermore, these methods require less computational effort than the GI approach, which is based on differential EIT and as consequence requires to solve inverse problem.

6.6 Robustness of the bladder volume estimation against uncertainty of urine conductivity

Fundamental to deciding whether a bioimpedance approach can be used to inform bladder volume in people with UI is whether the method estimates the volume of an object with unknown conductivity. To address this limitation, we compared GI with three FIM approaches. Specifically, we determined whether each approach differentiates between three cavities of different volumes of liquid with unknown conductivity.

GI has been recently proposed to estimate bladder volumes, predominantly because a linear relationship with volumes of objects has been shown. In a previous study [134] of nine male paraplegic patients, a strong Pearson's correlation was reported between GI and bladder volume. This correlation was negative for four patients because the conductivity of urine is higher than that of surrounding organs. Yet, positive correlations were identified in other five patients, and these were attributed to bladder movements outside measurement areas. In all of the present experiments with GI (Figure 5.24), these correlations were negative because the conductivities of the saline solutions (1.027, 1.877,

and 2.610 S/m) were higher than that of the background (0.217 S/m). In a previous study [134], conductivity was kept constant in urine samples by filling bladders with a contrast fluid of known conductivity. As a consequence, the effects of electrical properties of urine were not investigated in their study. Additionally, the effects of patient urine production were reduced by performing the experiment over only 30 min.

In a simulation study comparing errors of volume estimates, noise tolerance, and sensitivity to urine conductivity of GI with those of three EIT-based methods [132], average errors were lower than 5% and had insignificant standard deviations after calibrating the equation relating volume with GI. But changes in urine conductivity required further calibration to avoid over or under-estimation of volumes. In another study, GI was compared with other bioimpedance approaches [17], and GI values largely depended on the conductivity of urine. The data presented herein (Table 5.12) show that for a constant fluid volume significant differences ($p < 0.05$) in GI values follow conductivity changes. These results are in agreement with previous studies [132], [17], indicating that GI can be used to estimate volumes only when conductivity of the object under study remains constant.

The FIM-4 approach was proposed in a previous study [224], and comprises two mutually orthogonal tetrapolar measurements to estimate the impedance of an object that is located below the plane formed by the electrodes. Based on FIM-4, a method for organ volume estimation was proposed [225], and it was shown that simulations that are based on finite elements give linear relationships between volumes of study objects and sensitivity, which is defined as the quotient of impedance variation and the distance between electrodes. In addition, simulation experiments that were performed in a saline tank demonstrated that the constant that relates volume and sensitivity depends on the conductivity of the object and on its depth with respect to the plane of electrodes. Similarly, we show that for a constant volume, the values given by FIM-I and FIM-4 approaches depend on the conductivity of the saline solution (Tables 5.9 and 5.11). Our experiments with FIM-IE, however, showed no dependence of volume measurements on the conductivity of saline solutions (Table 5.10), and strict dependence on the volume of the cavity. The main difference between these three FIM approaches is the additional information required to calculate variations of electrical potential. Unlike FIM-I and FIM-4 procedures, FIM-IE is performed by injecting current and measuring voltage on internal and external electrodes. When current is injected through internal electrodes, voltage is measured at the external electrodes, and *vice versa*.

Each of the present bioimpedance approaches for estimating bladder volumes requires a calibration procedure that begins by emptying the patient's bladder and then using urodynamics to relate bladder volumes to the bioimpedance variable. The resulting equations relate measurements with volumes but are only valid when urine conductivity is equal to that during the calibration phase. Because urine conductivity varies physiologically, it is important to use bioimpedance approaches for which measured variables are independent of urine conductivity. Herein, we demonstrate that the FIM-IE approach meets these criteria, although more tests are required. Initially, such tests will require a phantom bladder with irregularly shaped cavities of variable volume that allow experiments with more than three volumes. Additionally, to make the phantom prototype more realistic, the container

will be cylindrical and the electrodes will be placed on its front side. Another aspect to consider in future experiments is that the conductivity of urine in the bladder is not constant as its volume increases. The ensuing experiments will verify the generalizability of the FIM-IE approach.

Finally, the results obtained in this thesis lead us to conclude that the proposed FIM-IE approach has low sensitivity against conductivity uncertainty, allowing a volume monitoring to long-term; contrary to the performance show the VCR, IRM and GI indices, which have high sensibility to conductivity uncertainty as is reported in [17, 74, 132, 134]. On the other hand, the developed 8-electrode EIT system is a novel low-cost alternative for monitoring biological processes with low temporal variability of their conductivity. Whereby the FIM-IE and the 8-electrode EIT system, based in the AFE4300 device, are a promising alternative for long-term bladder monitoring. Our contribution seeks to avoid catheterization processes in patients with loss of micturition sensation, and as a consequence potential risks of infection for the urinary system.

Unlike the VCR, MRI, and GI approaches, which are highly sensitive to conductivity changes [17, 74, 132, 134], FIM-IE is very robust to uncertainty in this variable, making it suitable for long-term bladder volume monitoring. Therefore, FIM-IE combined with the proposed EIT system is a promising alternative to avoid catheterization in patients with loss of voiding sensation.

In-vivo testing will be the next step in this research project, with the aim of establishing a correlation between FIM-IE and the volume of the human bladder. The time and complexity required to include an experimental phase with patients, including approval of equipment by national agencies, establishment of collaboration with a research hospital and approval of experiments by ethical committees have prevented us to include this phase in the thesis, which has been performed in an electrical engineering department.

Bibliography

[1] Texas-Instruments. Datasheet-AFE4300-Low-Cost, Integrated Analog Front-End for Weight-Scale and Body Composition Measurement. *Dallas, Texas, USA*, 2012.

[2] R Harikumar, R Prabu, and S Raghavan. Electrical impedance tomography (EIT) and its medical applications: a review. *Int J Soft Comp Eng*, 3(4):193–8, 2013.

[3] S. Bentolhoda Ayati, Kaddour Bouazza-Marouf, and David Kerr. In vitro localisation of intracranial haematoma using electrical impedance tomography semi-array. *Medical Engineering & Physics*, 37(1):34 – 41, 2015.

[4] Jianling Gao, Shihong Yue, Jun Chen, and Huaxiang Wang. Classification of normal and cancerous lung tissues by electrical impendence tomography. *Bio-medical materials and engineering*, 24(6):2229–2241, 2014.

[5] Rihui Li, Jinwu Gao, Yaning Li, Junpeng Wu, Zhanqi Zhao, and Yang Liu. Preliminary study of assessing bladder urinary volume using electrical impedance tomography. *Journal of Medical and Biological Engineering*, 36(1):71–79, 2016.

[6] Julien Bordes, Philippe Goutorbe, Pierre Julien Cungi, Marie Caroline Boghossian, and Eric Kaiser. Noninvasive ventilation during spontaneous breathing anesthesia: an observational study using electrical impedance tomography. *Journal of Clinical Anesthesia*, 34:420 – 426, 2016.

[7] Josep Solà, Andy Adler, Arnoldo Santos, Gerardo Tusman, Fernando Suárez Sipmann, and Stephan H. Bohm. Non-invasive monitoring of central blood pressure by electrical impedance tomography: first experimental evidence. *Medical & Biological Engineering & Computing*, 49(4):409–415, 2011.

[8] M. R. Islam and M. A. Kiber. Electrical impedance tomography imaging using gauss-newton algorithm. In *Informatics, Electronics Vision (ICIEV), 2014 International Conference on*, pages 1–4, May 2014.

[9] M. Proença, F. Braun, E. Muntané, J. Solà, A. Adler, M. Lemay, J. P. Thiran, and S. F. Rimoldi. Non-invasive monitoring of pulmonary artery pressure at the bedside. In *2016 38th Annual International Conference of the IEEE Engineering in Medicine and Biology Society (EMBC)*, pages 4236–4239, Aug 2016.

[10] Martin Proença, Fabian Braun, Josep Solà, Jean-Philippe Thiran, and Mathieu Lemay. Noninvasive pulmonary artery pressure monitoring by EIT: a model-based feasibility study. *Medical & Biological Engineering & Computing*, pages 1–15, 2016.

[11] M Balleza-Ordaz, E Perez-Alday, M Vargas-Luna, and JP Riu. Tidal volume monitoring by electrical impedance tomography (EIT) using different regions of interest (ROI): Calibration equations. *Biomedical Signal Processing and Control*, 18:102–109, 2015.

[12] Venkatratnam Chitturi, Nagi Farrukh, Vinesh Thiruchelvam, and Thang Ka Fei. A Low Cost Electrical Impedance Tomography (EIT) for Pulmonary Disease Modelling and Diagnosis. In *The Second International Conference on Technological Advances in Electrical, Electronics and Computer Engineering (TAEECE2014)*, pages 83–89. The Society of Digital Information and Wireless Communication, 2014.

[13] A. Fouchard, A. Noca, S. Bonnet, P. Pham, V. Sinniger, D. Clarençon, and O. David. Modular architecture of a multi-frequency electrical impedance tomography system: Design and implementation. In *2014 36th Annual International Conference of the IEEE Engineering in Medicine and Biology Society*, pages 6076–6079, Aug 2014.

[14] Ji Huang, Yi Hung, Jhi Wang, and Bor Lin. Design of wearable and wireless electrical impedance tomography system. *Measurement*, 78:9 – 17, 2016.

[15] T. Schlebusch, S. Nienke, S. A. Santos, and S. Leonhardt. Bladder volume estimation from electrical impedance tomography. In *2013 35th Annual International Conference of the IEEE Engineering in Medicine and Biology Society (EMBC)*, pages 6441–6444, July 2013.

[16] You-Jung Han, Anil Kumar Khambampati, and Kyung-Youn Kim. Performance analysis of eit bladder monitoring system according to input current patterns. *Journal of IKEEE*, 23(1):164–172, 2019.

[17] Thomas Schlebusch, Jakob Orschulik, Jaakko Malmivuo, Steffen Leonhardt, Dorothea Leonhäuser, Joachim Grosse, Michael Kowollik, Ruth Kirschner-Hermanns, and Marian Walter. Impedance ratio method for urine conductivity - invariant estimation of bladder volume. *Journal of Electrical Bioimpedance*, 5(1):48–54, 2019.

[18] Clare T. Soulsby, Mandeep Khela, Etsuro Yazaki, David F. Evans, Enid Hennessy, and Jeremy Powell-Tuck. Measurements of gastric emptying during continuous nasogastric infusion of liquid feed: Electric impedance tomography versus gamma scintigraphy. *Clinical Nutrition*, 25(4):671 – 680, 2006.

[19] Fridrun Podczeck, Catherine L Mitchell, J Michael Newton, David Evans, and Michael B Short. The gastric emptying of food as measured by gamma-scintigraphy and electrical impedance tomography (EIT) and its influence on the gastric emptying of tablets of different dimensions. *Journal of pharmacy and pharmacology*, 59(11):1527–1536, 2007.

[20] Feng Fu, Bing Li, Meng Dai, Shi-Jie Hu, Xia Li, Can-Hua Xu, Bing Wang, Bin Yang, Meng-Xing Tang, Xiu-Zhen Dong, Zhou Fei, and Xue-Tao Shi. Use of electrical impedance tomography to monitor regional cerebral edema during clinical dehydration treatment. *PLOS ONE*, 9(12):1–15, 12 2014.

[21] Gregory Boverman, Tzu-Jen Kao, Xin Wang, Jeffrey M Ashe, David M Davenport, and Bruce C Amm. Detection of small bleeds in the brain with electrical impedance tomography. *Physiological measurement*, 37(6):727, 2016.

[22] Seyed Reza Atefi, Fernando Seoane, Shervin Kamalian, Eric Rosenthal, Michael Lev, and Giorgio Bonmassar. Intracranial haemorrhage alters scalp potential distributions in bioimpedance cerebral monitoring applications : preliminary results from FEM simulation on a realistic head model and human subjects. *Medical Physics*, 43(2):675–686, 2016. QC 20170111.

[23] Alicia C Everitt, Brandon K Root, David F Bauer, and Ryan J Halter. Electrical impedance mapping for localizing evolving traumatic brain injury. In *Medical Imaging 2019: Biomedical Applications in Molecular, Structural, and Functional Imaging*, volume 10953, page 109530W. International Society for Optics and Photonics, 2019.

[24] Atsushi Nishida, Wook-Cheol Kim, Takashi Yoshida, Yoshinobu Oka, Naotake Yamada, Masashi Nakase, Kazuya Ikoma, Hiroyoshi Fujiwara, Noboru Ishikawa, Hiroshi Ikegaya, and Toshikazu Kubo. A new method for the estimation of age at death by using electrical impedance: A preliminary study. *Legal Medicine*, 17(6):560 – 568, 2015.

[25] Avihai Ron, Shimon Abboud, and Marina Arad. Home monitoring of bone density in the wrist—a parametric EIT computer modeling study. *Biomedical Physics & Engineering Express*, 2(3):035002, 2016.

[26] A.H. Dell'Osa. Bone electrical impedance and tomographic reconstruction of fracture detection: A review. volume 54, pages 12–15, 2016. cited By 0.

[27] Shani Kimel-Naor, Shimon Abboud, and Marina Arad. Parametric electrical impedance tomography for measuring bone mineral density in the pelvis using a computational model. *Medical Engineering & Physics*, 38(8):701 – 707, 2016.

[28] World Health Organization et al. Formulación de políticas sobre dispositivos médicos. 2012.

[29] Kelly Johanna Salazar Flórez, Sergio Botero Botero, and Claudia Nelcy Jiménez Hernández. Adquisición de tecnología biomédica en IPS colombianas: comparación y mejores prácticas. *Revista Gerencia y Políticas de Salud*, 15:88 – 118, 12 2016.

[30] Yan Wang, Florent Seguro, Evan Kao, Yue Zhang, Farshid Faraji, Chengcheng Zhu, Henrik Haraldsson, Michael Hope, David Saloner, and Jing Liu. Segmentation of lumen and outer wall of abdominal aortic aneurysms from 3D black-blood MRI with a registration based geodesic active contour model. *Medical Image Analysis*, 40:1 – 10, 2017.

[31] Andrés O'Brien, Roberto Oyanedel, Alvaro Huete, et al. Masas suprarrenales: evaluación por tomografía computada y resonancia magnética. *Revista chilena de radiología*, 15(1):31–38, 2009.

[32] Aleida Flores Mamani. Resonancia magnética nuclear (RMN) en odontología. *Revista de Actualización Clínica Investiga*, 38:1892, 2013.

[33] Brian H Brown. Medical impedance tomography and process impedance tomography: a brief review. *Measurement Science and Technology*, 12(8):991, 2001.

[34] Frederick D Coffman and Stanley Cohen. Impedance measurements in the biomedical sciences. *Studies In Health Technology And Informatics*, 185:185 – 205, 2013.

[35] Tushar Kanti Bera. Bioelectrical impedance methods for noninvasive health monitoring: a review. *Journal of medical engineering*, 2014, 2014.

[36] M. Wang. Electrical impedance tomography. In Mi Wang, editor, *Industrial Tomography*, Woodhead Publishing Series in Electronic and Optical Materials, pages 23 – 59. Woodhead Publishing, 2015.

[37] J. Bruno de Lema, Ernesto Serrano, Teresa Feixas, Núria Calaf, María del Valle Camacho, Pere J. Riu, and Pere Casan. Evaluación de la función pulmonar unilateral mediante tomografía por impedancia eléctrica. 44(8):408 – 412, 2008.

[38] Jane Kobylianskii, Alistair Murray, Debbie Brace, Ewan Goligher, and Eddy Fan. Electrical impedance tomography in adult patients undergoing mechanical ventilation: A systematic review. *Journal of Critical Care*, 35:33 – 50, 2016.

[39] J. Riera, P.J. Riu, P. Casan, and J.R. Masclans. Electrical impedance tomography in acute lung injury. *Medicina Intensiva (English Edition)*, 35(8):509 – 517, 2011.

[40] V. Sobota and J. Suchomel. Monitoring of pulmonary embolism using electrical impedance tomography: A case study. In *E-Health and Bioengineering Conference (EHB), 2013*, pages 1–4, Nov 2013.

[41] Zhanqi Zhao, Rainald Fischer, Inéz Frerichs, Ullrich Müller-Lisse, and Knut Möller. Regional ventilation in cystic fibrosis measured by electrical impedance tomography. *Journal of Cystic Fibrosis*, 11(5):412 – 418, 2012.

[42] Kirill Y. Aristovich, Brett C. Packham, Hwan Koo, Gustavo Sato dos Santos, Andy McEvoy, and David S. Holder. Imaging fast electrical activity in the brain with electrical impedance tomography. *NeuroImage*, 124, Part A:204 – 213, 2016.

[43] Illapha Cuba-Gyllensten, Paloma Gastelurrutia, Alberto G. Bonomi, Jarno Riistama, Antoni Bayes-Genis, and Ronald M. Aarts. A method to adapt thoracic impedance based on chest geometry and composition to assess congestion in heart failure patients. *Medical Engineering & Physics*, 38(6):538 – 546, 2016.

[44] S. Ahmad, Silu Chen, K. Soueidan, I. Batkin, M. Bolic, H. Dajani, and V. Groza. Electrocardiogram-assisted blood pressure estimation. *Biomedical Engineering, IEEE Transactions on*, 59(3):608–618, March 2012.

[45] International Electrotechnical Commission et al. Medical electrical equipment-part 1: General requirements for basic safety and essential performance. *IEC 60601-1: 2005*, 2005.

[46] Thomas Schlebusch and Steffen Leonhardt. Effect of electrode arrangements on bladder volume estimation by electrical impedance tomography. In *Journal of Physics: Conference Series*, volume 434, page 012080. IOP Publishing, 2013.

[47] Kai Petersen, Sairam Vakkalanka, and Ludwik Kuzniarz. Guidelines for conducting systematic mapping studies in software engineering: An update. *Information and Software Technology*, 64:1 – 18, 2015.

[48] Charles Polk and Elliot Postow. *Handbook of Biological Effects of Electromagnetic Fields, -2 Volume Set*. CRC press, 1995.

[49] Andrés Sánchez-Iglesias, Milagros Fernández-Lucas, and José L Teruel. Fundamentos eléctricos de la bioimpedancia. *Nefrología (Madrid)*, 32(2):133–135, 2012.

[50] Brian H Brown and Andrew D Seagar. The sheffield data collection system. *Clinical Physics and Physiological Measurement*, 8(4A):91, 1987.

[51] Olavo Luppi Silva, Raul Gonzalez Lima, Thiago Castro Martins, Fernando Silva de Moura, Renato Seiji Tavares, and Marcos Sales Guerra Tsuzuki. Influence of current injection pattern and electric potential measurement strategies in electrical impedance tomography. *Control Engineering Practice*, 58:276–286, 2017.

[52] Marc Bodenstein, Matthias David, and Klaus Markstaller. Principles of electrical impedance tomography and its clinical application. *Critical care medicine*, 37(2):713–724, 2009.

[53] Xicai Yue and Chris McLeod. FPGA design and implementation for EIT data acquisition. *Physiological measurement*, 29(10):1233, 2008.

[54] Ryan J Halter, Alex Hartov, and Keith D Paulsen. A broadband high-frequency electrical impedance tomography system for breast imaging. *IEEE Transactions on biomedical engineering*, 55(2):650–659, 2008.

[55] Susana Aguiar Santos, Anne Robens, Anna Boehm, Steffen Leonhardt, and Daniel Teichmann. System Description and First Application of an FPGA-Based Simultaneous Multi-Frequency Electrical Impedance Tomography. *Sensors (14248220)*, 16(8):1 – 21, 2016.

[56] X. Shi, F. You, C. Xu, Z. Ji, R. Liu, X. Dong, F. Fu, and X. Huo. Design and implementation of a high-precision electrical impedance tomography data acquisition system for brain imaging. In *2016 IEEE Biomedical Circuits and Systems Conference (BioCAS)*, pages 9–15, Oct 2016.

[57] Shadab Khan, Preston Manwaring, Andrea Borsic, and Ryan Halter. FPGA-based voltage and current dual drive system for high frame rate electrical impedance tomography. *IEEE Transactions on Medical Imaging*, 34(4):888–901, 2015.

[58] Perepelitsyn Artem and Shulga Dmitry. FPGA technologies in medical equipment: Electrical impedance tomography. *Proceedings of IEEE East-West Design and Test Symposium, EWDTS 2013*, pages 0–3, 2013.

[59] Guizhi Xu, Renping Wang, Shuai Zhang, Shuo Yang, Gusphyl A Justin, Mingui Sun, and Weili Yan. A 128-electrode three dimensional electrical impedance tomography system. In *Engineering in Medicine and Biology Society, 2007. EMBS 2007. 29th Annual International Conference of the IEEE*, pages 4386–4389. IEEE, 2007.

[60] Hun Wi, H. Sohal, A.L. McEwan, Eung Je Woo, and Tong In Oh. Multi-frequency electrical impedance tomography system with automatic self-calibration for long-term monitoring. *IEEE Transactions on Biomedical Circuits and Systems*, 8(1):119–128, 2014.

[61] S Khan, A Borsic, Preston Manwaring, Alexander Hartov, and Ryan Halter. FPGA based high speed data acquisition system for electrical impedance tomography. In *Journal of Physics: Conference Series*, volume 434, page 012081. IOP Publishing, 2013.

[62] Z. Zhang, F. Dong, and C. Xu. Data acquisition system based on Compact PCI bus and FPGA for electrical resistance tomography. In *2011 Chinese Control and Decision Conference (CCDC)*, pages 3538–3543, May 2011.

[63] Yi Zeng, Lijun Xu, Zhang Cao, and Shuilong Ma. FPGA-based implementation of Prony demodulation in the multi-frequency EIT system. *Conference Record - IEEE Instrumentation and Measurement Technology Conference*, pages 548–552, 2011.

[64] Illia Kukharenko and Vitalii Kotovskyi. Low power bioimpedance tracking system for stress and activity monitoring. In *2017 IEEE 37th International Conference on Electronics and Nanotechnology (ELNANO)*, pages 288–291. IEEE, 2017.

[65] Mohammad Khalighi, Bijan Vosoughi Vahdat, Mohammad Mortazavi, Wei Hy, and Manuchehr Soleimani. Practical design of low-cost instrumentation for industrial Electrical Impedance Tomography (EIT). In *Instrumentation and Measurement*

Technology Conference (I2MTC), 2012 IEEE International, pages 1259–1263. IEEE, 2012.

[66] T Oh, O Gilad, A Ghosh, Martin Schuettler, and David S Holder. A novel method for recording neuronal depolarization with recording at 125–825 hz: implications for imaging fast neural activity in the brain with electrical impedance tomography. *Medical & biological engineering & computing*, 49(5):593–604, 2011.

[67] Thomas Dowrick, G Sato Dos Santos, Anna Vongerichten, and David Holder. Parallel, multi frequency eit measurement, suitable for recording impedance changes during epilepsy. *Journal of Electrical Bioimpedance*, 6(1):37–43, 2015.

[68] Andy Adler, Pascal Olivier Gaggero, and Yasheng Maimaitijiang. Adjacent stimulation and measurement patterns considered harmful. *Physiological measurement*, 32(7):731, 2011.

[69] David C Barber and Andrew D Seagar. Fast reconstruction of resistance images. *Clinical Physics and Physiological Measurement*, 8(4A):47, 1987.

[70] Vinko Tomicic and Rodrigo Cornejo. Lung monitoring with electrical impedance tomography: technical considerations and clinical applications. *Journal of thoracic disease*, 11(7):3122, 2019.

[71] Marco Salucci and Giacomo Oliveri. Robust real-time inversion of electrical impedance tomography data for human lung ventilation monitoring. *Microwave and Optical Technology Letters*, 61(1):5–8, 2019.

[72] Júlia NG Lima, Melissa S Fontes, Tatiana Szmuszkowicz, Alexandre M Isola, and Alexandre T Maciel. Electrical impedance tomography monitoring during spontaneous breathing trial: Physiological description and potential clinical utility. *Acta Anaesthesiologica Scandinavica*, 2019.

[73] Bin Yang, Bing Li, Canhua Xu, Shijie Hu, Meng Dai, Junying Xia, Peng Luo, Xuetao Shi, Zhanqi Zhao, Xiuzhen Dong, et al. Comparison of electrical impedance tomography and intracranial pressure during dehydration treatment of cerebral edema. *NeuroImage: Clinical*, page 101909, 2019.

[74] Yaning Li, Yinglin Peng, Xin Yang, Shipei Lu, Jinwu Gao, Chengguang Lin, and Rihui Li. Analysis of measurement electrode location in bladder urine monitoring using electrical impedance. *Biomedical engineering online*, 18(1):34, 2019.

[75] Gregory Hansen, Tanya Holt, and Jeffrey Dmytrowich. Thoracic electrical impedance tomography to minimize right heart strain following cardiac arrest. *Annals of pediatric cardiology*, 12(3):315, 2019.

[76] Aline M. Ambrosio, Tatiana PA Carvalho Kamakura, Keila K. Ida, Barbara Varela, Felipe SRM. Andrade, Lara L. Facó, and Denise T. Fantoni. Ventilation distribution assessed with electrical impedance tomography and the influence of tidal volume, recruitment and positive end-expiratory pressure in isoflurane-anesthetized dogs. *Veterinary Anaesthesia and Analgesia*, 2017.

[77] Bartłomiej Grychtol, Gunnar Elke, Patrick Meybohm, Norbert Weiler, Inéz Frerichs, and Andy Adler. Functional Validation and Comparison Framework for EIT Lung Imaging. *PLoS ONE*, 9(8):1 – 13, 2014.

[78] D. T. Nguyen, A. Thiagalingam, A. Bhaskaran, M. A. Barry, J. Pouliopoulos, C. Jin, and A. L. McEwan. Electrical impedance tomography for assessing ventilation/perfusion mismatch for pulmonary embolism detection without interruptions in respiration. In *2014 36th Annual International Conference of the IEEE Engineering in Medicine and Biology Society*, pages 6068–6071, Aug 2014.

[79] K. Roubik, V. Sobota, and M. Laviola. Selection of the Baseline Frame for Evaluation of Electrical Impedance Tomography of the Lungs. In *2015 Second International Conference on Mathematics and Computers in Sciences and in Industry (MCSI)*, pages 293–297, Aug 2015.

[80] A. D. Waldmann, C. F. Ortolá, M. M. Martinez, A. Vidal, A. Santos, M. P. Márquez, P. L. Róka, S. H. Bohm, and F. Suarez-Sipmann. Position-dependent distribution of lung ventilation: A feasability study. In *2015 IEEE Sensors Applications Symposium (SAS)*, pages 1–6, April 2015.

[81] Constantin JC Trepte, Charles R Phillips, Josep Solà, Andy Adler, Sebastian A Haas, Michael Rapin, Stephan H Böhm, and Daniel A Reuter. Electrical impedance tomography (EIT) for quantification of pulmonary edema in acute lung injury. *Critical Care*, 20(1):18, 2016.

[82] L Andiani, A Rubiyanto, et al. Sensitivity analysis of thorax imaging using two-dimensional electrical impedance tomography (EIT). In *Journal of Physics: Conference Series*, volume 1248, page 012009. IOP Publishing, 2019.

[83] João Batista Borges, Fernando Suarez-Sipmann, Stephan H Bohm, Gerardo Tusman, Alexandre Melo, Enn Maripuu, Mattias Sandström, Marcelo Park, Eduardo LV Costa, Göran Hedenstierna, et al. Regional lung perfusion estimated by electrical impedance tomography in a piglet model of lung collapse. *Journal of applied physiology*, 112(1):225–236, 2012.

[84] Lin Yang, Chao Zhang, Wenbo Liu, Hang Wang, Junying Xia, Benyuan Liu, Xuetao Shi, Xiuzhen Dong, Feng Fu, and Meng Dai. Real-time detection of hemothorax and monitoring its progression in a piglet model by electrical impedance tomography: A feasibility study. *BioMed Research International*, 2020, 2020.

[85] Songqiao Liu, Li Tan, Knut Möller, Inez Frerichs, Tao Yu, Ling Liu, Yingzi Huang, Fengmei Guo, Jingyuan Xu, Yi Yang, et al. Identification of regional overdistension, recruitment and cyclic alveolar collapse with electrical impedance tomography in an experimental ards model. *Critical Care*, 20(1):119, 2016.

[86] F. Trenk, L. Mendes, P. Carvalho, R. P. Paiva, J. Henriques, N. Maglaveras, I. Chouvarda, V. Tsara, and C. A. Teixeira. Evaluation of lung ventilation distribution in

chronic obstructive pulmonary disease patients using the global inhomogeneity index. In *2016 38th Annual International Conference of the IEEE Engineering in Medicine and Biology Society (EMBC)*, pages 5286–5289, Aug 2016.

[87] Z. Zhao, K. Möller, U. Müller-Lisse, B. Vogt, and I. Frerichs. Customized evaluation software for clinical trials: An example on pulmonary function test with electrical impedance tomography. In *2013 ICME International Conference on Complex Medical Engineering*, pages 128–133, May 2013.

[88] S Heizmann, M Baumgärtner, S Krüger-Ziolek, Z Zhao, and K Möller. 3-D Lung Visualization Using Electrical Impedance Tomography Combined with Body Plethysmography. In *The 15th International Conference on Biomedical Engineering*, pages 172–175, 2013.

[89] Tobias Becher, Barbara Vogt, Matthias Kott, Dirk Schädler, Norbert Weiler, and Inéz Frerichs. Functional regions of interest in electrical impedance tomography: A secondary analysis of two clinical studies. *PLoS ONE*, 11(3):1 – 16, 2016.

[90] Judith L Hough, Andrew D Shearman, Helen Liley, Caroline A Grant, and Andreas Schibler. Lung recruitment and endotracheal suction in ventilated preterm infants measured with electrical impedance tomography. *Journal of Paediatrics & Child Health*, 50(11):884 – 889, 2014.

[91] I. Chatziioannidis, T. Samaras, G. Mitsiakos, P. Karagianni, and N. Nikolaidis. Assessment of lung ventilation in infants with respiratory distress syndrome using electrical impedance tomography. *Hippokratia*, 17(2):115 – 119, 2013.

[92] Felipe de Souza Rossi, Ana Cristina Zanon Yagui, Luciana Branco Haddad, Alice D'Agostini Deutsch, and Celso Moura Rebello. Electrical impedance tomography to evaluate air distribution prior to extubation in very-low-birth-weight infants: a feasibility study. *Clinics*, 68(3):345–350, 2013.

[93] K. Buzkova and J. Suchomel. Use of electrical impedance tomography for quantitative evaluation of disability level of bronchopulmonary dysplasia. In *2013 E-Health and Bioengineering Conference (EHB)*, pages 1–4, Nov 2013.

[94] Minseo Kim, Joonsung Bae, and Hoi-Jun Yoo. Wearable 3d lung ventilation monitoring system with multi frequency electrical impedance tomography. In *2017 IEEE Biomedical Circuits and Systems Conference (BioCAS)*, pages 1–4. IEEE, 2017.

[95] N. Omer, S. Abboud, and M. Arad. Classifying lung congestion in congestive heart failure using electrical impedance - a 3D model. In *2015 Computing in Cardiology Conference (CinC)*, pages 369–372, Sept 2015.

[96] Chuong Ngo, Sarah Spagnesi, Carlos Munoz, Sylvia Lehmann, Thomas Vollmer, Berno Misgeld, and Steffen Leonhardt. Assessing regional lung mechanics by combining electrical impedance tomography and forced oscillation technique. *Biomedical Engineering/Biomedizinische Technik*, 63(6):673–681, 2018.

[97] Ulrich Krause, Kristin Becker, Günter Hahn, Jörg Dittmar, Wolfgang Ruschewski, and Thomas Paul. Monitoring of regional lung ventilation using electrical impedance tomography after cardiac surgery in infants and children. *Pediatric cardiology*, 35(6):990–997, 2014.

[98] Barbara Vogt, Sarah Löhr, Zhanqi Zhao, Christian Falkenberg, Tobias Ankermann, Norbert Weiler, and Inéz Frerichs. Regional lung function testing in children using electrical impedance tomography. *Pediatric pulmonology*, 53(3):293–301, 2018.

[99] Inez Frerichs, Zhanqi Zhao, Tobias Becher, Peter Zabel, Norbert Weiler, and Barbara Vogt. Regional lung function determined by electrical impedance tomography during bronchodilator reversibility testing in patients with asthma. *Physiological measurement*, 37(6):698, 2016.

[100] Savino Spadaro, Tommaso Mauri, Stephan H Böhm, Gaetano Scaramuzzo, Cecilia Turrini, Andreas D Waldmann, Riccardo Ragazzi, Antonio Pesenti, and Carlo Alberto Volta. Variation of poorly ventilated lung units (silent spaces) measured by electrical impedance tomography to dynamically assess recruitment. *Critical Care*, 22(1):26, 2018.

[101] Barbara Vogt, Sven Pulletz, Gunnar Elke, Zhanqi Zhao, Peter Zabel, Norbert Weiler, and Inéz Frerichs. Spatial and temporal heterogeneity of regional lung ventilation determined by electrical impedance tomography during pulmonary function testing. *Journal of Applied Physiology*, 113(7):1154–1161, 2012.

[102] Martijn Miedema, Frans H De Jongh, Inez Frerichs, Mariëtte B Van Veenendaal, and Anton H Van Kaam. Changes in lung volume and ventilation during lung recruitment in high-frequency ventilated preterm infants with respiratory distress syndrome. *The Journal of pediatrics*, 159(2):199–205, 2011.

[103] Satoru Nebuya, Tomotaka Koike, Hiroshi Imai, Yoshiaki Iwashita, Brian H Brown, and Kazui Soma. Feasibility of using 'lung density'values estimated from eit images for clinical diagnosis of lung abnormalities in mechanically ventilated icu patients. *Physiological Measurement*, 36(6):1261, 2015.

[104] G Elke, S Pulletz, D Schädler, G Zick, B Gawelczyk, I Frerichs, and N Weiler. Measurement of regional pulmonary oxygen uptake—a novel approach using electrical impedance tomography. *Physiological measurement*, 32(7):877, 2011.

[105] Yuhong Li, Erik Tesselaar, João Batista Borges, SH Böhm, Folke Sjöberg, and Birgitta JANEROT-SJÖBERG. Hyperoxia affects the regional pulmonary ventilation/perfusion ratio: an electrical impedance tomography study. *Acta Anaesthesiologica Scandinavica*, 58(6):716–725, 2014.

[106] Pauline S van der Burg, Martijn Miedema, Frans H de Jongh, Inez Frerichs, and Anton H van Kaam. Cross-sectional changes in lung volume measured by electrical impedance tomography are representative for the whole lung in ventilated preterm infants. *Critical care medicine*, 42(6):1524–1530, 2014.

[107] B. Amm, T. J. Kao, X. Wang, G. Boverman, D. Shoudy, J. Sabatini, J. Ashe, J. Newell, G. Saulnier, D. Isaacson, and D. Davenport. Real-time 3D electrical impedance imaging for ventilation monitoring of the lung: Pilot study. In *2014 36th Annual International Conference of the IEEE Engineering in Medicine and Biology Society*, pages 6064–6067, Aug 2014.

[108] S. Hong, J. Lee, J. Bae, and H. J. Yoo. A 10.4 mW electrical impedance tomography SoC for portable real-time lung ventilation monitoring system. In *Solid-State Circuits Conference (A-SSCC), 2014 IEEE Asian*, pages 193–196, Nov 2014.

[109] J. Lee, U. Ha, and H. J. Yoo. 30-fps SNR equalized electrical impedance tomography IC with fast-settle filter and adaptive current control for lung monitoring. In *2016 IEEE International Symposium on Circuits and Systems (ISCAS)*, pages 109–112, May 2016.

[110] Shangjie Ren, Kai Sun, Dong Liu, and Feng Dong. A statistical shape constrained reconstruction framework for electrical impedance tomography. *IEEE transactions on medical imaging*, 2019.

[111] Chuan Li Yang and M Soleimani. Frequency difference electrical impedance tomography for imaging lung tumour. In *International Conference on Translational Research in Radiation Oncology*, 2014.

[112] J. Solà, M. Proença, D. Ferrario, J. A. Porchet, A. Falhi, O. Grossenbacher, Y. Allemann, S. F. Rimoldi, and C. Sartori. Noninvasive and nonocclusive blood pressure estimation via a chest sensor. *IEEE Transactions on Biomedical Engineering*, 60(12):3505 – 3513, Dec 2013.

[113] J. Solà, A. Adler, A. Santos, G. Tusman, F. Suárez Sipmann, and S.H. Bohm. Unsupervised non-invasive measurement of aortic pulse transit time by means of electrical impedance tomography. *Artery Research*, 5(4):144 –, 2011.

[114] S. Leonhardt, R. Pikkemaat, O. Stenqvist, and S. Lundin. Electrical impedance tomography for hemodynamic monitoring. In *2012 Annual International Conference of the IEEE Engineering in Medicine and Biology Society*, pages 122–125, Aug 2012.

[115] Deborshi Chakraborty, Madhurima Chattopadhyay, and Radhaballabh Bhar. Resistivity imaging of a phantom with irregular inhomogeneities with 32 silver electrodes based sensory system in two dimensional electrical impedance tomography. *Procedia Technology*, 10:191 – 199, 2013. First International Conference on Computational Intelligence: Modeling Techniques and Applications (CIMTA) 2013.

[116] Meng Dai, Bing Li, Shijie Hu, Canhua Xu, Bin Yang, Jianbo Li, Feng Fu, Zhou Fei, and Xiuzhen Dong. In vivo imaging of twist drill drainage for subdural hematoma: A clinical feasibility study on electrical impedance tomography for measuring intracranial bleeding in humans. *PLOS ONE*, 8(1):1–10, 01 2013.

[117] Sukritta Suksawang, Kamonwan Niamsri, and Taweechai Ouypornkochagorn. Scalp voltage response to conductivity changes in the brain in the application of electrical

impedance tomography (EIT). In *2018 15th International Conference on Electrical Engineering/Electronics, Computer, Telecommunications and Information Technology (ECTI-CON)*, pages 223–236. IEEE, 2018.

[118] Lei Wang, Yang Sun, Xinmin Xu, Xiuzhen Dong, and Feng Gao. Real-time imaging of epileptic seizures in rats using electrical impedance tomography. *NeuroReport*, 28(11):689, 2017.

[119] Ge Zhang, Meng Dai, Lin Yang, Weichen Li, Haoting Li, Canhua Xu, Xuetao Shi, Xiuzhen Dong, and Feng Fu. Fast detection and data compensation for electrodes disconnection in long-term monitoring of dynamic brain electrical impedance tomography. *Biomedical engineering online*, 16(1):7, 2017.

[120] Te Tang, Michael D Weiss, Peggy Borum, Sergei Turovets, Don Tucker, and Rosalind Sadleir. In vivo quantification of intraventricular hemorrhage in a neonatal piglet model using an eeg-layout based electrical impedance tomography array. *Physiological measurement*, 37(6):751, 2016.

[121] T Dowrick, C Blochet, and D Holder. In vivo bioimpedance measurement of healthy and ischaemic rat brain: implications for stroke imaging using electrical impedance tomography. *Physiological measurement*, 36(6):1273, 2015.

[122] Feng Fu, Bing Li, Meng Dai, Shi-Jie Hu, Xia Li, Can-Hua Xu, Bing Wang, Bin Yang, Meng-Xing Tang, Xiu-Zhen Dong, et al. Use of electrical impedance tomography to monitor regional cerebral edema during clinical dehydration treatment. *PloS one*, 9(12):e113202, 2014.

[123] Mayo Faulkner, Sana Hannan, Kirill Aristovich, James Avery, and David Holder. Feasibility of imaging evoked activity throughout the rat brain using electrical impedance tomography. *NeuroImage*, 178:1–10, 2018.

[124] Bin Yang, Xuetao Shi, Meng Dai, Canhua Xu, Fushen You, Feng Fu, Ruigang Liu, and Xiuzhen Dong. Real-time imaging of cerebral infarction in rabbits using electrical impedance tomography. *Journal of International Medical Research*, 42(1):173–183, 2014.

[125] Andy Adler, Mayo Faulkner, Kirill Aristovich, Sana Hannan, James Avery, and David S Holder. Cerebral perfusion imaging using EIT. *ELECTRICAL IMPEDANCE TOMOGRAPHY!*, 21:44, 2017.

[126] Haoting Li, Rongqing Chen, Canhua Xu, Benyuan Liu, Mengxing Tang, Lin Yang, Xiuzhen Dong, and Feng Fu. Unveiling the development of intracranial injury using dynamic brain EIT: an evaluation of current reconstruction algorithms. *Physiological measurement*, 38(9):1776, 2017.

[127] Hang Ma, Haoting Li, Xuechao Liu, Weichen Li, Junying Xia, Benyuan Liu, Xuetao Shi, Xiuzhen Dong, and Feng Fu. Real-time monitoring of contact impedance from multiple electrode–scalp interfaces during cerebral electrical impedance tomography. *IEEE Access*, 7:95186–95196, 2019.

[128] Chaoshuang Chen, Feng Fu, Bing Li, Wenbo Liu, Shiwei Xu, Feng Tao, Xuetao Shi, Lin Yang, Zhou Fei, and Xiuzhen Dong. Experimental study of detection of brain tissue with electrical impedance tomography after cerebral ischemic. In *World Congress on Medical Physics and Biomedical Engineering May 26-31, 2012, Beijing, China*, pages 807–810. Springer, 2013.

[129] Meng Dai, Xue-Chao Liu, Hao-Ting Li, Can-Hua Xu, Bin Yang, Hang Wang, Xue-Tao Shi, Xiu-Zhen Dong, and Feng Fu. EIT imaging of intracranial hemorrhage in rabbit models is influenced by the intactness of cranium. *BioMed research international*, 2018, 2018.

[130] Yandong Li, Ding Zhang, Benyuan Liu, Zhenxiao Jin, Weixun Duan, Xiuzhen Dong, Feng Fu, Shiqiang Yu, and Xuetao Shi. Noninvasive cerebral imaging and monitoring using electrical impedance tomography during total aortic arch replacement. *Journal of Cardiothoracic and Vascular Anesthesia*, 32(6):2469–2476, 2018.

[131] Eoghan Dunne, Martin O'Halloran, Darren Craven, Prem Puri, Paul Frehill, Sarah Loughney, and Emily Porter. Detection of vesicoureteral reflux using electrical impedance tomography. *IEEE Transactions on Biomedical Engineering*, 66(8):2279–2286, 2018.

[132] Thomas Schlebusch, Steffen Nienke, S Leonhardt, and M Walter. Bladder volume estimation from electrical impedance tomography. *Physiological measurement*, 35(9):1813, 2014.

[133] Thomas Schlebusch, Jakob Orschulik, Jaakko Malmivuo, Steffen Leonhardt, Dorothea Leonhäuser, Joachim Grosse, Michael Kowollik, Ruth Kirschner-Hermanns, and Marian Walter. Impedance ratio method for urine conductivity-invariant estimation of bladder volume. *Journal of Electrical Bioimpedance*, 5(1):48–54, 2014.

[134] S. Leonhardt, A. Cordes, H. Plewa, R. Pikkemaat, I. Soljanik, K. Moehring, H.J. Gerner, and R. Rupp. Electric impedance tomography for monitoring volume and size of the urinary bladder. *Biomedizinische Technik*, 56(6):301–307, 2011. cited By 11.

[135] Dorothea Leonhäuser, Carlos Castelar, Thomas Schlebusch, Martin Rohm, Rüdiger Rupp, Steffen Leonhardt, Marian Walter, and Joachim O Grosse. Evaluation of electrical impedance tomography for determination of urinary bladder volume: comparison with standard ultrasound methods in healthy volunteers. *Biomedical engineering online*, 17(1):95, 2018.

[136] Carlos Castellar. Internal electrode bladder volume EIT for routine urodynamic test application: An FEM study using EIDORS framework. In *Proceedings of the 20th International Scientific Student Conferenece POSTER, Prague, Czech*, pages 1–5. Czech Technical University in Prague, 2016.

[137] R. R. Ribeiro, A. R. S. Feitosa, R. E. de Souza, and W. P. dos Santos. Reconstruction of electrical impedance tomography images using genetic algorithms and non-blind search. In *2014 IEEE 11th International Symposium on Biomedical Imaging (ISBI)*, pages 153–156, April 2014.

[138] L. Lu, L. Liu, and C. Hu. Analysis of the electrical impedance tomography algorithm based on finite element method and tikhonov regularization. In *2014 International Conference on Wavelet Analysis and Pattern Recognition*, pages 36–42, July 2014.

[139] Nick Polydorides and William RB Lionheart. A matlab toolkit for three-dimensional electrical impedance tomography: a contribution to the electrical impedance and diffuse optical reconstruction software project. *Measurement science and technology*, 13(12):1871, 2002.

[140] Tushar Kanti Bera and J Nagaraju. A FEM-based forward solver for studying the forward problem of electrical impedance tomography (EIT) with a practical biological phantom. In *2009 IEEE International Advance Computing Conference*, pages 1375–1381. IEEE, 2009.

[141] M. Hadinia and R. Jafari. An element-free galerkin forward solver for the complete-electrode model in electrical impedance tomography. *Flow Measurement and Instrumentation*, 45:68 – 74, 2015.

[142] X. Zhang, G. Xu, S. Zhang, Y. Li, Y. Guo, Y. Li, Y. Wang, and W. Yan. A numerical computation forward problem model of electrical impedance tomography based on generalized finite element method. *IEEE Transactions on Magnetics*, 50(2):1045–1048, Feb 2014.

[143] P. Ghaderi Daneshmand and R. Jafari. A 3D hybridBE-FE solution to the forward problem of electrical impedance tomography. *Engineering Analysis with Boundary Elements*, 37(4):757 – 764, 2013.

[144] P. Kantartzis and P. Liatsis. On sparse forward solutions in non-stationary domains for the eit imaging problem. In *2011 Annual International Conference of the IEEE Engineering in Medicine and Biology Society*, pages 3892–3896, Aug 2011.

[145] M. Jehl, A. Dedner, T. Betcke, K. Aristovich, R. Klöfkorn, and D. Holder. A fast parallel solver for the forward problem in electrical impedance tomography. *IEEE Transactions on Biomedical Engineering*, 62(1):126–137, Jan 2015.

[146] Päivi J Vauhkonen, Marko Vauhkonen, Tuomo Savolainen, and Jari P Kaipio. Three-dimensional electrical impedance tomography based on the complete electrode model. *IEEE Transactions on Biomedical Engineering*, 46(9):1150–1160, 1999.

[147] M. R. Yousefi, R. Jafari, and H. A. Moghaddam. A combined wavelet - based mesh - free method for solving the forward problem in electrical impedance tomography. *IEEE Transactions on Instrumentation and Measurement*, 62(10):2629–2638, Oct 2013.

[148] X. Zhang, G. Xu, S. Zhang, H. Wang, Y. Xu, Y. Li, and W. Yan. Forward problem model of human thorax during breath in electrical impedance tomography. In *Electromagnetic Field Problems and Applications (ICEF), 2012 Sixth International Conference on*, pages 1–4, June 2012.

[149] Marko Vauhkonen, William RB Lionheart, Lasse M Heikkinen, Päivi J Vauhkonen, and Jari P Kaipio. A MATLAB package for the EIDORS project to reconstruct two-dimensional EIT images. *Physiological measurement*, 22(1):107, 2001.

[150] Andy Adler, John H Arnold, Richard Bayford, Andrea Borsic, Brian Brown, Paul Dixon, Theo JC Faes, Inéz Frerichs, Hervé Gagnon, Yvo Gärber, et al. GREIT: a unified approach to 2D linear EIT reconstruction of lung images. *Physiological measurement*, 30(6):S35, 2009.

[151] Vidya Sarode, Sneha Patkar, and Alice N Cheeran. Comparison of 2-D algorithms in EIT based image reconstruction. *International Journal of Computer Applications*, 69(8), 2013.

[152] David R Stephenson, John L Davidson, William RB Lionheart, Bruce D Grieve, and Trevor A York. Comparison of 3D image reconstruction techniques using real electrical impedance measurement data. In *Proceedings of the 4th World Congress on Industrial Process Tomography*, pages 643–650, 2005.

[153] Tao Dai, Manuchehr Soleimani, and Andy Adler. Eit image reconstruction with four dimensional regularization. *Medical & biological engineering & computing*, 46(9):889–899, 2008.

[154] Andy Adler, Tao Dai, and William RB Lionheart. Temporal image reconstruction in electrical impedance tomography. *Physiological measurement*, 28(7):S1, 2007.

[155] Nicholas Polydorides, William RB Lionheart, and Hugh McCann. Krylov subspace iterative techniques: on the detection of brain activity with electrical impedance tomography. *IEEE Transactions on Medical Imaging*, 21(6):596–603, 2002.

[156] Kyung Youn Kim, Bong Seok Kim, Min Chan Kim, Sin Kim, Yoon Joon Lee, Hae Jin Jeon, Bong Yeol Choi, and Marko Vauhkonen. Electrical impedance imaging of two-phase fields with an adaptive mesh grouping scheme. *IEEE transactions on magnetics*, 40(2):1124–1127, 2004.

[157] R. Ribeiro, A. Feitosa, R. de Souza, and W. dos Santos. A modified differential evolution algorithm for the reconstruction of electrical impedance tomography images. In *5th ISSNIP-IEEE Biosignals and Biorobotics Conference (2014): Biosignals and Robotics for Better and Safer Living (BRC)*, pages 1–6, May 2014.

[158] Liyun Rao, Renjie He, Youhua Wang, Weili Yan, Jing Bai, and Datian Ye. An efficient improvement of modified newton-raphson algorithm for electrical impedance tomography. *IEEE transactions on magnetics*, 35(3):1562–1565, 1999.

[159] Marc Molinari, Simon J Cox, Barry H Blott, and Geoffrey J Daniell. Comparison of algorithms for non-linear inverse 3D electrical tomography reconstruction. *Physiological Measurement*, 23(1):95–104, jan 2002.

[160] D Romano, S Pisa, and E Piuzzi. Implementation of the newton-raphson and admittance methods for EIT. *International Journal of Bioelectromagnetism*, 12(1):12–20, 2010.

[161] Nababithi Goswami, Supriyo K Mondal, and Swapan Paruya. A comparative study of dual active-set and primal-dual interior-point method. *IFAC Proceedings Volumes*, 45(15):620–625, 2012.

[162] Zhou Zhou, Gustavo Sato dos Santos, Thomas Dowrick, James Avery, Zhaolin Sun, Hui Xu, and David S Holder. Comparison of total variation algorithms for electrical impedance tomography. *Physiological measurement*, 36(6):1193, 2015.

[163] Marko Vauhkonen, Pasi A Karjalainen, and Jari P Kaipio. A kalman filter approach to track fast impedance changes in electrical impedance tomography. *IEEE Transactions on Biomedical Engineering*, 45(4):486–493, 1998.

[164] KY Kim, BS Kim, MC Kim, YJ Lee, and M Vauhkonen. Image reconstruction in time-varying electrical impedance tomography based on the extended kalman filter. *Measurement Science and Technology*, 12(8):1032, 2001.

[165] Radek Hrabuska, Michal Prauzek, Marketa Venclikova, and Jaromir Konecny. Image reconstruction for electrical impedance tomography: Experimental comparison of radial basis neural network and gauss – newton method. *IFAC-PapersOnLine*, 51(6):438 – 443, 2018. 15th IFAC Conference on Programmable Devices and Embedded Systems PDeS 2018.

[166] Sarah Jane Hamilton and Andreas Hauptmann. Deep d-bar: Real-time electrical impedance tomography imaging with deep neural networks. *IEEE transactions on medical imaging*, 37(10):2367–2377, 2018.

[167] Naimul Islam, K Siddique-e Rabbani, and Adrian Wilson. The sensitivity of focused electrical impedance measurements. *Physiological measurement*, 31(8):S97, 2010.

[168] Nusrat Jahan Surovy, Md Masum Billah, Salahuddin Haowlader, Golam Dastegir Al-Quaderi, and K Siddique-e Rabbani. Determination of abdominal fat thickness using dual electrode separation in the focused impedance method (FIM). *Physiological measurement*, 33(5):707, 2012.

[169] Jan C de Munck, Theo JC Faes, and Rob M Heethaar. The boundary element method in the forward and inverse problem of electrical impedance tomography. *IEEE transactions on Biomedical Engineering*, 47(6):792–800, 2000.

[170] Masum Iquebal and K Siddique-e Rabbani. Correlation of liquid volume in stomach to electrical transfer impedance measurements using FIM. *Bangladesh Journal of Medical Physics*, 6(1), 2014.

[171] K Siddique-e Rabbani and M Abdul Kadir. Possible applications of focused impedance method (FIM) in biomedical and other areas of study. *Bangladesh Journal of Medical Physics*, 4(1), 2013.

[172] David S. Holder. *Electrical Impedance Tomography: Methods, History and Applications*. Institute of Physics Publishing, 2004.

[173] Olavo H Menin, Vanessa Rolnik, and Alexandre S Martinez. Boundary element method and simulated annealing algorithm applied to electrical impedance tomography image reconstruction. *Revista Brasileira de Ensino de Física*, 35(2):1–7, 2013.

[174] Franco Simini and Pedro Bertemes-Filho. *Bioimpedance in biomedical applications and research*. Springer, 2018.

[175] T. Strouboulis, K. Copps, and I. Babuska. The generalized finite element method. *Computer Methods in Applied Mechanics and Engineering*, 190(32):4081 – 4193, 2001.

[176] Saeed Zaravi, Rassoul Amirfattahi, Bijan Vosoughi Vahdat, and Ali Hassanipour. Improving 2D block method in electrical impedance tomography. In *2015 22nd Iranian Conference on Biomedical Engineering (ICBME)*, pages 245–250. IEEE, 2015.

[177] Ian Jeffrey, Nicholas Geddert, Kevin Brown, and Joe LoVetri. The time-harmonic discontinuous galerkin method as a robust forward solver for microwave imaging applications. *Progress In Electromagnetics Research*, 154:1–21, 2015.

[178] MG Crabb. Convergence study of 2D forward problem of electrical impedance tomography with high-order finite elements. *Inverse Problems in Science and Engineering*, 25(10):1397–1422, 2017.

[179] Y Ma, SA Miedema, V Matousek, and WJ Vlasblom. Tomography as a measurement method for density and velocity distributions. In *23rd WEDA Technical Conference & 35th TAMU Dredging Seminar, Chicago, USA*, 2003.

[180] Saeed Zaravi, Rasoul Amirfattahi, and Bijan Vosoughi Vahdat. Expanding 2D block method in two direction by a new formula in EIT. In *2015 23rd Iranian Conference on Electrical Engineering*, pages 131–135. IEEE, 2015.

[181] William RB Lionheart. EIT reconstruction algorithms: pitfalls, challenges and recent developments. *Physiological measurement*, 25(1):125, 2004.

[182] Tushar Kanti Bera, Samir Kumar Biswas, K Rajan, and J Nagaraju. Projection error propagation-based regularization (PEPR) method for resistivity reconstruction in electrical impedance tomography (EIT). *Measurement*, 49:329–350, 2014.

[183] Tushar Kanti Bera, Samir Kumar Biswas, K Rajan, and J Nagaraju. Improving conductivity image quality using block matrix-based multiple regularization (BMMR) technique in EIT: a simulation study. *Journal of Electrical Bioimpedance*, 2(1):33–47, 2019.

[184] Bangti Jin and Peter Maass. An analysis of electrical impedance tomography with applications to tikhonov regularization. *ESAIM: Control, Optimisation and Calculus of Variations*, 18(4):1027–1048, 2012.

[185] Alistair Boyle and Andy Adler. The impact of electrode area, contact impedance and boundary shape on eit images. *Physiological measurement*, 32(7):745, 2011.

[186] BM Graham and Andy Adler. Objective selection of hyperparameter for EIT. *Physiological measurement*, 27(5):S65, 2006.

[187] David Silvera Tawil, David Rye, and Mari Velonaki. Improved image reconstruction for an EIT-based sensitive skin with multiple internal electrodes. *IEEE Transactions on Robotics*, 27(3):425–435, 2011.

[188] Manuchehr Soleimani, Phaneendra K Yalavarthy, and Hamid Dehghani. Helmholtz-type regularization method for permittivity reconstruction using experimental phantom data of electrical capacitance tomography. *IEEE Transactions on Instrumentation and Measurement*, 59(1):78–83, 2009.

[189] Jan Dinkelbach and Birgit Stender. Evaluation of cardiac induced impedance changes in EIT images using 4D image-based FEM simulations. In *Proc. of the 16th Int. Conf. on Biomedical Applications of Electrical Impedance Tomography (Zenodo Neuchtel, Switzerland,)*, page 109, 2015.

[190] Andrea Borsic, Brad M Graham, Andy Adler, and William RB Lionheart. In vivo impedance imaging with total variation regularization. *IEEE transactions on medical imaging*, 29(1):44–54, 2009.

[191] Y. M. Jung and S. Yun. Impedance imaging with first-order TV regularization. *IEEE Transactions on Medical Imaging*, 34(1):193–202, Jan 2015.

[192] Wei He, Peng Ran, Zheng Xu, Bing Li, and Song-nong Li. A 3D visualization method for bladder filling examination based on EIT. *Computational and mathematical methods in medicine*, 2012, 2012.

[193] Ashkan Javaherian, Amir Movafeghi, and Reza Faghihi. Reducing negative effects of quadratic norm regularization on image reconstruction in electrical impedance tomography. *Applied Mathematical Modelling*, 37(8):5637 – 5652, 2013.

[194] Tushar Kanti Bera, Samir Kumar Biswas, K Rajan, and Jampana Nagaraju. Image reconstruction in electrical impedance tomography (EIT) with projection error propagation-based regularization (PEPR): a practical phantom study. In *International Conference on Advanced Computing, Networking and Security*, pages 95–105. Springer, 2011.

[195] PA Hasgall, F Di Gennaro, C Baumgartner, E Neufeld, MC Gosselin, D Payne, A Klingenböck, and N Kuster. It'is database for thermal and electromagnetic parameters of biological tissues. *Version 3.0*, 2015.

[196] P Kauppinen, J Hyttinen, and J Malmivuo. Sensitivity distribution simulations of impedance tomography electrode combinations. In *BEM & NFSI Conference Proceedings*, volume 7, pages 344–347, 2005.

[197] David B Geselowitz. An application of electrocardiographic lead theory to impedance plethysmography. *IEEE Transactions on biomedical Engineering*, (1):38–41, 1971.

[198] WR Fan and HX Wang. Maximum entropy regularization method for electrical impedance tomography combined with a normalized sensitivity map. *Flow Measurement and Instrumentation*, 21(3):277–283, 2010.

[199] Eduardo LV Costa, R Gonzalez Lima, and Marcelo BP Amato. Electrical impedance tomography. In *Yearbook of Intensive Care and Emergency Medicine*, pages 394–404. Springer, 2009.

[200] Hervé Gagnon, Martin Cousineau, Andy Adler, and Alzbeta E Hartinger. A resistive mesh phantom for assessing the performance of EIT systems. *IEEE transactions on biomedical engineering*, 57(9):2257–2266, 2010.

[201] M Abdul Kadir, Syed Parvez Ahmed, Golam Dastegir Al Quaderi, Rubina Rahman, and K Siddique-e Rabbani. Application of focused impedance method (FIM) to determine the volume of an object within a volume conductor. In *Proceedings of the 2013 COMSOL Conference, Bangalore, India http://www. comsol. com/paper/download/182751/kadir_ paper. pdf*, 2013.

[202] Ahmed Raihan Abir and K Siddique-e Rabbani. Sensitivity study for a 4-electrode focused impedance method (FIM) using finite element method analysis. *Bangladesh Journal of Medical Physics*, 7, 2015.

[203] Sayed Parvez Ahmed, M Abdul Kadir, Golam Dastegir Al-Quaderi, Rubina Rahman, and K Siddique-e Rabbani. Improved understanding of the sensitivity of linear tetrapolar impedance measurement (TPIM) and 8-electrode focused impedance method (FIM) in a volume conductor. *Bangladesh Journal of Medical Physics*, 8, 2017.

[204] Golam Dastegir Al-Quaderi, Sayed Parvez Ahmed, and K Siddique-e Rabbani. Determination of the thickness of a resistive material layer in a finite volume conductor using focused impedance method (FIM) a simulation study. *Bangladesh Journal of Medical Physics*, 7(1):8–23, 2014.

[205] FJ Pettersen, H Ferdous, H Kalvøy, Ø G Martinsen, and JO Høgetveit. Comparison of four different FIM configurations—a simulation study. *Physiological measurement*, 35(6):1067, 2014.

[206] Abdullah Al Amin, Shahnaj Parvin, MA Kadir, Tasmia Tahmid, S Kaisar Alam, and K Siddique-e Rabbani. Classification of breast tumour using electrical impedance and machine learning techniques. *Physiological measurement*, 35(6):965, 2014.

[207] M Abdul Kadir, Tanvir Noor Baig, and K Siddique-e Rabbani. Focused impedance method to detect localized lung ventilation disorders in combination with conventional spirometry. *Biomedical Engineering: Applications, Basis and Communications*, 27(03):1550029, 2015.

[208] Samiron Kumar Saha, Golam Dastegir Al-Quaderi, and K Siddique-e Rabbani. 3D sensitivity of 8-electrode FIM through experimental study in a phantom. *Bangladesh Journal of Medical Physics*, 6(1), 2014.

[209] Khondkar Siddique-e Rabbani. Focused impedance method: Basics and applications. In *Bioimpedance in Biomedical Applications and Research*, pages 137–185. Springer, 2018.

[210] KS Rabbani, M Sarker, MHR Akond, and T Akter. Focused impedance measurement (FIM): a new technique with improved zone localization. *Annals of the New York Academy of Sciences*, 873(1):408–420, 1999.

[211] KS Rabbani and MAS Karal. A new four-electrode focused impedance measurement (FIM) system for physiological study. *Annals of biomedical engineering*, 36(6):1072–1077, 2008.

[212] Van Yang, P Aroul, and K Wen. Impedance measurement with the AFE4300. *Application Repor. SBAA202–October*, 2013.

[213] Alessandro Palla, Claudio Crema, Luca Fanucci, and Paolo Bellagente. Kalman-based approach to bladder volume estimation for people with neurogenic dysfunction of the urinary bladder. In *International Conference on Computers Helping People with Special Needs*, pages 521–528. Springer, 2016.

[214] P. Ran, X. Xiao, W. He, Z. Li, W. Wang, and Y. Pang. Planar array electrical impedance tomography system evaluation for breast and abdomen detection. *Journal of Medical Imaging and Health Informatics*, 5(7):1450–1454, 2015. cited By 1.

[215] T Schlebusch, S Nienke, D Leonhäuser, J Grosse, and S Leonhardt. Optimal electrode positions to determine bladder volume by bioimpedance spectroscopy. *Lecture Notes on Impedance Spectroscopy*, 4:67–73, 2013.

[216] Tushar Kanti Bera and J. Nagaraju. Studying the resistivity imaging of chicken tissue phantoms with different current patterns in Electrical Impedance Tomography (EIT). *Measurement*, 45(4):663 – 682, 2012.

[217] T. F. Yamaguchi, M. Katashima, L. q. Wang, and S. Kuriki. Imaging and estimation of human abdominal fat by electrical impedance tomography using multiple voltage measurement patterns. In *2013 35th Annual International Conference of the IEEE Engineering in Medicine and Biology Society (EMBC)*, pages 3299–3302, July 2013.

[218] Tadashi Ito, Naosumi Kaneda, and Yuuichi Higuchi. Simulation based prior evaluation of 3D EIT system with a small number of electrodes. In *2017 56th Annual*

Conference of the Society of Instrument and Control Engineers of Japan (SICE), pages 912–915. IEEE, 2017.

[219] Mengxing Tang, Wei Wang, James Wheeler, Malcolm McCormick, and Xiuzhen Dong. The number of electrodes and basis functions in EIT image reconstruction. *Physiological measurement*, 23(1):129, 2002.

[220] Eoghan Dunne, Brian McGinley, Martin O'Halloran, and Emily Porter. A realistic pelvic phantom for electrical impedance measurement. *Physiological measurement*, 39(3):034001, 2018.

[221] Eoghan Dunne, Adam Santorelli, Brian McGinley, Geraldine Leader, Martin O'Halloran, and Emily Porter. Image-based classification of bladder state using electrical impedance tomography. *Physiological Measurement*, 39(12):124001, 2018.

[222] Víctor Hugo Mosquera, Adrian Arregui, Ramon Bragós Bardia, and Carlos Felipe Rengifo. Implementation of a low cost prototype for electrical impedance tomography based on the integrated circuit for body composition measurement AFE4300. In *Proceedings of the 11th International Joint Conference on Biomedical Engineering Systems and Technologies (BIOSTEC 2018): January 19-21, 2018: Funchal, Madeira, Portugal*, pages 121–127. Scitepress, 2018.

[223] Vernoon Ang, MHF Rahiman, and RA Rahim. Study of gauss–newton and total variation image reconstruction approach in imaging the phantom in concrete using electrical resistance tomography. In *Symposium on Intelligent Manufacturing and Mechatronics*, pages 487–496. Springer, 2019.

[224] K. S. Rabbani and M. A. S. Karal. A new four-electrode focused impedance measurement (FIM) system for physiological study. *Annals of Biomedical Engineering*, 36(6):1072–1077, Jun 2008.

[225] Sayed Parvez Ahmed, M Abdul Kadir, Rubina Rahman, Golam Dastegir Al Quaderi, and K Siddique-e Rabbani. Determination of organ volume using focused impedance method (FIM): A simulation approach. *Bangladesh Journal of Medical Physics*, 7, 2015.